Luminescence of Graphene in the Visible Spectral Range after Short-Pulse Excitation in the Near Infrared

Lumineszenz von Graphen im sichtbaren Spektralbereich
nach Kurzpulsanregung im nahen Infrarot

MASTERARBEIT

zur Erlangung des akademischen Grades
Master of Science
(M. Sc.)
im Fach Physik

eingereicht an der
Mathematisch-Naturwissenschaftlichen Fakultät
Institut für Physik
Humboldt-Universität zu Berlin

von
Herrn Martin Rothe
geboren am 15.10.1990 in Berlin

Gutachter:

1. Prof. Dr. Oliver Benson
2. Prof. Dr. Jürgen P. Rabe

eingereicht am 22.09.2015

Abstract

Graphene is well known for its unique electronic and optical properties. The study and manipulation of its nonlinear optical response at energies in the range of visible light is of interest for the understanding of its charge carrier dynamics in this energy regime [1]. In this thesis the investigations of a broad luminescence of graphene and graphene multilayers in the entire visible spectral range after excitation with femtosecond laser pulses in the near infrared are presented. The spectrum that starts even above twice the excitation energy indicates multi-photon absorption or efficient electron scattering processes. This method of luminescence excitation is not only well suited for imaging with high contrast but can also gain insight into fundamental electron relaxation and collective excitation processes [2].

Kurzfassung

Graphen ist bekannt für seine einzeigartigen elektronischen und optischen Eigenschaften. Die Untersuchung und Manipulation seiner nicht-linearen optischen Eigenschaften im sichtbaren Spektralbereich trägt zum Verständnis der Ladungsträgerdynamik in diesem Energiebereich bei [1]. In dieser Arbeit werden Untersuchungen zur Lumineszenz von Graphen und Graphen-Multilagen präsentiert, deren Spektrum den gesamten sichtbaren Spektralbereich abdeckt. Die Lumineszenz wird durch Femtosekunden-Laserpulse im nahen Infrarot angeregt. Das Spektrum, welches sogar die doppelte Anregungsphotonenenergie übersteigt, deutet auf Mehrphotonenabsorption oder effiziente Elektronenstreuprozesse im Graphen hin. Diese Methode der Lumineszenzanregung ist nicht nur zur Abbildung mit hohem Kontrast gut geeignet, sie bietet auch die Möglichkeit, Einblicke in fundamentale Elektronenrelaxations- und kollektive Anregungsprozesse zu erlangen [2].

Table of Contents

Abbreviations

AFM	atomic force microscope
APD	avalanche photodiode
BBO	β-Barium borate
CCD	charge-coupled device
DFT	density functional theory
EELS	electron energy loss spectroscopy
LDOS	local density of states
NA	numerical aperture
NIR	near-infrared
RPA	random phase approximation
SHG	second harmonic generation
SP	surface plasmon
SPP	surface plasmon polariton
TBA	tight binding approximation
TE	transverse electric
Ti:Sa	Titanium-doped sapphire
TM	transverse magnetic
TPL	two-photon luminescence

1 Introduction

Mankind's understanding of the nature has always been accompanied with optical observations. Optical investigations of periodic time lapses of sun and stars let early ancient people predict seasons and weather conditions. In the 17th century at latest, "optics" revolutionized our understanding of the world: the invention of optical tools, e.g. telescopes and microscopes, led to insights into the principles of the cosmos (Galileo, Newton) or the foundations of life (Hooke and others). Together with the evolution of electricity and electronics, optical illumination methods were able to actively excite luminescence of particles and molecules which would remain in the dark otherwise. Today, optical tools made their way out of the lab into technology with multiple applications for industry and the people, ranging from laser to smartphone. Thus, the comprehension of light-matter interaction has been and will be a key skill for the development of devices and research.

In the field of nanooptics the light-matter interaction is studied and controlled on a length scale well below the diffraction limit of visible light. At these length-scales the quantum nature of matter is becoming more and more important. As a matter of fact the understanding and control of the relevant physical processes may enable the exploration of non-classical features for future optical building blocks with yet inaccessible functionality.

A subsection of nanooptics deals with the interaction of light with the free electrons on the surface of a metal. The solution of Maxwell's equations provide specific electromagnetic field distributions localized on the surface. The quanta of these fields are called surface plasmon polaritons, briefly SPPs or sometimes just plasmons. SPPs allow the localization of light into sub-wavelength dimensions and thus a strong field enhancement. This effect is used e.g. in surface enhanced Raman scattering which allows Raman spectroscopy on the single molecule level [3]. The localization of SPPs to the surface allows its observation and application not only at the surface of a bulk but also in thin metallic films.

A material that recently attracted much attention is graphene. Graphene is the two dimensional type of graphite, i.e. a one atom thin layer. Thought to be thermodynamic unstable, a run on graphene has started when the converse was proofed. For the fabrication and first measurements on the unique electronic properties (published in 2004) A.K. Geim and K.S. Novoselov earned the Nobel prize in Physics 2010. Graphene exhibits a record high electron mobility, a high thermal conductivity and a huge intrinsic strength. The high optical quantum efficiency is revealed in the optical absorption of $\pi\alpha \approx 2.3\%$ per atomic layer for normal incident light below 3eV photon energy [4]. Its 2D confinement provide good technical access for e.g. electrostatic doping and tuning. Graphene photodetectors are presently one of the most actively studied photonic devices and graphene based optical modulators might become one of the key active building blocks for future devices [5]. However the implementation in devices requires a complete understanding of the light induced charge carrier dynamics in graphene.

This thesis is motivated by the question if there are plasmonic excitations in

graphene in the visible spectral range. Undoped graphene is known to be plasmonic active in the ultraviolet [6]. Similar to graphite these plasmons are determined by the bandstructure. They are energetically fixed. In the infrared regime, electrostatic doping of graphene opens a gap where plasmonic excitation is allowed whereas electron-hole excitation is forbidden. This allows for relatively weakly damped plasmonic excitations within the graphene sheet. Recently, standing wave patterns in a tapered graphene flake have been observed [7, 8]. The mathematical description predicts the plasmon energy to be limited by the doping level. Since the doping level is limited due to technical reasons such plasmons appear only up to the energy regime of infrared light. Following this distinct calculations plasmons are not expected in the visible spectral range. In contrast, the result of recent measurements [2, 9, 10] can be interpreted towards and new theories [11] predict plasmonic activity in graphene in the visible spectral range.

In this thesis, a nonlinear optical approach is used to gain insight into graphenes plasmonic activity. Two-photon luminescence and second harmonic generation react sensitively on the local density of photonic modes and field intensity. Both features are characteristic plasmonic effects. In turn plasmons could be probed by these effects. It turns out that such experiments (as will be shown later) reveal a variety of phenomena, which can be the basis for a deeper understanding, e.g. of charge carrier dynamics. Although the question of plasmonic activity in the visible spectral range could not be answered yet, this thesis yields a high contrast upconversion imaging technique, studies on the optical degeneration of graphene as well as excitation dependent and spectroscopic measurements. Especially last one treats the upconversion luminescence, the blackbody like emission and second harmonic generation. The thesis is structured as follows:

First of all detailed theoretical descriptions of processes that are relevant for this thesis will be given. SPPs will be described (chapter 2.1) as well as graphene (chapter 2.2) and important aspects of its charge carrier behavior (chapter 2.2.2-2.2.3) Afterwards, selected incoherent and coherent upconversion processes will be discussed in general (chapter 2.3.1-2.3.2). Two examples will be given how two-photon luminescence and second harmonic generation is effected by plasmons (chapter 2.3.3-2.3.4). The paragraph ends up with a summary of reported graphene based upconversion measurements (chapter 2.3.5).

Subsequently, the experimental and technical realization will be discussed. Throughout this thesis, samples of graphene on mica are used (chapter 3.1). The sample preparation, substrate influences and optical characterization methods will be discussed (chapter 3.1.1-3.1.3). Furthermore, the development of the confocal upconversion scanning setup, the properties of the devices and the essential setup characterization is shown (chapter 3.2).

Afterwards, the obtained results will be presented. The first part focus on the confocal upconversion scanning (chapter 4.1). Upconversion scanning was also used to look for spatial modulations and to investigate the excitation intensity dependence of the luminescence. The next section is an excursion to the destruction of graphene (chapter 4.2). At elevated excitation power optical degeneration occurs. Knowledge had been gained before the next section could be started: the spectroscopic investigations (chapter 4.3). In this section, acquisition methods to obtain luminescence spectra and processing of the data are described. The upconversion luminescence is analyzed and a blackbody model is fitted to the data. Results regarding the intensity dependence and a comparison of different layer thicknesses

will be discussed. The section finishes with the attempt to record second harmonic generation. The results lead to important requirements for future investigations of second harmonic generation.

All results will be summarized and interpreted in the discussion chapters (chapter 5.1-5.4). The thesis ends with the conclusion and outlook.

2 Theoretical Basis

Within this chapter a detailed theoretical description of processes that are relevant for this thesis will be given. The surface plasmon polariton will be introduced followed by relevant physical properties and charge carrier dynamics of graphene. The third part of this theory chapter focuses on photon-upconversion. Three processes will be described resulting in luminescence with photon energies exceeding that of the excitation. Finally it will be shown how these nonlinear effects can be used to probe plasmons and what is known about these effects in graphene.

2.1 Surface Plasmon Polaritons

2.1.1 Surface Plasmon Polaritons at Metal Surfaces

Between 1861 and 1862, James Clerk Maxwell published his famous equations describing electric and magnetic field, how they interact and how they alter each other. These equations are the basis for classical electrodynamics. The existence of electromagnetic radiation is described by propagating oscillations of the electric and magnetic fields. This chapter sums up common assumptions and the derivation of the Helmholtz equation which describes the propagation. Furthermore, the formalism is applied to a metal-dielectric interface to obtain one solution which is called a surface plasmon polariton (SPP) [12].

Combining Maxwell's equations one can derive an expression that only depends on $\vec{E}$ and material parameters:

$$\nabla \times \nabla \times \overrightarrow{E}(\vec{r},t) = -\mu_0\epsilon_0\epsilon\frac{\partial^2\vec{E}(\vec{r},t)}{\partial t^2} \tag{2.1}$$

where the electric displacement field is used in the form $\vec{D} = \epsilon_0\epsilon\vec{E}$. This is the form of a linear homogenous and isotropic dielectric with a constant relative permittivity ϵ. ϵ_0 and μ_0 are the vacuum permittivity and permeability, respectively. In the absence of external stimuli $\nabla(\epsilon\vec{E}) = 0$. Further calculations lead to

$$\nabla^2\vec{E}(\vec{r},t) - c^{-2}\epsilon\frac{\partial^2\vec{E}(\vec{r},t)}{\partial t^2} = 0 \tag{2.2}$$

with the speed of light in vacuum $c = 1/\sqrt{\epsilon_0\mu_0}$. One can assume a harmonic time dependent electric field, i.e. $\vec{E}(\vec{r},t) = \vec{E}(\vec{r}) \cdot \mathrm{e}^{-i\omega t}$ with the angular frequency ω. Accordingly, $\vec{k}$ is the wave vector and $k_0 = \omega/c$ is its magnitude for a propagating wave in vacuum. Finally, this yields the Helmholtz equation:

$$\nabla^2\vec{E} + k_0^2\epsilon\vec{E} = 0 \tag{2.3}$$

Straightforward this equation can be applied to the following situation. Without loss of generality on can take an interface in three dimensional space at $z = 0$

which divides the space into a half-space $z < 0$ and $z > 0$, each with its own relative permittivity ϵ_1 and ϵ_2, respectively. The solutions of interest are waves that travel along the x-axis with a complex propagation constant $\beta = k_x$ and no dependence on the y-direction. The geometry is depicted in figure 2.1(a). Taking this form of the electric field

$$\vec{E}(\vec{r}) = \vec{E}(z) \cdot \mathrm{e}^{i\beta x} \tag{2.4}$$

and the analog for the magnetic field and plug it into the Helmholtz equation 2.3 yields the two equations

$$\frac{\partial^2}{\partial z^2} \begin{pmatrix} \vec{E}(z) \\ \vec{H}(z) \end{pmatrix} + \left(k_0^2 \epsilon - \beta^2\right) \cdot \begin{pmatrix} \vec{E}(z) \\ \vec{H}(z) \end{pmatrix} = 0. \tag{2.5}$$

Again, Maxwell's equations can be used to derive a set of six coupled differential equations. For harmonic time dependence, propagation along the x-direction and homogeneity in the y-direction, two sets of self-consistent solutions exist, i.e.

$$\begin{array}{lll} \text{TM mode}: & \text{only} & E_x, E_z, H_y \neq 0, \\ \text{TE mode}: & \text{only} & H_x, H_z, E_y \neq 0. \end{array} \tag{2.6}$$

Of special interest are the solutions, which decay exponentially for increasing magnitude of z, i.e. solutions that do not radiate (leak) to the farfield but are bound to the interface. The result would be an electric and magnetic field which would be proportional to $\exp(-k_2 z)$ for $z > 0$ and $\exp(k_1 z)$ for $z < 0$. The $k_i \equiv k_{z,i}$ for $i = 1, 2$ are the components of the wave vector perpendicular to the interface. The reciprocals define the decay length. Indeed, such a solution exists. In terms of the permittivities ϵ_1 and ϵ_2 the result reads as

$$\begin{array}{rcll} H_y^{(2)}(z) &=& A\mathrm{e}^{i\beta x}\mathrm{e}^{-k_2 z} & \\ E_x^{(2)}(z) &=& iA\frac{k_2}{\omega\epsilon_0\epsilon_2}\mathrm{e}^{i\beta x}\mathrm{e}^{-k_2 z} & \\ E_z^{(2)}(z) &=& -A\frac{\beta}{\omega\epsilon_0\epsilon_2}\mathrm{e}^{i\beta x}\mathrm{e}^{-k_2 z} & \text{for } z > 0 \text{ and} \\ & & & \\ H_y^{(1)}(z) &=& A\mathrm{e}^{i\beta x}\mathrm{e}^{-k_1 z} & \\ E_x^{(1)}(z) &=& -iA\frac{k_1}{\omega\epsilon_0\epsilon_1}\mathrm{e}^{i\beta x}\mathrm{e}^{k_1 z} & \\ E_z^{(1)}(z) &=& -A\frac{\beta}{\omega\epsilon_0\epsilon_1}\mathrm{e}^{i\beta x}\mathrm{e}^{k_1 z} & \text{for } z < 0. \end{array} \tag{2.7}$$

Obviously, this is the TM mode. The field distribution is schematically plotted in figure 2.1 (a). One can neglect the TE mode because the conditions of continuity would end up in a vanishing amplitude prefactor. In the case of the TM mode the constant prefactor A is a consequence of the continuity condition for H_y. From the second continuity condition $D_{z,1}(z = 0) = D_{z,2}(z = 0)$ follows the constancy of $\epsilon_i E_z$ and therefore

$$\frac{k_2}{k_1} = -\frac{\epsilon_2}{\epsilon_1} \tag{2.8}$$

This important relation give the condition for decaying evanescent fields. Exponential decay perpendicular to the surface occurs only when the two permittivities have different signs. This is exactly the case for a metal-dielectric interface. While a dielectric can be described by a positive $\epsilon_2 > 0$, the permittivity for metals is typically frequency dependent $\epsilon_1(\omega) < 0$. When Ohmic losses are taken into account, the condition slightly changes to $\Re(\epsilon_1) < 0$ where $\Re$ denotes the real part.

A small imaginary part of the permittivity would lead to a small oscillatory component perpendicular to the surface or a damped oscillation in the propagation direction. Finally this becomes clear when the H_y components are put again in the wave equation 2.5. The two results

$$k_i^2 = \beta^2 - k_0^2 \epsilon_i \tag{2.9}$$

can be combined and give the dispersion relation of the SPP:

$$\beta = k_0 \sqrt{\frac{\epsilon_1 \epsilon_2}{\epsilon_1 + \epsilon_2}} \tag{2.10}$$

In summary, there are the condition (equation 2.8), the electric and magnetic fields components (equation 2.7) and the dispersion (equation 2.10) of a TM mode traveling along and bound to the interface between metal and dielectric. This is known as a SPP.

The dispersion curve is plotted in figure 2.1 (b). The straight lines are the dispersion for photons in the dielectric plotted exemplary for air and silica. The dispersion of a photon in bulk silica is given by $k = n_{silica} \cdot \omega/c$. The photon and SPP curves never cross because the momentum of the SPP is always higher for a fixed energy. Consequently, SPPs cannot be excited from farfield photons because either energy or momentum is not conserved. Among other things, the evanescent field of total internal reflection or an emitter in the nearfield of the metal surface can serve for the condition of large wave vector and excite the plasmon.

The geometry of a single metallic surface is one of the simplest. The next chapter goes one step further and discuss the case for a thin metallic slab between two dielectrics.

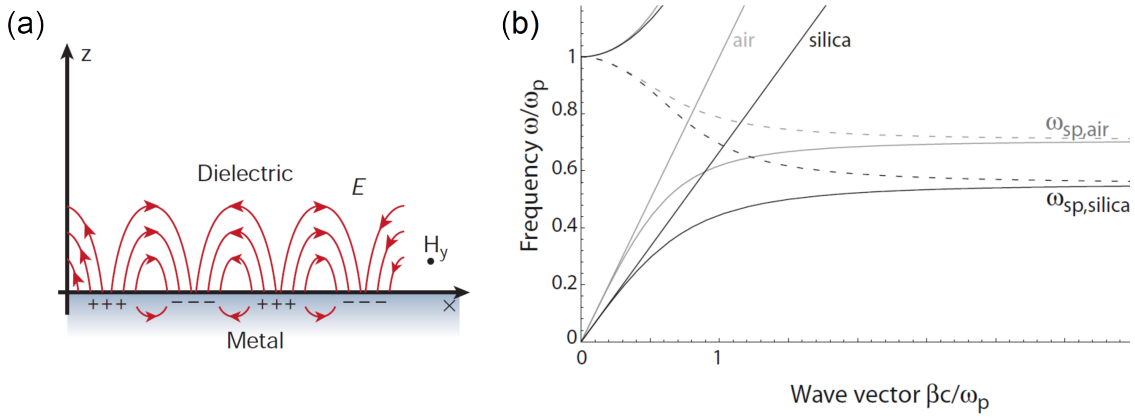

Abbildung 2.1: (a) Schematics of the electric and magnetic field for a surface plasmon polariton [13]. The wave is bound to the metal-dielectric interface in the xy-plane. Both fields decay exponentially with increasing distance from the interface. (b) Dispersion curve of the SPP for the interfaces metal-air (grey) and metal-fused silica (black) [12]. The axis are normalized to the plasma frequency or the corresponding wave vector for a photon in vacuum, respectively. Continuous and broken curves belong to the real and imaginary part of the wave vector β, respectively. The straight lines are the dispersion for photons within die dielectric.

2.1.2 Plasmonic Modes in Thin Metal Slabs

In the previous chapter, the SPP is introduced. This TM mode travels along an interface between metal and dielectric and confines energy to this interface. In the presented context, a more accurate description is given by the geometry of a thin metal slab between two dielectrics. The permittivities will be denoted as ϵ_m for the metal and ϵ_1 and ϵ_2 for the super- and the substrate. In analogy to the previous chapter, the interfaces lie perpendicular to the z-axis, at $z = -a$ and $z = a$, respectively. Hence, the thickness of the slab is $2a$. The propagation direction is parallel to the x-axis. Figure 2.2 depicts the geometry.

For a sufficient thickness, one expects two independent guided modes separated by the metal slab. The situation becomes more complicated when the thickness is of the order of the decay length of the evanescent field within the metal:

$$a \sim k_m^{-1}. \tag{2.11}$$

In consequence, both SPPs interact and give rise to coupled modes and accompanied hybridization. Of course, the solution has to fulfill the wave equation 2.5 and the field components must decay exponentially into the dielectrics. The complete set of non-vanishing field components for the lowest-order bound mode is:

$$\begin{aligned}
H_y^{(1)} &= A\mathrm{e}^{i\beta x}\mathrm{e}^{-k_3 z} \\
E_x^{(1)} &= iA\tfrac{k_1}{\omega\epsilon_0\epsilon_1}\mathrm{e}^{i\beta x}\mathrm{e}^{-k_1 z} \\
E_z^{(1)} &= -A\tfrac{\beta}{\omega\epsilon_0\epsilon_1}\mathrm{e}^{i\beta x}\mathrm{e}^{-k_1 z} && \text{for } z > a\ , \\
\\
H_y^{(m)} &= B\mathrm{e}^{i\beta x}\mathrm{e}^{k_m z} + C\mathrm{e}^{i\beta x}\mathrm{e}^{-k_m z} \\
E_x^{(m)} &= -iB\tfrac{k_m}{\omega\epsilon_0\epsilon_m}\mathrm{e}^{i\beta x}\mathrm{e}^{k_m z} + iC\tfrac{k_m}{\omega\epsilon_0\epsilon_m}\mathrm{e}^{i\beta x}\mathrm{e}^{-k_m z} \\
E_z^{(m)} &= B\tfrac{\beta}{\omega\epsilon_0\epsilon_m}\mathrm{e}^{i\beta x}\mathrm{e}^{k_m z} + C\tfrac{\beta}{\omega\epsilon_0\epsilon_m}\mathrm{e}^{i\beta x}\mathrm{e}^{-k_m z} && \text{for } -a < z < a \text{ and} \\
\\
H_y^{(2)} &= D\mathrm{e}^{i\beta x}\mathrm{e}^{k_2 z} \\
E_x^{(2)} &= -iD\tfrac{k_2}{\omega\epsilon_0\epsilon_2}\mathrm{e}^{i\beta x}\mathrm{e}^{k_2 z} \\
E_z^{(2)} &= -D\tfrac{\beta}{\omega\epsilon_0\epsilon_2}\mathrm{e}^{i\beta x}\mathrm{e}^{k_2 z} && \text{for } z < -a.
\end{aligned} \tag{2.12}$$

The boundary conditions are still valid. Thus, the propagation constant is still linked to the other wave vector components in the form of equation 2.9. The solution of this system of three linear equations yields

$$\mathrm{e}^{-4k_m a} = \frac{\frac{k_m}{\epsilon_m} + \frac{k_1}{\epsilon_1}}{\frac{k_m}{\epsilon_m} - \frac{k_1}{\epsilon_1}} \cdot \frac{\frac{k_m}{\epsilon_m} + \frac{k_2}{\epsilon_2}}{\frac{k_m}{\epsilon_m} - \frac{k_2}{\epsilon_2}}. \tag{2.13}$$

The plasmon dispersion $\beta(\omega)$ is implicitly given by this equation [12].

The relatively complicated general solution is significantly simplified for equal outer dielectrics. Hence, the resulting dispersion obtained from equation 2.13 splits into two branches. The odd and even mode dispersion curves appear to the left and to the right of the single-interface dispersion curve, respectively. In both cases, the qualitative shape follows the single-interface curve.

The case of different dielectrics in the vicinity of a metal slab is treated analytically by B. Prade et al.[14]. A metal with negligible losses is described via its real negative permittivity and its real refractive index. The dielectrics are also described via their refractive index. The absolute values of the refractive indexes and their relation to each other give in sum ten conditions on the existence and form

of the lowest-order modes and subsequently 12 self-sustaining solutions. With two exceptions the solutions have a cut off above and/or below a critical value of $k_m \cdot a$. This means, the solutions need either a small, a high or a specific decay length with respect to the thickness of the slab. However some modes are guided even by a very thin metal slab where $k_m \cdot a$ reach an extreme value.

Even though graphene can be seen as the thinnest possible metal, its description, usually in terms of the non-vanishing sheet conductivity σ, differ from this one. This acquires another approach which will be given in chapter 2.2.3. Before the plasmonic properties of graphene will be discussed, one has to take a closer look to graphenes other properties.

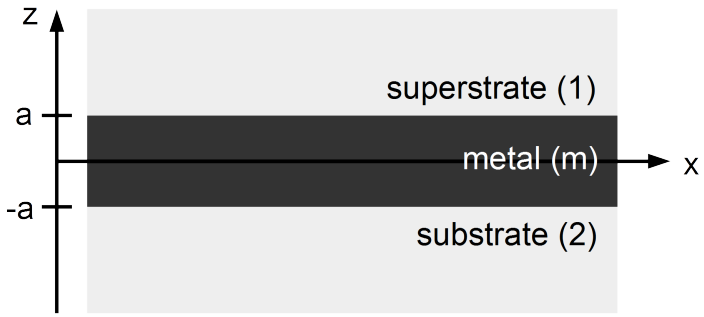

Figure 2.2: Thin metallic layer sandwiched between two dielectrics [12]. When the slab is thin compared to the decay length of the evanescent field the two SPP modes at the interfaces couple. Different sub- and superstrate require a sophisticated description.

2.2 Graphene

2.2.1 Relevant Physical Properties

Carbon is a well known building block in the nature of both inorganic and organic conjunctions. There are two different, purely carbon based materials frequently found in the inanimate nature. Formed in the Earth's mantle under high pressure, diamond is one of them. It consists of carbon atoms arranged in a form of face-centered cubic crystal structure, known as the diamond lattice. The highest energy electrons are located in sp^3-hybridized orbitals around each carbon atom.

The second well known variant of carbon is graphite. In contrast to diamond, only three of four valence electrons are located in sp^2-hybridized orbitals. They form tight bonds with the neighboring atoms in plane. Consequently, each carbon atom contributes one electron which is delocalized in a π or π' orbital. The crystal structure is therefore a quasi two-dimensional honeycomb structure. The term graphite in this sense means several of these two dimensional sheets. They are stacked together by comparatively small van-der-Waals interaction. Several questions motivated the research towards downsizing this structure and reducing its dimensionality. Prominent examples are the C_{60} Buckminsterfullerene, firstly fabricated by Kroto et al. in 1985 [15], and single wall carbon nanotubes, firstly fabricated by Sumio Iijama et al. in 1993 [16].

2004, finally, K.S. Novoselov, A.K. Geim et al. succeeded in fabricating a two dimensional structure consisting of only one layer of graphite [17]. 1986, this so called

graphene was expected to be thermodynamically unstable [18]. It was expected to form fullerenes and nanotubes. However, for the production and the investigation of its unique electronic properties, K.S. Novoselov and A.K. Geim received the Noble Prize in physics 2010. After their success, graphene research has progressed very fast, also because the laboratory procedures enable to obtain high-quality graphene relatively fast and simple [5].

The honeycomb lattice of graphene consist of a two atom basis (figure 2.3 (a)). The distance between the atoms is 1.42 Å. The length of the lattice vectors is 2.46 Å. The π and π' orbital located above and below the sheet give graphene the thickness of 3.4 Å. This value can be used in optical interference experiments to obtain the layer thickness of a few layer thick arrangements.

There are many unique characteristics of graphene exceeding those obtained in any other material. There are the room-temperature electron mobility of $2.5 \cdot 10^5\,\mathrm{cm^2V^{-1}s^{-1}}$ [19], a Youngs's modulus of 1 TPa and intrinsic strength of 130 GPa [20], a very high thermal conductivity of above 3000 W/mK [21] and an optical absorption of exactly $\pi\alpha \approx 2.3\,\%$ per layer in the infrared limit [22].

When the experimental results of this thesis will be discussed (chapter 5) some of the values will become important again. A lot of the mentioned properties are consequences of the unique electronic band structure and charge carrier behavior in graphene. This is described in the k-space where the reciprocal lattice is also a honeycomb (figure 2.3 (b))This will be discussed in more detail in the next chapter.

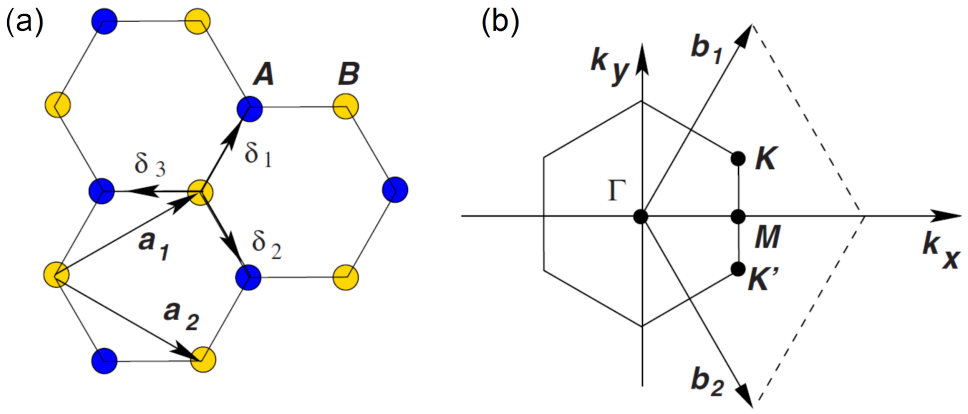

Figure 2.3: (a) The honeycomb lattice of graphene. The atoms of the two sublattices A and B are separated by 1.42 Å. a_1 and a_2 indicate the lattice vectors. (b) The reciprocal lattice is also honeycomb. The high-symmetry points are denoted by Γ, M, K and K' [23].

2.2.2 The Electronic Bandstructure of Graphene

Some of graphene's most impressive properties are results of its unique electronic band structure (figure 2.4 (a)). In real space, the π and π' orbitals are well separated below and above the graphene sheet. The wave functions are orthogonal and therefore one expects a crossing of the energy bands. This is in contrast to graphite (figure 2.4 (c)) where interlayer coupling effects the bandstructure.

Converting the honeycomb lattice from the real space to the reciprocal lattice, one gets a honeycomb lattice again. The Brillouin zone is determined by the $\Gamma-$point in the center of each hexagon, the $M-$point in the middle of each ledge and the

$K-$point on the corner. A tight-binding approximation is usually used to calculate the π and π' energy bands in the reciprocal space. They are of the form

$$E(\vec{k}) = \pm E_0 \sqrt{3 + f(\vec{k})} - E_1 f(\vec{k}) \tag{2.14}$$

with

$$f(\vec{k}) = 2\cos\left(\sqrt{3}k_y a\right) + 4\cos\left(\frac{\sqrt{3}}{2}k_y a\right)\cos\left(\frac{3}{2}k_x a\right) \tag{2.15}$$

where $(k_x, k_y) = (0, 0)$ refers to the $\Gamma-$point. $E_0 = 2.7\text{eV}$ is the nearest neighbor hopping energy and E_1 the next-nearest neighbor hopping energy. In contrast to E_0, E_1 is hard to determine and often set to zero in simpler tight binding models. A more accurate description uses a value of $E_1 = -E_0/5$. π and π' bands are plotted schematically in figure 2.4 (b). Independent of the exact value, the result is a wide separation of valence and conduction band ($\sim 20\,\text{eV}$) at the $\Gamma-$point, saddle points at the $M-$points and a double-cone structure at the $K-$and $K'-$points.

Transforming $\vec{k} \to \vec{\kappa}$, where $(\kappa_x, \kappa_y) = (0, 0)$ refers to the $K-$point, and tailoring the dispersion curve yields

$$E \simeq \pm \hbar v_f \left|\vec{\kappa}\right| \tag{2.16}$$

with the Fermi-velocity of the electrons $v_f = 3E_0 a/2\hbar \approx 10^6\,\text{m/s}$. From special relativity one knows $E = \sqrt{m^2c^4 + p^2c^2}$. Since $\vec{p} = \hbar\vec{\kappa}$ one gets

$$E \propto |\vec{\kappa}| \Leftrightarrow m = 0. \tag{2.17}$$

Conclusively, the dispersion describes effective massless Dirac Fermions moving with their "speed-of-light" v_f. This leads, among other effects, to the record mobility as μ is inversely proportional to the charge carriers mass ($\mu \propto m^{-1}$). Furthermore, the relativistic character makes it necessary to use the Dirac equation for a quantum mechanical description. This in turn leads to counterintuitive effects like Klein tunneling and non reflecting boundaries for spatial-dependent doping [23, 24, 25].

For undoped graphene, the Fermi level lies exactly between the two cones, whereas the density of states goes to zero at this point. Thus, Graphene is often called a "gapless semiconductor" or "quasi-metal". In actual experiments and devices graphene is often supported by a substrate like Si/SiO_2 waver or mica. The influence of the surface and potential contamination by adjacent molecules leads to either p- or n-doped graphene. This can strongly effect optical transitions, charge carrier relaxation and cooling mechanisms of hot electron distributions.

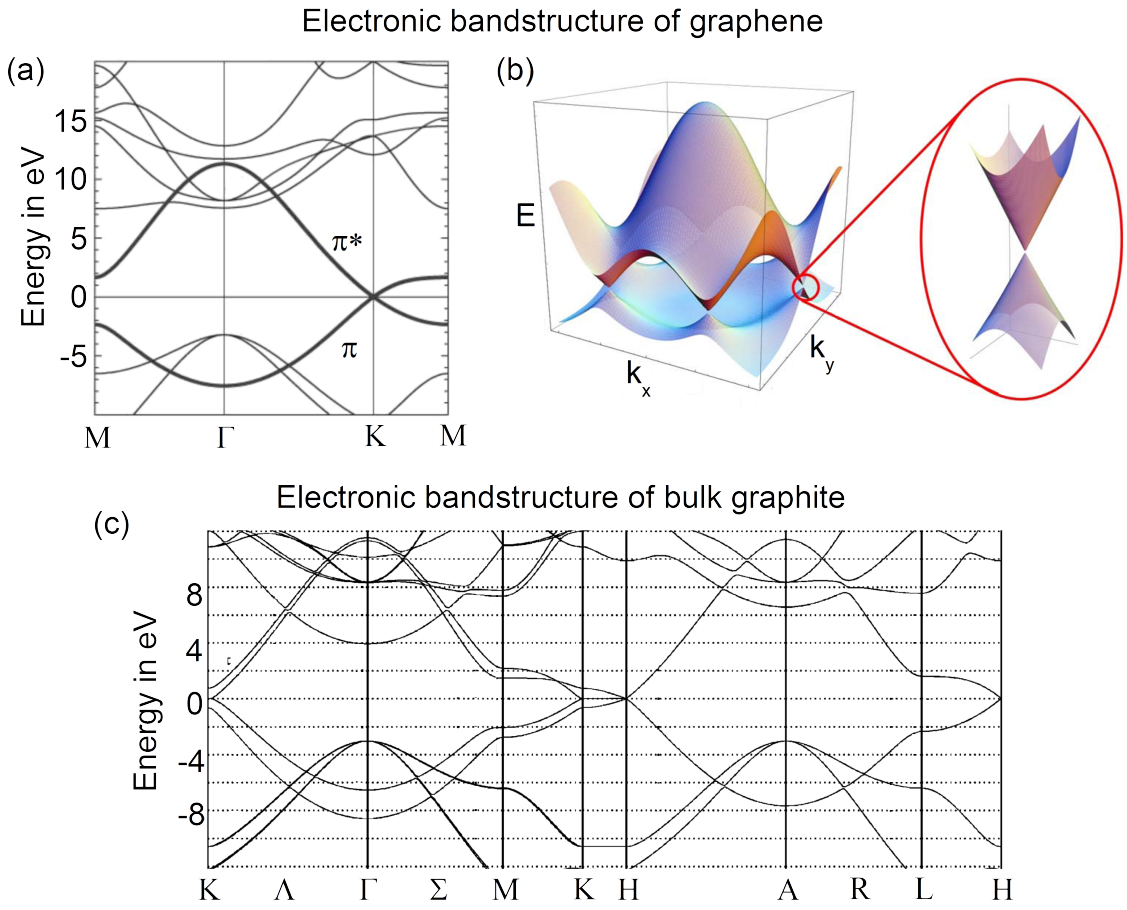

Figure 2.4: (a) Electronic bandstructure of graphene [26]. (b) The 3D-plot of π- and π'-band illustrates the Dirac cones at the K-point [23]. (c) The bandstructure of graphite does not show the show the cone structure. Interlayer coupling leads to split energy bands [27].

2.2.3 Dynamics of Optically Excited Charge Carriers in Graphene

The last two chapters wrapped up the unique physical properties of graphene. Especially the bandstructure within 1.5 eV around the Fermi level for undoped graphene causes many interesting phenomena. The basis for the understanding of graphene-light interaction lies in the understanding of the charge carrier dynamics in this energy regime. First, the interaction possibilities of single optically excited electron will be listed. Afterwards, the interaction of a few and many excited electrons will be discussed. The chapter ends up by reviewing the collective electron plasma oscillations, i.e. plasmons in graphene.

Similar to semi-conductors, an electron-hole pair can be created when graphene absorbs a photon. The energy gained by the electron when it jumps from the valence to the conduction band has to match the photon energy. The momentum of the photon is typically unimportant because of the much larger electron momentum. A similar excitation is possible when two photons are absorbed instantaneously. In this case the sum of the energy of two photons has to match the transition condition. However, both processes give an excited electron-hole pair which can undergo several transitions. The special case of two-photon luminescence will be

discussed later on in chapter 2.3.1.

After excitation, electron and hole can interact e.g. with phonons. By emission of phonons, electron and hole can relax toward the Dirac point. Generally, all processes underlie the principle of conservation of both energy and momentum. As long as the charge carriers remain in the same band the transitions are called intraband transitions. The red arrows in figure 2.5 (a) point out this situation.

Another possibility is the transition to a second Dirac cone in reciprocal space. This requires a larger momentum carried away by the phonon and is called an intervalley transition (figure 2.5 (a), lower blue arrow). Finally the electron or the hole can transit to the opposite band (figure 2.5 (a), upper blue arrow). These interband transitions can also occur as interband intervalley transition (figure 2.5 (a), green arrow).

All transitions do not necessarily require a phonon. Coulomb interaction between electrons and/or holes induce similar transitions. The arrows in figure 2.5 (b) point out the corresponding mechanisms. Similar to the phonon channels, the colors mark intraband, interband and intervalley transitions. In the following the situation of multiple excited charge carriers will be discussed. The ongoing physics however, consists of the former mentioned scattering and relaxation channels [28].

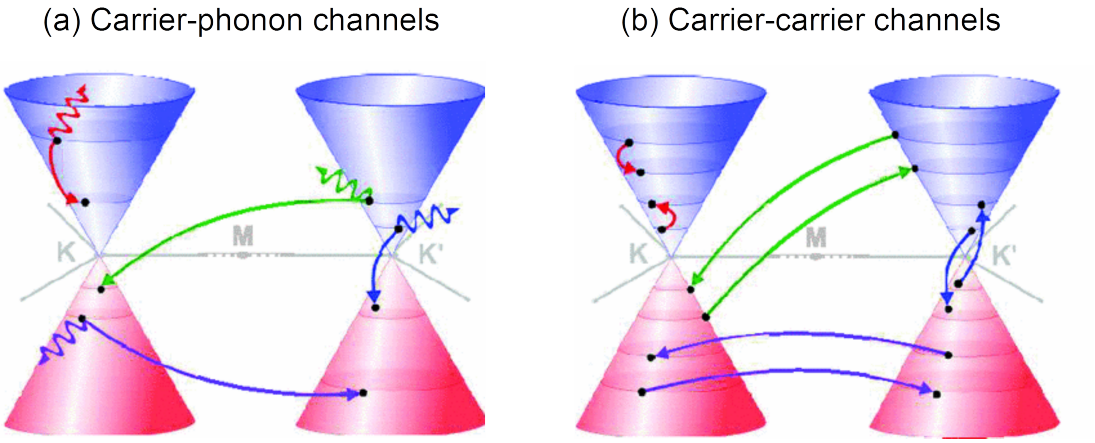

Figure 2.5: (a) Carrier-phonon and (b) carrier-carrier channels for excited charge carriers within the Dirac cone. For all transitions, energy and momentum must be conserved. The interplay of all channels determines the relaxation of one single electron or an electron gas [28].

Methods of statistical physics have to be used when more than a few excited electrons are involved. When many electrons are excited, e.g. by a strong and spectrally broad laser pulse, a hot electron gas is created. The temporal evolution of the carrier distribution is calculated by E. Malic et al. and is shown in figure 2.6. After a short time of $\sim 150\,\mathrm{fs}$ the electron gas is thermalized. Afterwards it takes picoseconds to cool down. The relaxation dynamics are determined by Coulomb- and phonon induced intra- and interband scattering [28].

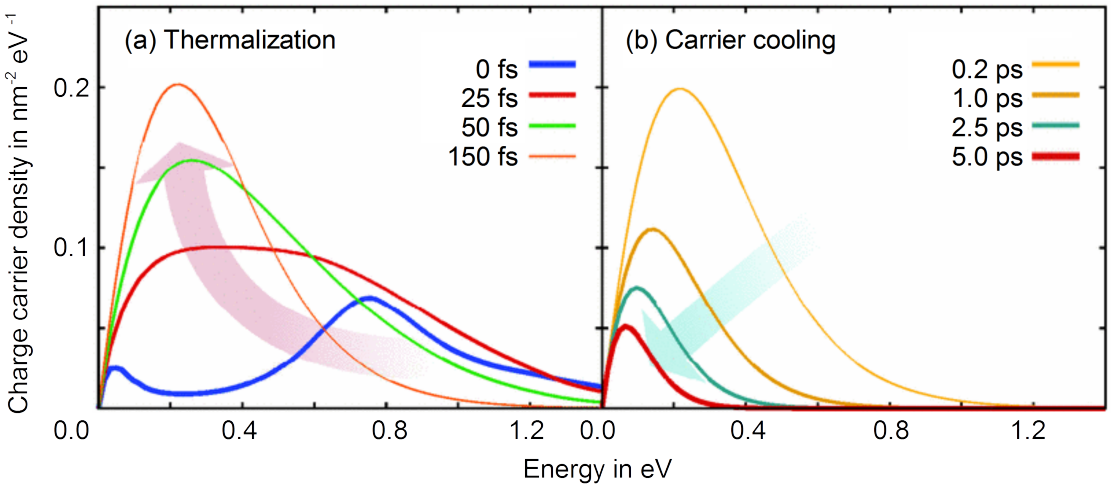

Figure 2.6: Charge distribution shortly after intense excitation. The electron gas thermalizes within 10s of femtoseconds (a) and cools down within picoseconds (b). The interaction and relaxation is determined by electron-electron and electron-phonon channels [28].

All the above mentioned excitations are single particle excitation even when they are treated statistically. Beside them, there are collective excitations. Since there are free charge carriers, one can think of oscillations of their density. Furthermore, graphene itself can be seen as a surface or a thin film and therefore one can expect collective modes similar to the SPPs described in chapter 2.1. Indeed, there are several reports on plasmons in graphene. Similar to the single electron excitation, one has to distinguish between collective inter- and intraband excitations according to a high- and a low energy regime, respectively.

In the high energy regime there are the so called π and $\pi + \sigma$ excitations at 4.9 eV and 15.4 eV. They occur as peaks in the loss function obtained from electron energy loss spectroscopy. These excitations are claimed to be plasmons in analogy to plasmons in bulk graphite at the same energy [29]. Nevertheless if they are actually collective or just single electron excitations has been discussed recently [30].

On the other hand, there is the low energy regime. The interaction of graphene with light of the near or mid infrared spectrum generates charge carriers within the π and π' bands which can be described by the cone approximation. In this energy regime shifting of the Fermi level strongly influence possible interactions. When the Fermi level is shifted from 0 to E_F a photon energy of $2E_F$ is required to excite a single electron. Otherwise Pauli blocking suppresses the transition. This is not the case for a plasmonic mode. Shifting of the Fermi level opens a gap for a pure plasmonic excitation. This phenomenon is extensively studied by Frank H. L. Koppens, F. Javier García de Abajo et al. [31]. In their model, a graphene monolayer is bound to a surface. Vacuum acts as the superstrate. The Fresnel reflection coefficients are derived from the boundary conditions of electric and magnetic field for incoming plane waves. From the pole of the reflection coefficient for a p-polarized wave, the dispersion of the plasmon is implicitly given by the equation

$$\frac{\epsilon_0 \epsilon_{sub}}{\sqrt{\epsilon_{sub} k_0^2 - k_{SP}^2}} + \frac{\epsilon_0}{\sqrt{k_0^2 - k_{SP}^2}} = -\frac{\sigma}{\omega} \tag{2.18}$$

with graphenes sheet conductivity σ, the substrate's permittivity ϵ_{sub} and the vacuum photon wave vector $k_0 = \omega/c$. The plasmon wave vector k_{SP} can expressed within the common limit $k_{SP} \gg k_0$ by

$$k_{SP} \approx (\epsilon + 1)\epsilon_0 \omega \frac{i}{\sigma}. \tag{2.19}$$

This equation links the plasmon wave vector with the sheet conductivity of graphene. Obviously, an oscillating propagating SPP requires a non vanishing imaginary part of the sheet conductivity.

Koppens et al. [31] go on with the derivation of the sheet conductivity using methods of statistical physics. From a tight binding approach (TBA) and random-phase approximation (RPA) follows

$$\sigma(\omega) = \frac{e^2 E_F}{\pi\hbar^2} \cdot \frac{i}{\omega + i\tau^{-1}} + \frac{e^2}{4\hbar} \cdot \left[\theta(\hbar\omega - 2E_F) + \frac{i}{\pi} \cdot \log\left|\frac{\hbar\omega - 2E_F}{\hbar\omega + 2E_F}\right|\right] \tag{2.20}$$

with a relaxation time $\tau \sim 10^{-13}$ s and the Heaviside step function θ. The resulting plasmon dispersion curve is plotted together with the allowed single electron transition in figure 2.7. According to this model plasmons are only predicted at the energy regime of and below the doping level. Therefore these kind of plasmons cannot appear in the visible spectral range since a sufficiently high doping can probably not be achieved [32]. This give rise to the assumption that graphene is completely plasmonic inactive within the visible spectral range.

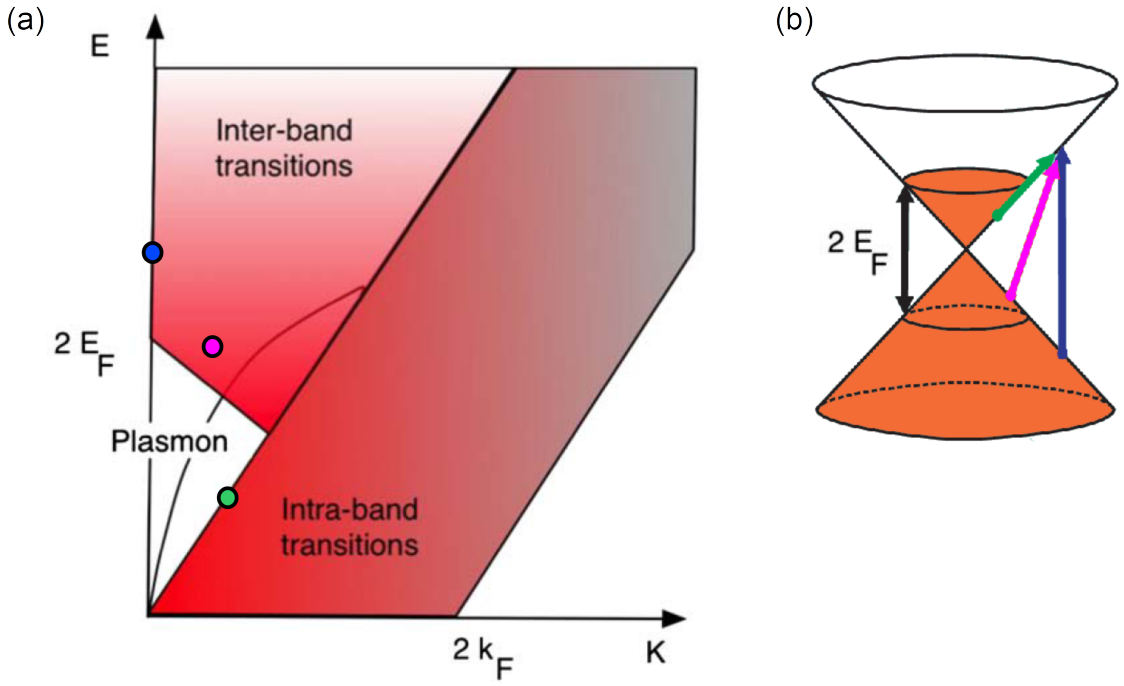

Figure 2.7: (a) Possible transfer of energy and momentum for electronic excitations in doped graphene. Doping graphene by the energy E_F opens a gap where only plasmonic excitations exist and electron-hole excitation is suppressed by Pauli blocking [23]. (b) The situation is visualized through the Dirac cone. The colored arrows correspond to the dots in (a), respectively. Shifting the Fermi level by E_F blocks transitions below $2E_F$ when no momentum is transferred [31].

In contrast, sufficiently high imaginary part of the sheet conductivity is predicted by density functional theory (DFT) based calculations [11]. Furthermore, measurements by electron energy loss spectroscopy (EELS) [9] and ellipsometry [10] confirm a comparable high imaginary part of the sheet conductivity $\Im(\sigma)$. This is in contrast to TBA+RPA based calculations and absorption measurements [33]. Lange et al. [2] coupled rhodamine 6G molecules to graphene and measured the quenching due to the interaction with graphene. They derived a theoretical quenching factor either with coupling to plasmons or without. Their result as well as their calculations based on other measurements follow clearly the predictions according to the existence of plasmons. The plasmons appear to be spatially localized, in the visible spectral range and with a line width of 0.1 eV. Anyway, the performed measurements within this work encounter only the case for this type of emitter in one specific distance.

Therefore, further methods have to be developed and further measurements have to be performed to answer the question if there are plasmons in the visible spectral range or not. Within this thesis nonlinear optical effects are used to probe among other things plasmons in the visible spectral range. The theoretical background is given in the next section.

2.3 Photon-Upconversion

2.3.1 Incoherent Upconversion

In general, upconversion describes the fact that light with a specific frequency is converted into light with a higher frequency. This can happen in various ways when light hits the surface of a medium or is guided through the bulk. It can be categorized in coherent and incoherent processes. Because the excitation is typically laser light the incoming photons are in a coherent state. The first section focuses on two-photon luminescence and upconversion scattering. Both processes lead to the emission of upconverted incoherent radiation.

Two-photon luminescence (TPL) describes the radiative decay after a two-photon absorption process (figure 2.8 (a)). The relaxation process is similar to that of fluorescence known e.g. from dye molecules. After exciting an electron, it can decay non-radiatively through vibrational levels and finally emits an photon when it transits back to the ground state. Of course, the whole spectrum of transitions is, in principle, possible. The advantage is to excite to energy levels which where not accessible from the ground state by an one-photon absorption. Since excitation and detection wavelength is well separated in two-photon luminescence one is able to detect in the immediate vicinity or resonantly at the excited energy level.

The excitation process can be explained by an instantaneous absorption of two photons. An electron transits through a virtual energy state and ends finally up in a real excited state. The absorption cross section ς of this excitation process scales linearly with the excitation intensity and one can write [34]

$$\varsigma = \varsigma^{(2)} I \tag{2.21}$$

where $\varsigma^{(2)}$ is a constant coefficient. Furthermore, the transition rate scales linearly with the cross section and the excitation intensity. One obtains

$$R = \varsigma I/\hbar\omega \tag{2.22}$$

$$= \varsigma^{(2)} I^2/\hbar\omega \tag{2.23}$$

From $R \propto I^2$ follows easily that the two-photon luminescence also scales as I^2. Depending on the prefactor $\varsigma^{(2)}$ this results show that for efficient two-photon luminescence high peak intensity of the excitation light source is required. By studying the incoherent emission, one can gain information about the energy level structure, transition rates etc.

Most of the non-radiative relaxation processes in solids are based on the excitation of vibrational modes. The excited phonon takes an amount of energy and the electron decays into a lower vibrational level. An alternative scattering process is Coulomb scattering of two electrons where one electron takes over an amount of energy from a second electron. Conservation of momentum and energy reduces the number of scattering possibilities. For instance, two electrons with energy E_i, $i = 1, 2$, and momentum $\vec{k_i}$ scatter and gain the energy ΔE_i and momentum $\Delta\vec{k_i}$, respectively. Hence,

$$(E_1 + \Delta E_1) + (E_2 + \Delta E_2) = E_1 + E_2 \tag{2.24}$$

$$\Leftrightarrow \Delta E_1 = -\Delta E_2 \tag{2.25}$$

and

$$\left(\vec{k_1} + \Delta\vec{k_1}\right) + \left(\vec{k_2} + \Delta\vec{k_2}\right) = \vec{k_1} + \vec{k_2} \tag{2.26}$$

$$\Leftrightarrow \Delta\vec{k_1} = -\Delta\vec{k_2}. \tag{2.27}$$

Combining the two equations yields

$$\frac{\Delta\vec{k_1}}{\Delta E_1} = \frac{\Delta\vec{k_2}}{\Delta E_2}. \tag{2.28}$$

When any exchange of momentum and energy is possible, the last equation can be further generalized to

$$\nabla_{\vec{k}} E = \text{const.} \tag{2.29}$$

Conclusively, efficient electron-electron scattering occur in solids with linear band structure. Figure 2.8 (b) depicts the situation were two photons of almost the same energy create two electron hole pairs. Both electrons and holes scatter and one electron hole pair raises energy. Recombination before another relaxation process can occur which leads to the emission of a photon. Apparently, the emitted photon carries a higher energy than one of the incident photons. The presented conical electronic dispersion curve can be applied to the band structure of graphene within the cone approximation.

Before discussing specifically the upconversion processes in graphene, the remaining coherent upconversion process will be discussed.

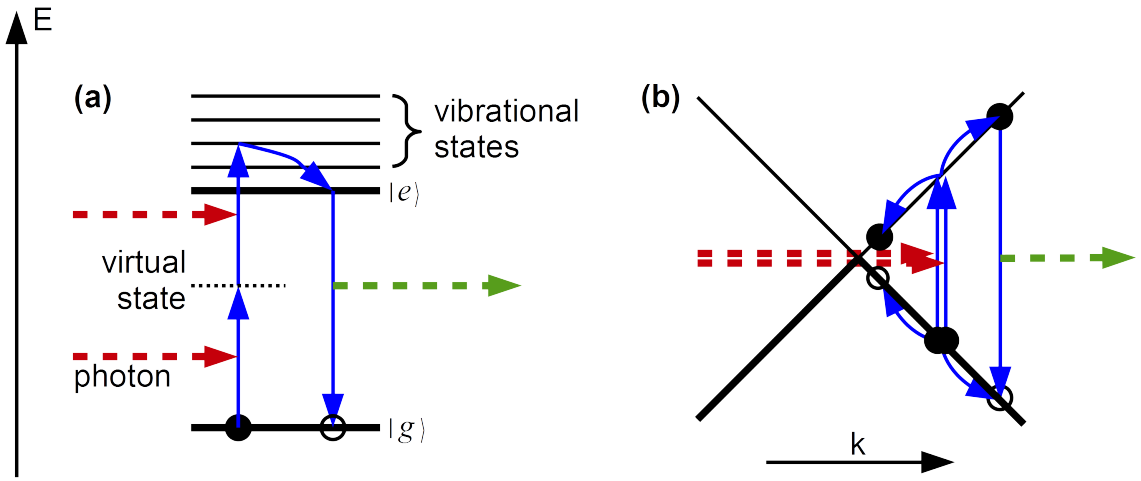

Figure 2.8: Incoherent upconversion processes. (a) Two-photon luminescence: Instantaneous absorption of two photons populates an excited state. Non-radiative and radiative relaxation lead to the emission with photon energies exceeding the excitation photon energies. (b) Efficient scattering between two excited charge carriers and recombination before relaxation can produce photons at higher energies. This process requires a linear band structure to be efficient.

2.3.2 Coherent Upconversion: Second Harmonic Generation

In contrast to two-photon luminescence, second harmonic generation is a coherent effect and does not require real energy states matching the photon energies (figure 2.9). In the photon picture, two photons cause a transition from a ground state into a first virtual state and at the same time from there to a second virtual state. Of course, the final virtual state is separated from the ground state by twice the incident photon energy. Instantaneously, a transition back to the ground state generates one photon with exactly this energy.

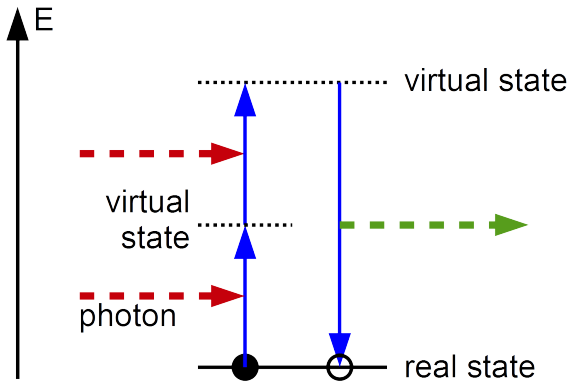

Figure 2.9: Second harmonic generation in the photon picture. The instantaneous absorption of two and emission of one photon converts the pump light coherently.

A classical approach to this topic is to describe the polarization $\tilde{P}(t)$ of the medium as nonlinear with respect to the electric field [34].

$$\tilde{P}^{(2)}(t) \quad = \quad \epsilon_0 \chi^{(2)} \tilde{E}(t)^2. \tag{2.30}$$

The second order nonlinear susceptibility $\chi^{(2)}$ is introduced. The tilde denotes fast oscillating terms in time. A non-vanishing $\chi^{(2)}$ leads to numerous effects. This can be demonstrated by writing the electric field as a sum of two components, each of them with its own frequency.

$$\tilde{E}(t) \quad = \quad E_1 e^{-i\omega_1 t} + E_2 e^{-i\omega_2 t} + c.c. \tag{2.31}$$

The fast oscillating contribution is presented by the exponential function, whereas the slowly varying envelope is hosted by E_1 and E_2, respectively. Plugging the electric field into equation 2.30 leads to the following nonlinear polarization:

$$\begin{array}{rcll|ll}
\tilde{P}^{(2)}(t) & = & \epsilon_0\chi^{(2)} & \tilde{E}(t)^2 & & \\
\tilde{P}^{(2)}(t) & = & \epsilon_0\chi^{(2)} & (E_1^2 e^{-2i\omega_1 t} + & \leftrightarrow P(2\omega_1) & \leftrightarrow SHG \\
 & & & +E_2^2 e^{-2i\omega_2 t} + & \leftrightarrow P(2\omega_2) & \leftrightarrow SHG \\
 & & & +2E_1E_2 e^{-i(\omega_1+\omega_2)t} + & \leftrightarrow P(\omega_1+\omega_2) & \leftrightarrow SFG \\
 & & & +2E_1E_2^* e^{-i(\omega_1-\omega_2)t} + & \leftrightarrow P(\omega_1-\omega_2) & \leftrightarrow DFG \\
 & & & +c.c.+ & & \\
 & & & +2E_1E_1^* + 2E_2E_2^*) & \leftrightarrow P(0) & \leftrightarrow OR
\end{array} \tag{2.32}$$

Each expression is labeled by the name of the physical process, i.e. second harmonic generation (SHG), sum frequency generation (SFG), difference frequency generation (DFG) and optical rectification (OR). The complex conjugated *c.c.* contains all responses at the negative of each frequency.

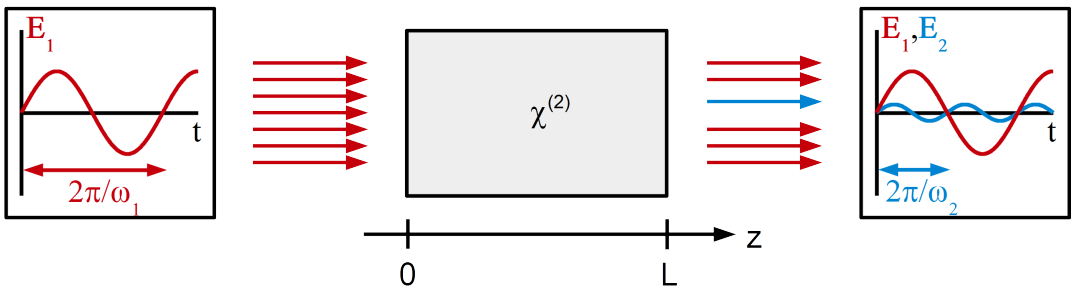

Figure 2.10: Bulk second harmonic generation. The nonlinear susceptibility $\chi^{(2)}$ causes the creation of a second electric field E_2. The incident field E_1 and E_2 propagate in z-direction and exchange energy over the whole length L.

Now, a mathematical description of second harmonic generation in a bulky medium will be given. The situation is shown schematically in figure 2.10. The electric field of the incident light of frequency ω_1 is denoted by $\tilde{E}_1(z,t)$. At $z = 0$ the field enters the medium and due to nonlinear susceptibility $\chi^{(2)}$ a second field $\tilde{E}_2(z,t)$ is induced which oscillates with frequency $\omega_2 = 2\omega_1$. Now, there are two fields traveling through the medium and exchange energy. One can start the description

similar to equation 2.31. In addition, the fast oscillating term can be expanded in time-dependent and space-dependent factors . The remaining terms are the slowly varying amplitudes $A_1(z)$ and $A_2(z)$.

$$\begin{aligned}
\widetilde{E}(z,t) &= \widetilde{E}_1(z,t) + \widetilde{E}_2(z,t) && (2.33)\\
\widetilde{E}(z,t) &= E_1(z)e^{-i\omega_1 t} + E_2(z)e^{-i\omega_2 t} + c.c. && (2.34)\\
\widetilde{E}(z,t) &= A_1(z)e^{ik_1 z}e^{-i\omega_1 t} + A_2(z)e^{ik_1 z}e^{-i\omega_2 t} + c.c. && (2.35)
\end{aligned}$$

$k_j = n_j\omega_j/c$ is the wave vector in z-direction and n_j is the refractive index at frequency ω_j. The refractive index is determined by the materials relative permittivity as $n_j = \sqrt{\epsilon^{(1)}(\omega_j)}$.

Each component of the electric field has to fulfill the driven wave equation

$$\frac{\partial^2 \widetilde{E}_j}{\partial z^2} - \frac{\epsilon^{(1)}(\omega_j)}{c^2}\frac{\partial^2 \widetilde{E}_j}{\partial t^2} = \frac{1}{\epsilon_0 c^2}\frac{\partial^2}{\partial t^2}\widetilde{P}_j. \quad (2.36)$$

This differential equation connects the components of the electric field with their induced polarization. For the two field components there are two polarization components P_1 and P_2 oscillating with frequency ω_1 and ω_2, respectively. Together, the two components form the nonlinear polarization

$$\begin{aligned}
\widetilde{P}^{NL}(z,t) &= \widetilde{P}_1(z,t) + \widetilde{P}_2(z,t), && (2.37)\\
\widetilde{P}^{NL}(z,t) &= P_1(z)e^{-i\omega_1 t} + P_2(z)e^{-i\omega_2 t} + c.c. && (2.38)
\end{aligned}$$

Now one can identify the underlying physical process leading to the nonlinear response of the medium. In contrast to equation 2.32 where two arbitrary fields where obtained, there are two specific fields. Thus, the two components of the polarization can be expressed by the electric fields via

$$\begin{aligned}
P_1(z) &= 2\epsilon_0\chi^{(2)}E_2E_1^* && (2.39)\\
&= 2\epsilon_0\chi^{(2)}A_2A_1^*e^{i(k_2-k_1)z}, && (2.40)\\
P_2(z) &= \epsilon_0\chi^{(2)}E_1^2 && (2.41)\\
&= \epsilon_0\chi^{(2)}A_1^2e^{2ik_1z}. && (2.42)
\end{aligned}$$

Plugging the obtained results into 2.36 lead to coupled equations for the amplitudes

$$\begin{aligned}
\frac{dA_1}{dz} &= \frac{8\pi i\omega_1^2 d_{eff}}{k_1 c}A_2A_1^*e^{-i(2k_1-k_2)z}, && (2.43)\\
\frac{dA_2}{dz} &= \frac{4\pi i\omega_2^2 d_{eff}}{k_2 c}A_1^2e^{i(2k_1-k_2)z}. && (2.44)
\end{aligned}$$

Finally, the undepleted pump approximation appears suitable. Assuming that only a small fraction of the intense incident light field is converted leads to $A_1 \simeq const.$ Immediate integration $\int_0^L dz...$ and the fact that$A_2(z=0) = 0$ give

$$A_2(z=L) = 4\pi \cdot d_{eff} \cdot A_1^2 \cdot \frac{\omega_2^2}{k_2} \cdot \frac{e^{i(2k_1-k_2)L}-1}{(2k_1-k_2)}. \quad (2.45)$$

The total intensity $I = I_1 + I_2$ consists of $I_j = \frac{n_j c}{2\pi} |A_j|^2$. Consequently the intensities follow the proportionality

$$I_2 \propto |A_2|^2 \propto |A_1|^4 \propto I_1^2. \tag{2.46}$$

Consequently, a second order nonlinear effects is more sensitive to the excitation intensity than a linear optical process. This relation can be used to verify if an observed emission is due to second harmonic generation.

This description is a completely classical wave description of light. The obtained equations have interpretations in the photon picture. Without going deep into the quantum mechanical description of SHG, the last equation and the related proportionality should be discussed. In the photon picture, two photons are converted into one photon. This process has to fulfill conservation of energy and momentum. The proportionality between input and SHG intensity describes the conservation of energy. Always two photons, i.e. two quanta of energy, are needed to create one photon of doubled energy. Since the number of photons can be seen as proportional to the classical intensity this leads directly to the squared dependence. The conservation of momentum, i.e. the conservation of the sum of all photon k-vectors, means that the SHG process can occur only when the sum of the two input k-vectors sum up to the k-vector of the SHG photon. Treating the photon as a wave packet of finite size in k-space, this statement transform to a statement of transition probability. Due to the finite size of the wave packet, the probability has its maximum when the condition is perfectly fulfilled, i.e. the two input wave packets overlap completely. It decreases towards all other cases.

In the classical picture, this means one gets a maximum of SHG intensity when the k-vectors match and a strongly damped intensity for a small mismatch. This statement is expressed in the last term of equation in equation 2.45 which is of the form $(e^{ix} - 1)/x$. For $2k_1 = k_2$, i.e. $x = 0$, the absolute value of the term is 1. For other x, the denominator induces a decrease of the absolute value and a change in phase. Hence, the SHG intensity is reduced [34].

2.3.3 Surface Plasmon Enhanced Second Harmonic Generation on Silver Films [35]

In the purely classical description, the strength of the second harmonic generation depends on $\chi^{(2)}$. It is typically a constant of a material and depends, among other things, on the crystal structure. Assuming a centrosymmetric crystal, one expect a nonlinear polarization $\tilde{P}^{NL}(t)$ for an electric field $E(t)$ and $-\tilde{P}^{NL}(t)$ for $-E(t)$. Using equation 2.30 for both cases leads to

$$\tilde{P}^{NL}(t) = \epsilon_0 \chi^{(2)} \left(\tilde{E}(t)\right)^2, \tag{2.47}$$

$$-\tilde{P}^{NL}(t) = \epsilon_0 \chi^{(2)} \left(-\tilde{E}(t)\right)^2. \tag{2.48}$$

Obviously, both polarizations have the same expression which is for a non-vanishing electric field only possible when

$$\chi^{(2)} = 0. \tag{2.49}$$

Consequently, second harmonic generation is not expected from centrosymmetric crystals [34].

Crystalline silver has the space group $Fm\bar{3}m$ and is therefore a centrosymmetric crystal. Second harmonic generation is not expected when light travels through the bulk of a silver crystal. In contrast second harmonic generation is observed when a light field interacts with the surface. At the interface the inversion symmetry is broken and SHG becomes possible. It seems reasonable that SPPs influence this effect. This chapter focuses on the work by H.J. Simon et al. In 1974, they reported the first experimental and theoretical investigations of the coupling of SHG to surface-plasmon mode in a silver film [35].

A silver film on a glass substrate in an attenuated total reflection Kretschmann configuration is used (see figure 2.11 (a)). Light from a ruby laser ($\lambda = 694.3$nm) is guided through the glass prism and is reflected at the silver covered surface at an angle of incidence θ. The evanescent field penetrates into the silver and reaches the opposite silver-air interface. The component of the photon wave vector parallel to the silver-air interface is expressed by

$$k_{||} = \frac{\omega}{c} \cdot n \cdot \sin\theta \tag{2.50}$$

with n being the refractive index of the glass and ω and c the angular frequency and the speed of light in vacuum, respectively. Inserting silver's dielectric function ϵ into equation 2.10 gives the SPP dispersion:

$$k_{SPP} = \frac{\omega}{c}\sqrt{\frac{\epsilon}{\epsilon+1}}. \tag{2.51}$$

A SPP mode is excited when the wave vectors match. Hence, the condition

$$n \sin\theta_P = \sqrt{\frac{\epsilon}{\epsilon+1}} \tag{2.52}$$

must be fulfilled. Indeed, scanning θ causes a dip in the reflected light at the plasmon angle θ_P due to the excitation of the plasmon at the silver-air surface.

At every angle of incidence, a small amount of light is converted to the second harmonic at the glass-silver interface due to the broken symmetry. Additionally enhancement of the SHG is observed when θ reaches θ_P. The data is plotted in figure 2.11 (b). The excited fundamental plasmon mode leads to an resonant enhancement of the fundamental electric field. Thus, a large nonlinear polarization is induced at the silver-air surface which in turn causes a resonantly enhanced emission of the second harmonic. Simon et al. express the total reflected harmonic intensity $I(2\omega)$ by the reflected harmonic electric field amplitude $E_R^{(2\omega)}$ evaluated for an infinitely thick silver film and the nonlinear plasmon Fresnel factor F_{NLP}:

$$I(2\omega) = \frac{cn^{(2\omega)}}{8\pi}\left|E_R^{(2\omega)} F_{NLP}\right|^2 \tag{2.53}$$

with

$$\begin{aligned} F_{NLP} \;=\; & \frac{\left(1 - {r_{sa}^{(\omega)}}^2 \mathrm{e}^{-2k^{(\omega)}d}\right) \cdot \left(1 - r_{sa}^{(2\omega)} \mathrm{e}^{-k^{(2\omega)}d}\right)}{\left(1 + r_{gs}^{(\omega)} r_{sa}^{(\omega)} \mathrm{e}^{-k^{(\omega)}d}\right)^2 \cdot \left(1 + r_{gs}^{(2\omega)} r_{sa}^{(2\omega)} \mathrm{e}^{-k^{(2\omega)}d}\right)} \\ & - \frac{\left(\frac{\epsilon^{(\omega)}-1}{\epsilon^{(\omega)}-{n^{(\omega)}}^2}\left(1 - {r_{sa}^{(\omega)}}^2\right) \mathrm{e}^{-k^{(\omega)}d} \cdot \mathrm{e}^{-\frac{1}{2}k^{(2\omega)}d}\left(1 + r_{sa}^{(2\omega)}\right)\sqrt{\epsilon^{(2\omega)}}\right)}{\left(1 + r_{gs}^{(\omega)} r_{sa}^{(\omega)} \mathrm{e}^{-k^{(\omega)}d}\right)^2 \cdot \left(1 + r_{gs}^{(2\omega)} r_{sa}^{(2\omega)} \mathrm{e}^{-k^{(2\omega)}d}\right)}. \end{aligned} \tag{2.54}$$

The r's refer to the Fresnel reflection coefficients for the glass-silver (gs) and the silver-air (sa) interface, the k's to silver's absorption coefficient, the n's to the refractive index of the glass prism and d is the thickness of the silver film. The respective values correspond either to the fundamental or the harmonic frequency which is expressed in the superscript.

The first term of equation 2.54 describes the SHG at the glass-silver interface and the second term at the silver-air interface. For plausibility, one can assume an infinite thick silver film resulting in $F_{NLP} = 1$ and the whole SHG is defined by $E_R^{(2\omega)}$ in equation 2.53. In contrast a finite thin silver film can induce enhanced emission. This enhancement was firstly reported in the presented paper by Simon et al.[35].

It has been shown that SPPs couple to second harmonic generation under special circumstances. Consequently the enhancement of SHG can be used as a probe for SPP modes. This justifies the investigation of SHG with regard to the question if plasmonic modes are present or not. This thesis shed light on the question, if plasmonic modes in graphene are present. The special case of SHG will be further discussed in the result part of this thesis.

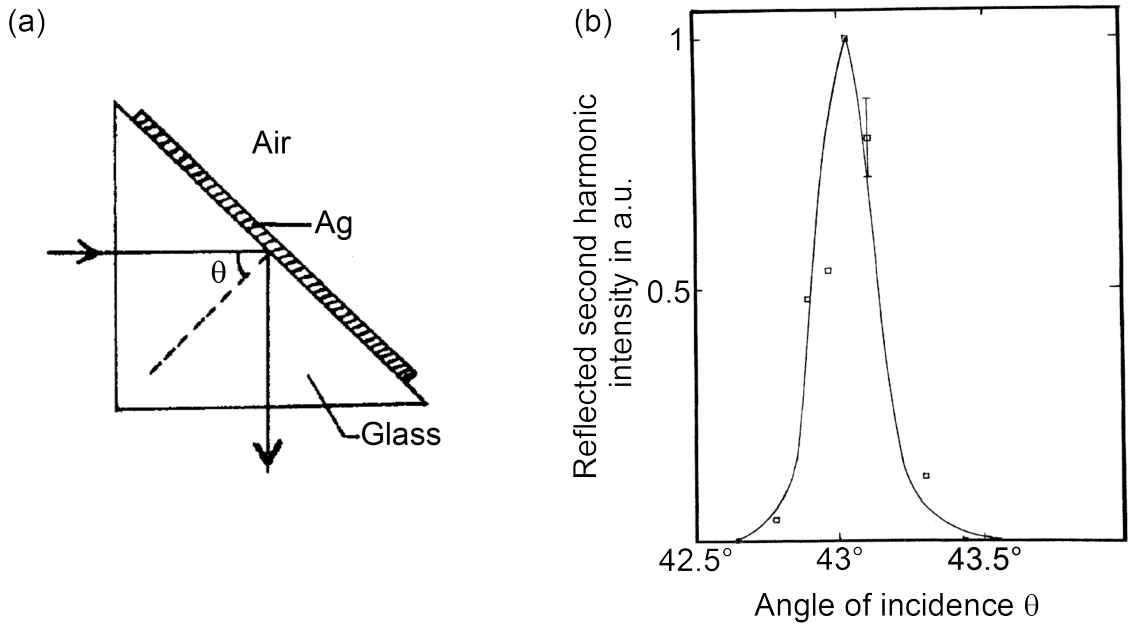

Figure 2.11: (a) Geometry of the attenuated total reflection Kretschmann configuration. Coupling to the SPP mode induce an enhancement of the SHG. (b) The detected second harmonic light is strongly enhanced at the plasmon angle [35].

2.3.4 Investigating the Plasmonic LDOS of Gold Nanoprisms [36]

In 2013, Viarbitskaya et al. reported on a TPL based microscopy method to probe the surface plasmon local density of states (SP-LDOS) inside thin gold nanoprisms [36]. The setup is comparable to the setup used in this thesis. For polarization switching a $\lambda/2$ plate is set in front of the beamsplitter. The samples composes of 0.5-1 μm gold platelets with triangular or hexagonal shape and 20nm thickness on a glass substrate. By moving the sample through the focused laser beam an

upconversion process appears, i.e. two-photon luminescence. The observed TPL is strongly affect by the plasmon modes within the gold plates. The intensity of luminescence is directly linked to the SP-LDOS.

By exciting the gold plate with circular polarized light at a frequency ω_0 and a beam waist at $\vec{R_0}$ the emitted two-photon luminescence intensity can be written as

$$I_{TPL}(\vec{R_0}, \omega_0) = \eta^2(\omega_0) \int_V |\vec{E}(\vec{R_0}, \vec{r}, \omega_0)|^4 d\vec{r} \tag{2.55}$$

where $\vec{E}$ is the local electric field distribution and η is the nonlinear coefficient corresponding to the second order nonlinear optical process. A general relation links the light field intensity $|\vec{E_0}(\vec{R_0}, \vec{r}, \omega)|^2$ with the local field intensity $|\vec{E}(\vec{R_0}, \vec{r}, \omega)|^2$ and the SP-LDOS $\rho_{||}(\vec{r}, \omega_0)$ at any arbitrary point $\vec{r}$ inside the metal:

$$|\vec{E}(\vec{R_0}, \vec{r}, \omega)|^2 = |\vec{E_0}(\vec{R_0}, \vec{r}, \omega)|^2 \pi^2 \omega_0^2 A^{-1} \rho_{||}(\vec{r}, \omega_0). \tag{2.56}$$

Plugging this into formula 2.55 leads to

$$I_{TPL}(\vec{R_0}, \omega_0) = \eta^2(\omega_0) \pi^4 \omega_0^4 A^{-2} \int_V |\vec{E_0}(\vec{R_0}, \vec{r}, \omega)|^4 \rho_{||}^2(\vec{r}, \omega_0) d\vec{r}. \tag{2.57}$$

This shows that the TPL intensity is a convolution of the incident beam profile with the squared SP-LDOS. Consequently, an I_{TPL}-map converge towards the SP-LDOS map for decreasing beam waist. In addition, TPL is only expected where the SP-LDOS $\rho_{||}^2$ is different from zero. Figure 2.12 presents the simplified setup (a) and a scanning electron micrograph of one of the gold plates on the glass substrate (b). (c) shows the corresponding TPL scan. The standing wave patterns along the edges appear clearly. As described in the former equation the resolution is limited by the beam waist.

The modulation of the TPL signal and the direct mapping of the SP-LDOS might be a powerful tool for spatial investigations of flat plasmonic structures. It is just obvious to think about transferring the method to graphene structures. This justifies the analysis of the optical upconversion process in graphene. Before the results will be discussed the next chapter wraps up what is so far reported on the nonlinear response of graphene.

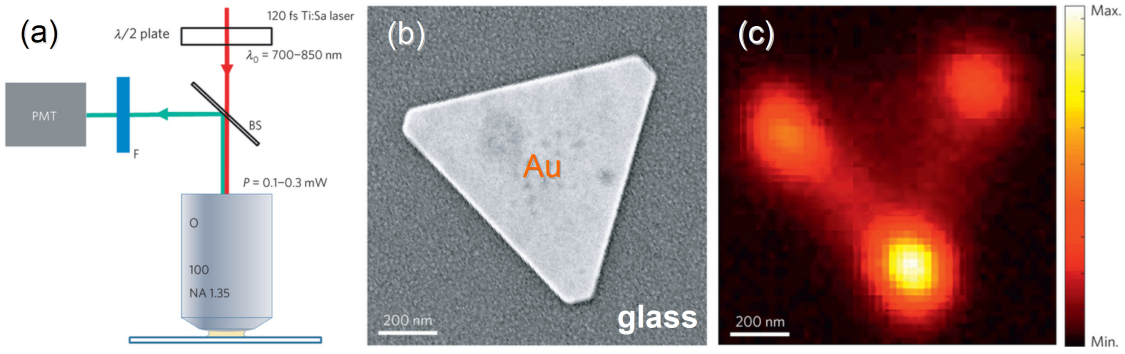

Figure 2.12: (a) The setup presented to investigate the surface plasmon local density of states of gold nano prisms is comparable to the setup presented used this thesis. (b) The scanning electron micrograph of such a gold plate clearly corresponds to the spatial dependent two-photon luminescence. (c) The standing wave patterns of the plasmon modes are clearly visualized by TPL [36] .

2.3.5 Reports on Nonlinear Optical Behavior of Graphene

As discussed in chapter 2.3.1 nonlinear effects appear due to a nonlinear macroscopic polarization. This polarization is determined by the nonlinear susceptibility tensor. Several publications have focused on the coherent optical response of graphene with regard to $\chi^{(2)}$- and $\chi^{(3)}$-processes. For instance, E. Hendry et al. [37] who set up a four-wave mixing experiment and found a significant large third-order optical susceptibility. The current thesis concentrate more on second order and upconversion channels in the range of 1...2.5 times the excitation energy.

Most comparable to the measurements presented in this thesis are those by Wei-Tao Liu et al. [1]. Femtosecond laser pulses were used to study upconversion luminescence from graphene. After excitation, emitted light with photon energies which exceeding those of the laser was found. The spectral broad emission was also used to map graphene and thin graphitic sheets. Figure 2.13 (a) shows a white light microscopy image of their sample and (b) the corresponding upconversion image. Luminescence is detected from sheets down to a monolayer with a clear layer contrast. In (c) the excitation fluence dependence of the luminescence is plotted for different excitation photon energies. The slope is determined to be between 2 and 3. The upconversion spectra for several excitation energies are shown in (d). All have in common that the position of the maximum is defined by the edge of the shortpass filter. Towards higher photon energies, the signal decreases. This is different from the two-photon luminescence from gold (shown in grey). The origin of graphene's upconversion is assigned to be efficient upward scattering of electrons as described in chapter 2.3.1. Two-photon luminescence is excluded by citing the result of pump-probe measurements[38]. Herein the change of graphenes transmission after excitation is studied. While this effect appeared to be linear with pump power, TPL was designated to be not dominant. The excitation fluence lay in a range of 0.1 to $1\,\mu\mathrm{J/cm^2}$ in [1] and up to $200\,\mu\mathrm{J/cm^2}$ in [38].

Similar physical processes were studied by Chun Hung Lui et al. [39]. They performed a two pulse experiment at $\sim 827\,\mathrm{nm}$ wavelength for time dependent analysis. They also present an upconversion spectrum (figure 2.13(e)) which looks similar to the former mentioned. Additionally, a blackbody and temperature based model for the luminescence is derived. As a result, the luminescence is explained by thermal radiation from an up to 3000 K hot electron gas. The efficient scattering leads to the fast thermalization and interaction with strongly coupled optical phonons to the relaxation.

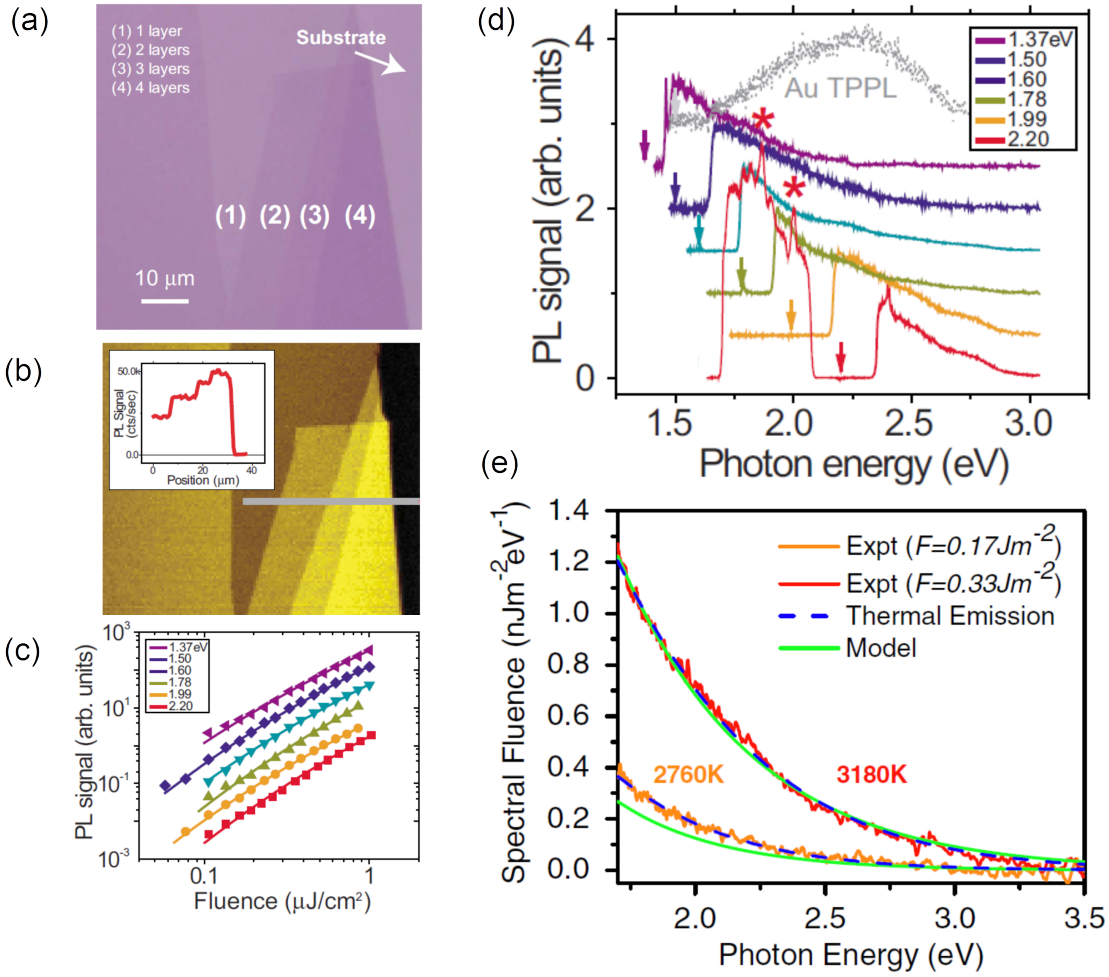

Figure 2.13: (a) White light microscopy of a graphene sample. (b) An upconversion scan of the same area. (c) The upconversion luminescence increases with the second to the third power of the excitation power. (d) The luminescence spectrally exceeds the excitation and decreases monotonically towards higher photon energies. These differ from gold two-photon luminescence. (a-d) were adopted from [1]. (e) Upconversion spectrum of graphene, adopted from [39]. The emission was found to behave like a blackbody at $\sim 3000\,\mathrm{K}$.

Beside the incoherent upconversion that behaves like thermal radiation, there are a few reports on second harmonic generation in graphene. Two publications by Jesse J. et al. focus on this $\chi^{(2)}$-process [40, 41]. They studied graphene samples mounted on Si/SiO_2 and excited with laser pulses of 800nm wavelength and 150 fs duration. The emission passed a bandpass at half of the excitation and was detected using a photomultipliertube. The lattice symmetry of substrate and graphene has a direct impact on the second harmonic generation. Therefore, the SHG from graphene in contrast to graphitic films and the substrate was measured dependent on the azimuthal rotational angle of the sample. Bulk contributions were neglected within the thin film limit. The SHG is expected only from surfaces and interfaces. The surface contribution from 15-layer down to bilayer graphene shows a threefold rotational symmetry according to their C_{3v} surface symmetry group. Crossed excitation and detection polarization exhibit even the full sixfold periodicity as shown in the green and blue curve in figure 2.14.

Graphene on a substrate has C_{6v} symmetry. Thus dipolar SHG is permitted for the reasons explained in detail in chapter 2.3.3. However, a small isotropic contribution is reported to be possible. The same holds for the Si/SiO_2 interface. Conclusively, the fourfold symmetry SHG from the bare substrate (black curve) arises from bulk Si electric quadrupole/magnetic dipole sources. Finally, the isotropic offset of the red curve is interpreted as the SHG from a graphene monolayer [40]. Nevertheless, neither in this publication nor in any other, a spectrum of the frequency doubled light is given. Furthermore, strong excitation can create upconverted light at twice the excitation energy which is not SHG. This will be described in chapter 4.3.3.

This motivates a deeper analysis as performed in this thesis. When SHG from graphene would be understood and controlled further inside could be gained also into plasmonic excitations in graphene.

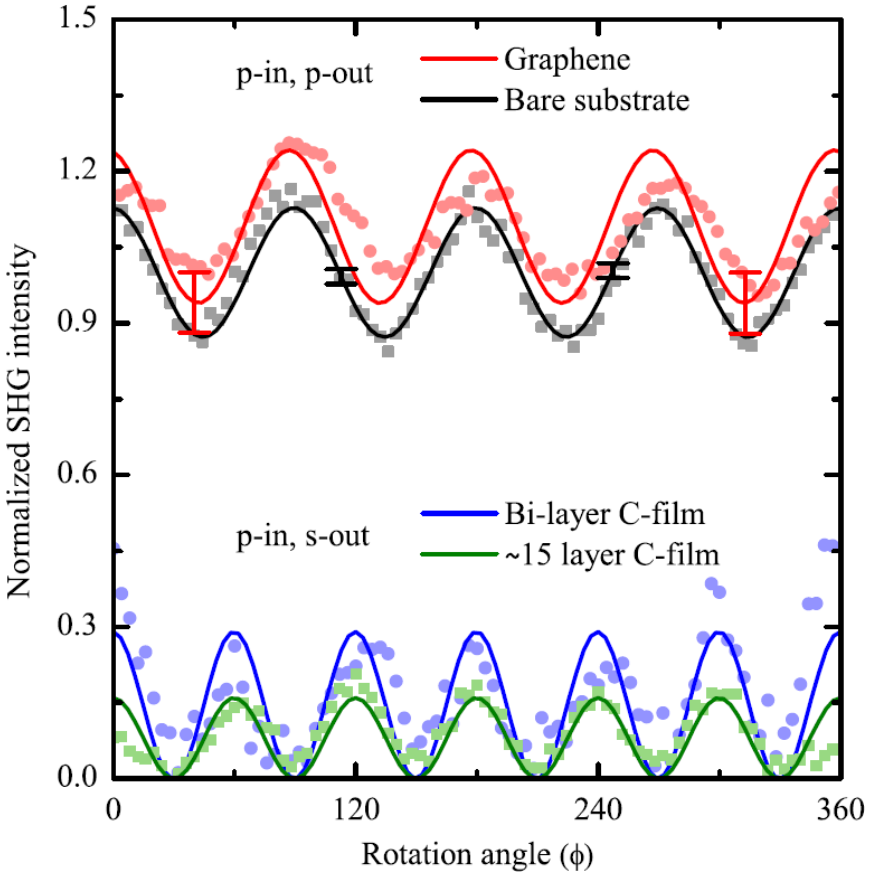

Figure 2.14: The crystal symmetry at the surface affects the SHG with regard to the polarization [40]. The anisotropy allows to distinguish between substrate (black) and multilayer or bilayer graphene (green and blue). The contribution from monolayer graphene (red) is the isotropic offset on the substrate's response.

3 Experimental and Technical Realization

The investigation of the upconversion processes in graphene described in the last chapter requires a well characterized setup and distinct knowledge about the properties of the samples. Firstly, the sample preparation as well as two characterization methods will be discussed. Secondly, the developed confocal scanning and spectroscopy setup will be presented. The reliability of the data is ensured by characterization of every optical component. To this end the spectral correction function which is necessary for the analysis of spectrally broad luminescence will be given. The principle of atomic-force microscopy is briefly described since it is used for further analysis.

3.1 Samples: Graphene on Mica

3.1.1 Exfoliated Graphene on Muscovite Mica

A simple but effective method for the production of 2D graphene is mechanical exfoliation of freshly cleaved bulk graphite crystals. The graphene samples used in this thesis were obtained from highly orientated pyrolytic graphite and deposited onto a mica substrate with a lateral dimension of 1 to 3 cm. All samples were provided by members of the group of Prof. Rabe (Department of Physics, Humboldt-Universität zu Berlin). The samples were produced in a nitrogen flushed glove box and were stored under ambient conditions.

When highly orientated pyrolytic graphite is freshly cleaved, smaller graphite structures protrude out of the crystal. They can either be grabbed with tweezers or the whole crystal can be put top down on mica. Now, the van-der-Waals interaction between mica and graphite layers can be higher than between adjacent graphite layers. By removing the crystal, small and thin graphite structures remain on the surface. Afterwards, optical methods can be used to characterize the graphite structures. The flakes typically have lateral dimensions between a couple of micrometers for single- and fewlayer graphene and up to 1mm for multilayer graphene and graphite.

The mineral Muscovite mica belongs to the group of phyllosilicates. It consists of potassium, aluminum, silicon, oxygen and hydrogen. The sum formula of the monoclinic crystal system reads as $KAl_2(AlSi_3O_{10})(OH)_2$. A sketch of the crystal structure is given in figure 3.1. The potassium atoms act as separator between layer of $\sim 9.94\,\text{Å}$ thickness. The interlayer bounding is very weak compared to the intralayer bounding. Consequently cleaving mica leads to a controlled break along one flat plane. The resulting surface appears to be atomically flat in the range of centimeters. Further, the freshly cleaved surface is free of any contaminants. This makes mica a well suited candidate for a substrate when the roughness has to be controlled on the atomic scale [42].

Cleaving mica leads to a surface which consists mostly of charged potassium atoms. Subsequently, the surface is hydrophilic and attracts water from the atmospheric humidity. Even when graphene is deposited onto mica under pure N_2 atmosphere water is able to diffuse into the interlayer when the sample exposed to air [43]. This happens within seconds. The water layers between graphene and mica occur either as thin (monolayer) film or as fractal structure depending on humidity and fabrication process. They can be visualized by AFM imaging. The existence of water molecules close to the graphene surface have to be taken into account when the interaction of graphene and substrate is discussed. Optically induced degeneration of graphene and substrate also induced effects on the water layer which will be discussed in chapter 4.2.2.

Mica is transparent in the visible which can be advantageous compared to silicon wavers that are often used. Due to the monoclinic crystal structure it is birefringent. The respective refractive indexes lie in the ranges of $n_\alpha = 1.552 \ldots 1.576$ and $n_\beta = 1.582 \ldots 1.615$ as well as $n_\gamma = 1.587 \ldots 1.618$ [44]. The resulting birefringence of $\delta = 0.035 \ldots 0.042$ can be used to obtain high contrast images of single graphene layers on mica as described in [45] and chapter 3.1.2.

Since mica forms centrosymmetric crystals electric dipole SHG is not expected from the bulk. In 2011, Savoia et al. [42] studied second harmonic generation from mica experimentally. Samples of different thickness were investigated in a transmission setup. The measured SHG should be independent of the sample thickness when only surface contribution to the SHG are taken into account. Quite contrary, a crucial thickness dependence was measured. Savoia et al. explained this theoretically by dominant nonlocal quadrupolar SHG from the bulk. Further polarization and sample orientation dependent measurements fit to the model. Rotating the sample by 360° along the transmission axis leads to six peaks in the SHG signal. This coincides with the sixfold symmetry of the crystal structure.

In summary, sheets of Muscovite mica appear as a suitable substrate with respect to surface roughness, sample fabrication and optical characterization possibilities. Nevertheless, the effects of water interlayers and its response in nonlinear optical experiments have to be taken into account.

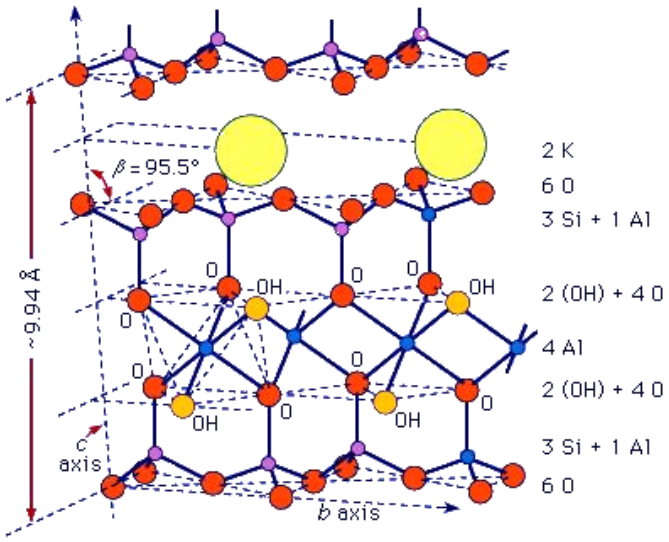

Figure 3.1: Crystal structure of Muscovite mica. Mechanical cleavage of mica results in an atomically flat surface along the potassium atom plane [46].

3.1.2 Sample Characterization by High Contrast Imaging

Due to the fabrication process of the samples graphene monolayer are relatively rare. Monolayers can be visualized in principle by atomic force microscopy but the scan speed is relatively low. Furthermore, the height information can be influenced by the substrate due to different interactions with the tip. The low optical absorption per layer and even lower reflectivity makes it difficult to detect the layer thickness using an optical microscope.

However, treating graphene as a thin Fabry-Pérot etalon, interference effects can be used for fast and easy high contrast imaging. Figure 3.2 (a) shows the scheme of a setup as published in [45] and used during this thesis. Graphene is illuminated through the mica substrate by linear polarized light from a halogen lamp. The birefringence of mica induces a rotation of the polarization. Since the coherence length of a halogen lamp ($\sim 1\,\mu$m) is larger than the graphene thickness, the reflected light from the mica-graphene interface interferes with the reflected light from the graphene-air interface. The reflected light passes mica again and the polarization is rotated a second time. Collected by the objective, the light passes a second polarizer which blocks all light reflected by the top of the mica. Thus, the following camera detects only the light reflected by the mica-graphene side. The contrast between graphene covered and uncovered mica regions within one image can be written in terms of the reflected intensities I:

$$C = \frac{I_{mica,bottom} - I_{graphene}}{I_{mica,bottom}} \cdot 100\,\%. \tag{3.1}$$

Assuming perpendicular incidence, one can express $I_{mica,bottom}$ in terms of the reflection coefficients $r_{mica,air}$. They are defined by the complex indexes of refraction n_{mica} and n_{air}.

$$I_{mica,bottom} = I_0 \cdot |r_{mica,air}|^2 = I_0 \cdot \left|\frac{n_{air} - n_{mica}}{n_{air} + n_{mica}}\right|^2 \tag{3.2}$$

I_0 is the incident intensity. The total light reflected from graphene can be derived from multiple reflections from both interfaces and multiple-beam interference. According to [45] one gets

$$I_{graphene} = I_0 \cdot \left| \frac{r_{mica,graphene} + r_{graphene,air} \exp\left(-4i\pi \frac{m \cdot d}{\lambda} n_{graphene}\right)}{1 + r_{mica,graphene}\, r_{graphene,air} \exp\left(-4i\pi \frac{m \cdot d}{\lambda} n_{graphene}\right)} \right|^2 \tag{3.3}$$

where $m \cdot d$ is the thickness of m layers of graphene and $d = 0.34$nm. The refractive index of graphene can be approximated by graphite's refractive index for a plain parallel light field to be $n_{graphene} \simeq 2.675 - 1.35i$ [47]. Figure 3.2 (b) shows $C(m)$ for different wavelengths λ. As one can see, even when a white light source is used one can distinguish between single layer numbers in the important low layer regime.

The calculation was based on perpendicular incidence onto a homogenous sheet. This approximation becomes inaccurate when an high NA objective is used or the graphene has a substructure below the resolution limit. Furthermore, when the substrate is only slightly birefringent or the polarizers are not well aligned, one also has to consider the reflection from the top of the substrate. The result is a continuum of possible contrasts. The measured value lies between a minimum and maximum contrast C_{min} and C_{max}. Assuming the substrate to be highly transparent, the incident intensity is equal for top and bottom reflection, i.e. $I_0 \simeq$ const., and one derives [32]

$$C_{max} = \frac{I_{substrate,bottom} - I_{graphene}}{I_{substrate,bottom}} \cdot 100\%, \tag{3.4}$$

$$\begin{aligned} C_{min} &= \frac{I_{substrate,bottom} - I_{graphene}}{I_{substrate,bottom} + I_{substrate,top}} \cdot 100\% \\ &\simeq \frac{I_{substrate,bottom} - I_{graphene}}{2 \cdot I_{substrate,bottom}} \cdot 100\% = \frac{1}{2} C_{max}. \end{aligned} \tag{3.5}$$

Unfortunately, the distinctness is lost, especially when all uncertainties are taken into account. Nevertheless, this method was always used for a first characterization of the sample because it is easy and fast. A more sophisticated, but more complex characterization with respect to mono- or fewlayer graphene is given in the following chapter.

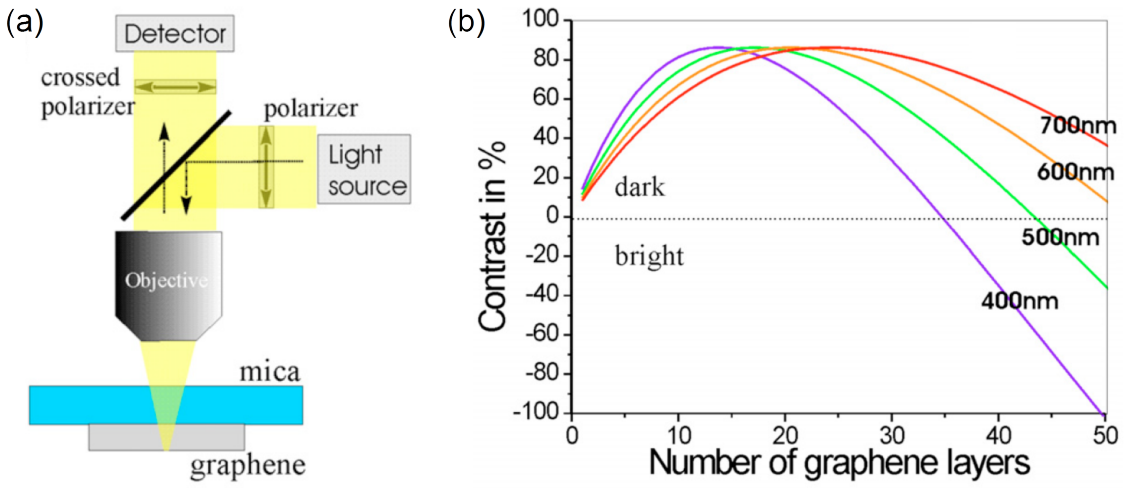

Figure 3.2: (a) Scheme of the high contrast imaging setup used to characterize graphene on mica samples. (b) The layer contrast calculated from the ansatz of interference in a Fabry-Pérot etalon. Even white light can be used to identify monolayer graphene [45].

3.1.3 Sample Characterization by Raman Spectroscopy

Another nondestructive and fast method to detect monolayer graphene and distinguish them from double and few layer graphene and graphite is Raman spectroscopy [48]. Due to the peculiar π-electron dispersion of graphene, Raman spectroscopy is always resonant. Consequently Raman peaks are relatively strong and easy to detect. A couple of distinct peaks appear at wavenumbers between 1000 and 3000 cm^{-1}. Their position is defined by specific vibrations within the layered carbon structure. Slight shifts, changes in shape and intensity can be observed depending on the number of layers, doping level and impurity density. Figure 3.3 (a) shows the Raman spectrum of graphite and a monolayer graphene. The G and 2D peaks are dominant. The intensity of the 2D peak is clearly enhanced for graphene. Figure 3.3 (b) shows the evolution of the shape of the 2D peak when graphite is downsized from bulk, to 10 and 5 layers and further down 2 and 1 layer of graphene. There are clear differences in the few layer regime according to the phonon spectrum.

The 2D peak is the second order of the D peak. When an electron-hole pair is created, electron-phonon scattering can lead to an intervalley transition of the electron, i.e. a jump from the cone at the K-point to this at K' (compare figure 2.5 on page 12). Recombination is only possible when the electron is scattered back into the first cone. This can happen either by impurity scattering or again by electron-phonon scattering. In contrast to the impurity, the second phonon gain again an amount of energy. These processes lead to the D-peaks which depends on the density of impurities on one hand. On the other hand, the 2D peak at twice the energy arises.

Moreover, the mentioned double phonon scattering changes slightly in bilayer graphene. The interaction of the two planes cause the π and π'-bands to divide in four bands with a different splitting for electron and holes. In short, this leads to four different processes involving phonons with four different wave vectors. Finally, the 2D peak for bilayer graphene consists of four contributions of slightly different wave number. The result is a significant broader peak compared to monolayer

graphene [48].

In summary, Raman spectroscopy provides a powerful tool for the characterization of graphene samples. Especially the properties of the 2D peak itself and in comparison with the G peak is a very good addition to the above mentioned high contrast imaging. Both methods together fit perfectly to the purposes and were used during this thesis.

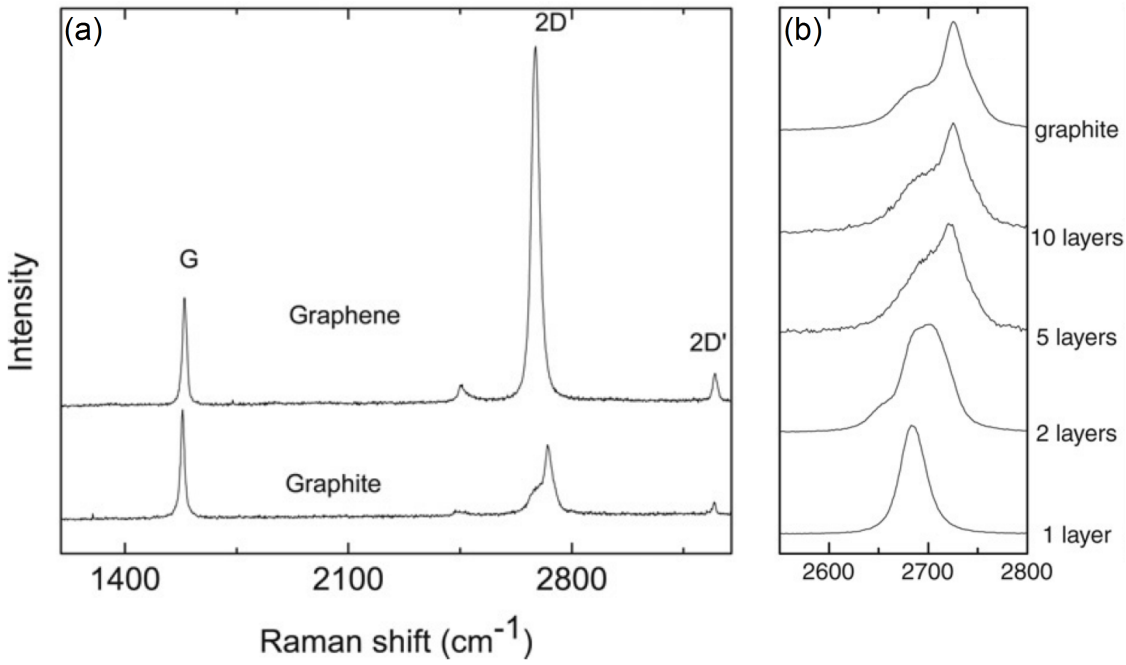

Figure 3.3: (a) Typical Raman spectra from bulk graphite and a monolayer of graphene. The size of the 2D peak is clearly different for graphene and graphite compared to the G peak. (b) The evolution of the shape of the 2D peak from graphite to monolayer graphene is obvious. This allows to distinguish clearly even between fewlayer, bilayer and monolayer graphene. Both images show the case for 514 nm incident wavelength [48].

3.2 The Confocal Scanning and Spectroscopy Setup

3.2.1 Overview and Development

The upconversion setup is based on a confocal scanning setup for fluorescent studies in the visible spectral range. During the time of this thesis it was established for upconversion investigations using both, confocal scanning and spectral analysis. A sketch is given in figure 3.4. For excitation a Ti:Sa laser was used. Its emission wavelength is tunable in a range of roughly ± 50 nm around 970 nm. In the pulsed state it is emitting < 100 fs short pulses (see chapter 3.2.2 for details). The pulsed emission can be efficiently frequency doubled by inserting a BBO crystal. Afterwards, the beam is guided through a continuously variable neutral density filter, a telescope and a iris diaphragm to control power, angular spread and beam width, respectively. After passing the beamsplitter it is focused by a Leitz Wetzlar $50x$

magnification, $NA = 0.6$ microscope air objective onto the sample. The sample lies on the 2D scanning stage of the NT-MDT atomic-force microscopy system. The Software NOVA Px is used to control the position of the sample and the distance of the objective. The emitted light from the sample is collected by the same objective, passing the beamsplitter again and the shortpass filter FF01-842/SP. The filter edge wavelength lies at 835 nm and the first stop band is centered around 842 nm. The following lens, the 50 μm pinhole and the second lens realize the confocal principle. The pinhole can be flipped out for non-confocal analysis. A flip mirror is used to switch between a path to an avalanche photo diode or to a spectrometer, respectively. The confocal principle and the optical detection instruments will be explained in chapter 3.2.3 and 3.2.4, respectively.

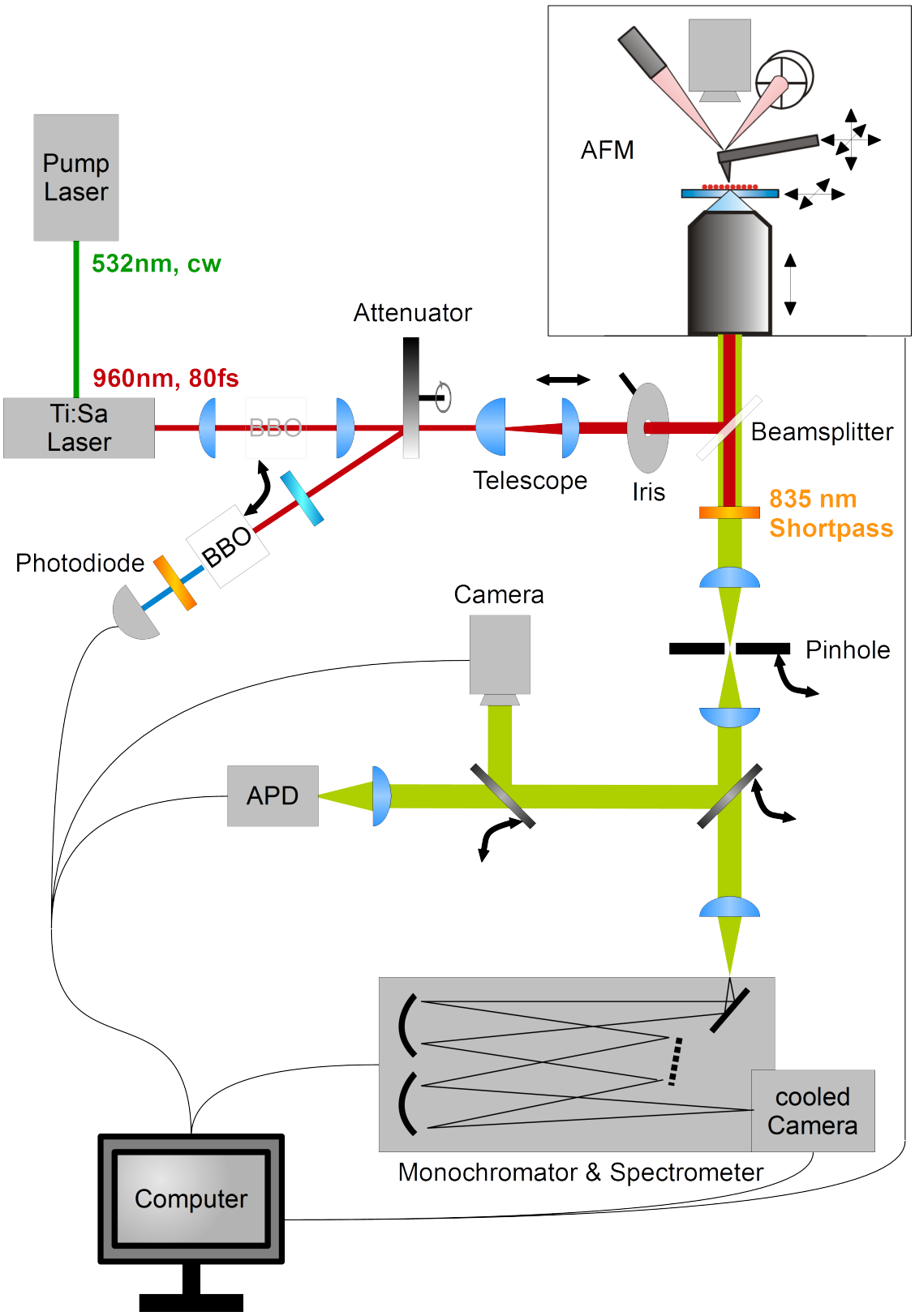

Figure 3.4: Sketch of the upconversion confocal scanning setup. The sample is mounted on the AFM scanning stage and is optically accessible from below. The sample is excited by focused $\sim 80\,\mathrm{fs}$ pulsed laser light from a Ti:Sa laser. The laser light can be frequency doubled using a BBO crystal. Otherwise the BBO acts as a control unit to indicate the pulsed state. In the detection path only light of shorter wavelength than 835 nm is transmitted through the shortpass filter. Either a camera, an APD or a spectrometer are provided. For spectrometry, the pinhole was flipped out of the beampath.

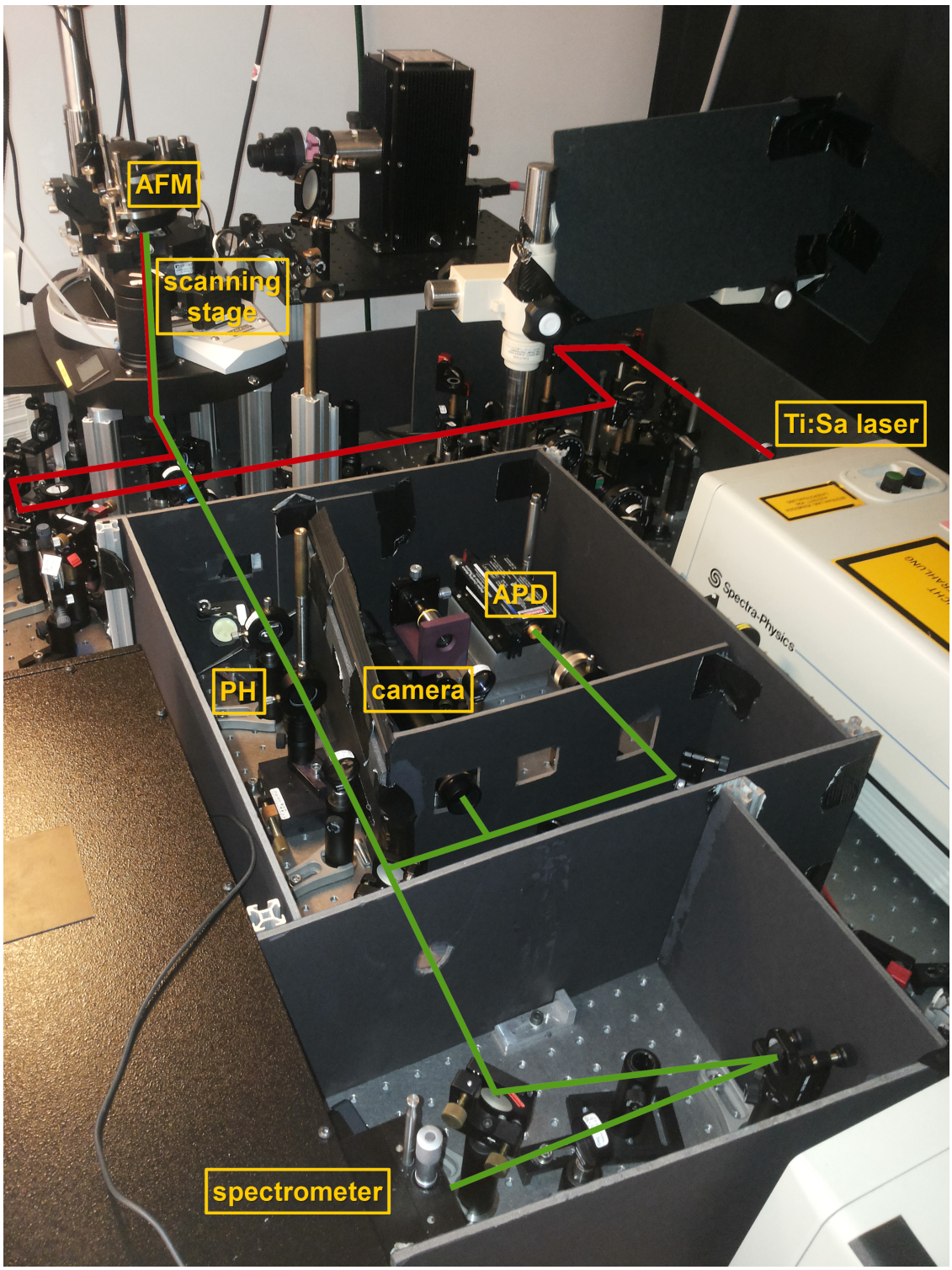

Figure 3.5: Photo of the real setup, uncovered for illustration. The red line indicates the excitation light path starting at the Ti:Sa laser and ending at the sample on top of the scanning stage. The emission light path, indicated by the green line, goes from the sample through the pinhole (PH) and can either be guided to the avalanche photodiode (APD), to the camera or to the spectrometer. The atomic force microscope (AFM) is also an essential part of the setup but was not used within this thesis.

For analyzing the very broad spectral range emitted by the sample, one has to take care about the transmission characteristics of all optical components, especially mirrors and lenses. Aluminum and Silver mirrors show an acceptable wavelength dependent reflectivity. Furthermore, lenses with different anti-reflection coatings are available. Typical anti-reflection coatings are designed for either 350...700 nm or 650...1050 nm. Both coatings cover the considered spectral range only partly. Finally, chromatic aberration appears at the focusing elements. To reduce this effect, all spectral measurements were performed without pinhole.

To characterize the transmission of the setup, the path from the objective to the last mirror in front of the spectrometer was inspected with a thermal light source. Figure 3.6 (a) shows the transmission function of the spectrometer path in arbitrary units. In addition, the transmission of the shortpass and the transmission of the collection lens in front of the spectrometer are given according to manufacturer's data (Figure 3.6 (b) and (c)) .

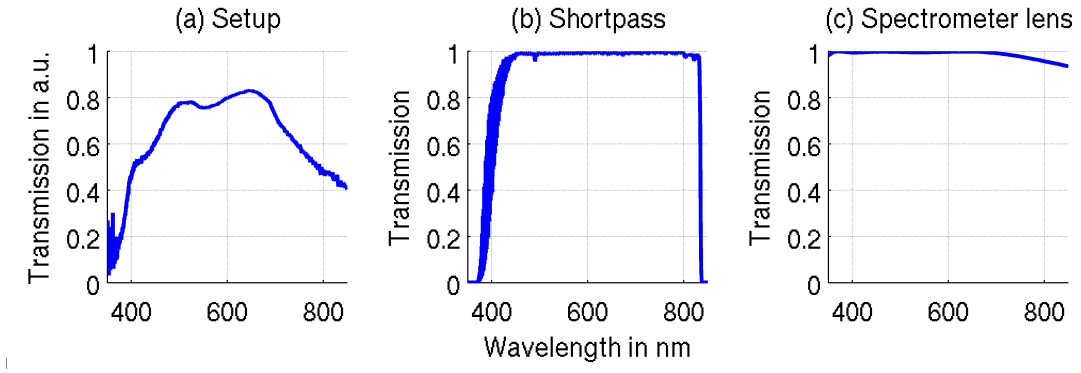

Figure 3.6: (a) The measured spectral transmission function of the detection path of the setup. (b) The transmission of the shortpass filter. (c) The transmission of the spectrometer collection lens. (b) and (c) are based on manufacturer's data.

3.2.2 The Excitation Light Source: Mode-locked Ti:Sa Laser

The investigation of higher order optical effects requires high intensity light sources. The best opportunity is to use a pulsed laser where the energy of one repetition cycle is compressed and emitted into one pulse of significant shorter time. Within this work the Spectra-Physics Tsunami laser was used, pumped optically by a Verdi V18 solid state cw laser. The active medium, Titanium doped sapphire, covers a broad spectral range. The system enables to generate laser pulses of about 80 fs pulse length at 80 MHz repetition rate. The wavelength was tunable in a range of roughly 920 to 1020 nm. For active modelocking an acousto-optic modulator is installed. The laser can be switched between continuous wave and pulsed mode.

Due to the absorption of atmospheric oxygen, water vapor and water films on surfaces at the emissions wavelength the Tsunami appeared to be very sensitive to the environment. Especially at the beginning of this work, fluctuation of the average emission power and beam direction as well as spontaneous switching from pulsed to cw mode occurred. Precise alignment and constant flushing with nitrogen starting at least one day before use was necessary.

The laser's state was monitored using the back reflection of the attenuator wheel.

By guiding the light through a longpass, a BBO crystal and a shortpass onto a photodiode, control of power and state of the laser was provided during measurements.

3.2.3 The Confocal Principle

The combination of a high-NA objective and an avalanche photodiode allows the detection of very weak light sources. The resolution is mostly determined by the numerical aperture of the objective. A high resolution improves the quality of scans. Furthermore, it is necessary to detect the light from the focused plane, exclusively. This increase of longitudinal resolution and background suppression is realized by a confocal microscope setup.

Behind the shortpass filter, the detection light path consists of an arrangement of a first lens, a 50 μm pinhole and a second lens. The pinhole is positioned in the focal point of both lenses. Light collected by the objective is focused on the pinhole. An sharp image occurs only for the emitters in the objective focal plane. Since only the center of the image can pass the pinhole, most of the information of other light sources are suppressed. The second lens collimates the beam for the following detection path. This technique increases the longitudinal resolution and allows measurement even under dimmed overhead light conditions [49].

For this thesis, all presented scans were performed using the setup as a confocal microscope. The pinhole was flipped out during spectrum acquisitions. This should avoid cut-off effects at the pinhole due to chromatic aberration and therefore misleading spectra. Indeed, background subtraction post-processing becomes unavoidable.

3.2.4 Optical Detection Instruments

Using the setup as a confocal microscope allows the operation of a sensitive avalanche photodiode (APD). Avalanche, in this sense, means the multiplication of charge carriers after one photon is absorbed producing one electron-hole pair. Most simply, an ideal APD would be a good PIN photodiode with gain [50]. The sensitivity of the APD is limited by the detector noise limit, the photon shot noise and the APDs leakage current. Here, the Perkin Elmer SPCM-AQRH Single Photon Counting Module was used. The single photon timing resolution of 350 ps fits with the Tsunami laser's repetition rate of 80 MHz = $(12500\,\mathrm{ps})^{-1}$. More important for this work is the spectral photon detection efficiency as plotted in figure 3.7 (c). The used APD fulfill the requirements of high detection efficiency over the range of 400 to 850 nm. Anyway, the detection efficiency is not constant over the whole range which has to take into account when spectral different measurements are compared.

When the scan shows an region of special interest, the sample can be moved piezo controlled to this position, the pinhole and one mirror can be flipped out and spectral acquisition is possible. The light is guided into the Acton SP2500i monochromator/spectrometer. Via two concave mirrors and one grating the light is split in its spectral components. One can choose between two gratings with either 1200 grooves per mm or 300 grooves per mm. A higher groove density is appropriate for a high resolution. In contrast, the light is split into a wider angle and therefore less photons reach the detector. Consequently, for measurements with poor signal-to-noise ratios, a grating with less grooves is more suitable. Furthermore, the gratings are blazed at 500 nm. This is an optimization to scatter an high amount

of the light into the first diffraction order. Both properties together define the grating efficiency, shown in figure 3.7 (a). For broad spectra, the grating efficiency has to be taken into account as a weighting function. Finally the detection is done by the Andor Newton CCD camera. The 27.6×6.9 mm image area contains 1024×255 pixels. The typical operation temperature of -70°C lowers the noise. The quantum efficiency (figure 3.7 (b)) of the camera is extracted from the data sheet and acts also as a weighting function.

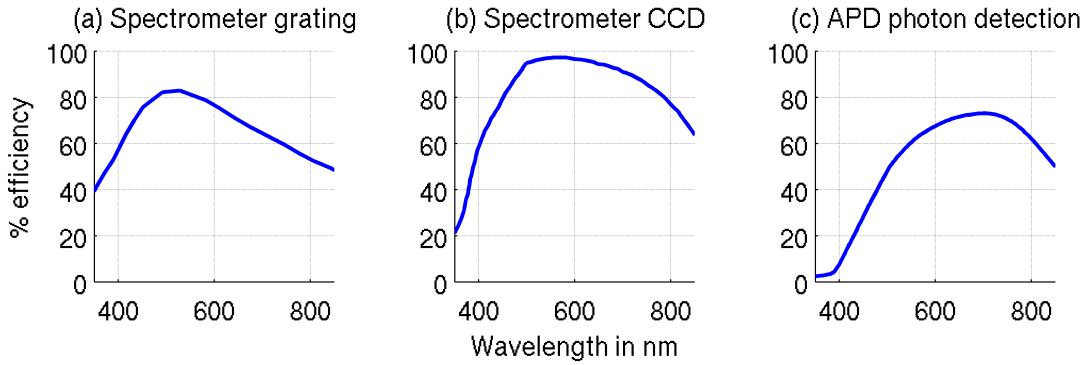

Figure 3.7: (a) Spectrometer grating efficiency. (b) Quantum efficiency of the attached CCD camera. The non-uniformity must not be neglected when broad spectra are analyzed. (c) The quantum efficiency of the APD must be considered when the spectrum of the emission changes.

All influences, i.e. the detection path transmission, the shortpass filter transmission, spectrometer collector lens transmission, the grating efficiency and the CCD quantum efficiency, have to be taken into account for quantitative reliable spectral statements. The product of all individual functions form the total weighting function (figure 3.8). As one see especially in the ranges below 500 nm and above 650 nm post-processing of the data is necessary.

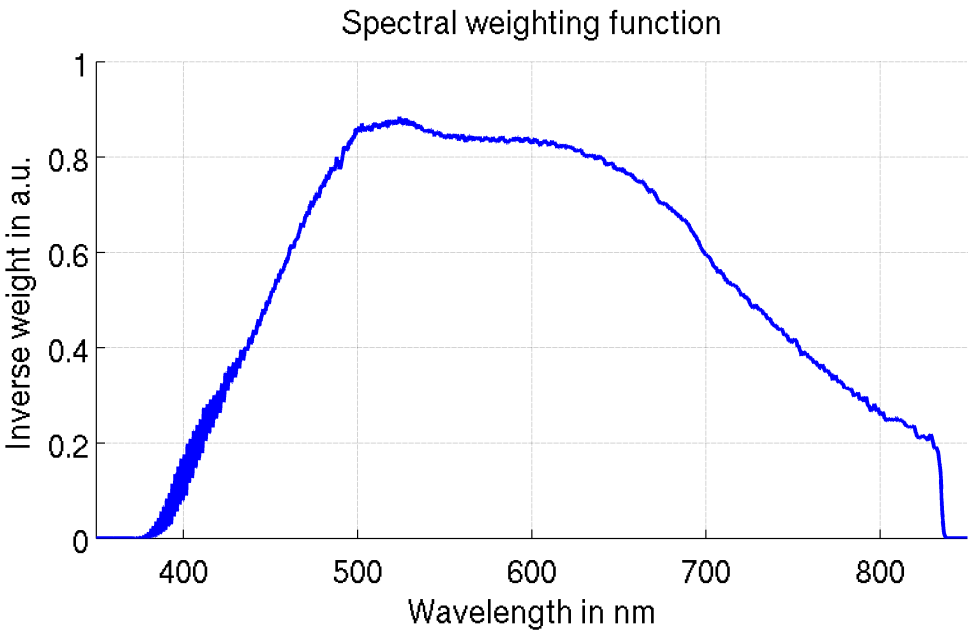

Figure 3.8: Overall detection efficiency for the upconversion luminescence setup with the spectrometer in use. This function is obtained from multiplication of all former mentioned weighting functions.

3.3 Atomic-Force Microscopy

For the investigation of spatial structures smaller than the wavelength of visible light, atomic force microscopy was used. In short, the surface of the sample interacts with a tiny tip at the front of a silicon cantilever. The cantilever is moved piezo controlled along the surface while a laser is reflected by the cantilever on a diode array. When the cantilever is bended due to the interaction with the surface, a change in the illumination of the diode array occurs. This position dependent information can be stored. Several different techniques exist how to scan the surface.

A very useful tool for atomic force microscopy is the "tapping mode". The tip is driven by a generator close to its resonance frequency somewhere between 1 and 100kHz depending on the cantilever, e.g. its material and length. When the tip is scanned along the surface, a change in topography changes the amplitude of the tip. A feedback mechanism moves the tip closer to or further away from the surface until the previous amplitude is recovered. This method generates a high-resolution topography. Simultaneously, the tip is not in direct contact with the surface. This avoids the issue of lateral forces and drag across the surface.

The setup contains an AFM on top of the sample holder. The ability to image a monolayer with this AFM is proofed in [32]. However, to achieve even higher resolution the AFM of the group of Prof. Rabe was used during this thesis as this setup is even better stabilized against vibrations.

4 Results

This chapter presents the data and the results accumulated during this thesis. The first section demonstrates the characterization of samples of graphene on mica and the confocal imaging using femtosecond pulsed laser excitation. The process leading to the luminescence is firstly studied by spectral filtering and excitation power dependent imaging. Furthermore, degeneration of graphene under intense irradiation is briefly investigated. The results allowed the development of acquisition methods to obtain spectral information of the upconversion luminescence of graphene. As introduced in the theory chapter, the luminescence will be explained and classified in coherent and incoherent upconversion processes.

4.1 Imaging with Femtosecond Pulsed Laser Excitation

4.1.1 Confocal Scanning

The following section presents the obtained results from scanning and imaging of graphene on mica. The sample was fabricated by Nikolai Severin (group of Prof. Rabe, department of physics, Humboldt-Universität zu Berlin) by mechanical exfoliation from a highly orientated pyrolytic graphite crystal (grade ZYB). Prepared in a glove box, it was stored under ambient conditions for the whole time. As described in chapter 3.1.1, one can assume a water layer between mica and graphene, either as homogenous layer or as fractal structure. The sample was in use for approximately one month. Thus, other contamination is not expected to appear.

Shortly after fabrication, the sample was characterized by high contrast imaging. Several low layer graphene flakes were found and some of them were expected to be monolayer graphene. Figure 4.1 shows a location where multilayer graphene flakes step down. The red rectangles mark the regions where flakes with a significant low contrast were found. The contrasts lie below the expected values derived in chapter 3.2. This can be explained by limited resolution of the microscope and by slight misalignment of the setup. However, the five marked areas F1-F5 were further analyzed by Raman spectroscopy. The insets (b) to (d) show the view on the sample through the Raman setup for flake F3, F4 and F5. Laser light of 532nm wavelength was focused in the center of the small squares

Figure 4.2 present the D, G and 2D peak regions of the obtained Raman spectra. The flakes F1 to F5 can be clearly classified. In contrast to flake F2 and F5 which show the typical behavior of double or fewlayer graphene, flake F1, F3 and F4 are concluded to be monolayer graphene. The 2D peak close to $2700\,\mathrm{cm}^{-1}$ is clearly shifted, narrower and enhanced compared to the G-peak. The G-Peak at $1580\,\mathrm{cm}^{-1}$ remains unchanged for all cases. This matches with the monolayer characteristics described in chapter 3.1.3. Furthermore, the spectrum in the range of a possible D-peak at $1350\,\mathrm{cm}^{-1}$ is given. From the absence of this peak, it follows

that no impurity or boundary scattering is involved in these Raman processes. Consequently, all inspected positions are part of large and high quality graphene crystals.

Finally, the dashed line in figure 4.1 marks the region which was scanned afterwards using the upconversion confocal scanning setup. The results will be given hereafter. The work of sample fabrication and characterization was completely done in the laboratories of the group of Prof. Rabe.

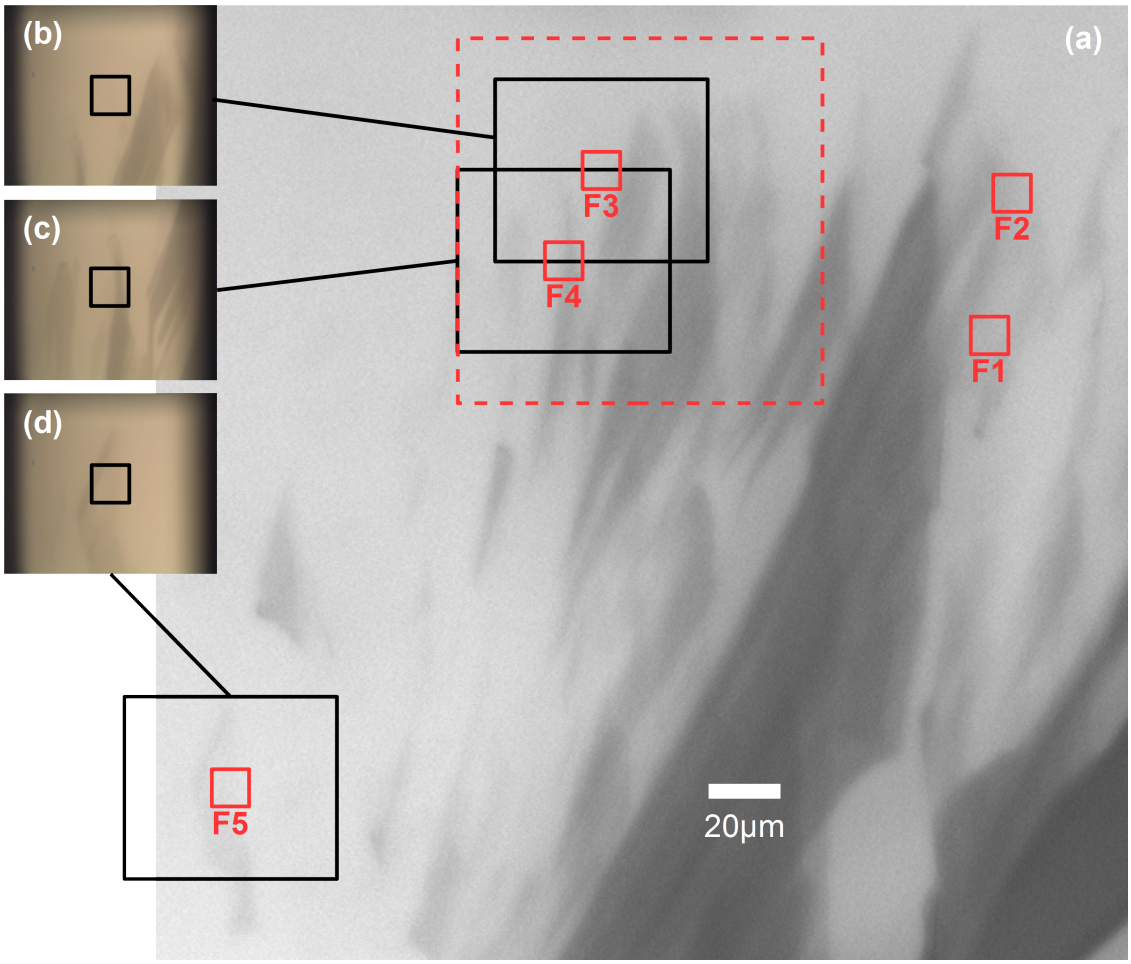

Figure 4.1: (a) High contrast image of graphene on mica. The layered structure of the multi- and fewlayer graphene is clearly visible. The small red squares indicate flakes suspected to be monolayer. They are labeled with letters F1-F5. (b) - (d) Images produced by the Raman setup. The center of each square is probed by Raman spectroscopy. The dashed line indicate the later upconversion confocal scanning area.

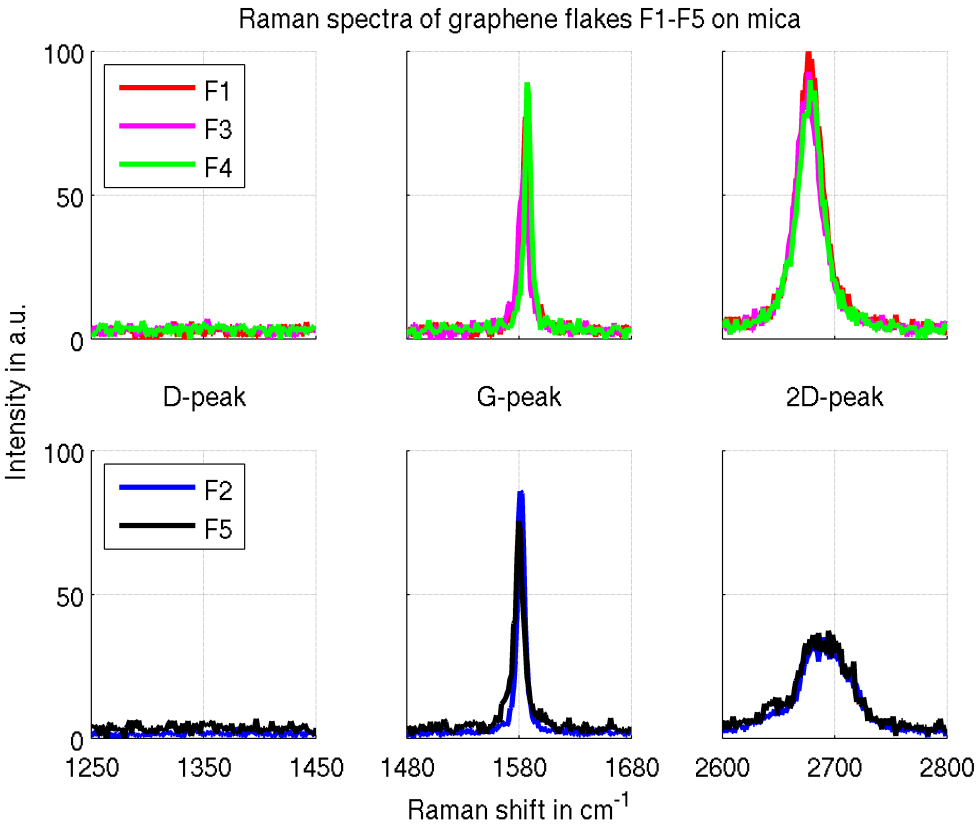

Figure 4.2: Raman spectra from the graphene flakes F1-F5. The selections are centered around the (potential) D-, G- and 2D-peak, respectively. Flake F1, F3 and F4 are determined to be monolayer due to the shape and enhancement of the 2D-peak. A missing D-peak at 1350 cm^{-1} indicate extensive high quality graphene around the laser focus.

As mentioned before, the sample was well characterized for further investigations. It was mounted upside-down on the confocal scanning setup. Cameras above the sample and in the detection path were used to find the correct position. The Tsunami laser was well stabilized and constantly set to a wavelength of 960 nm. The average excitation power $P_{avg} = 5.6\,\mathrm{mW}$ was measured in front of the last mirror prior to the microscope objective (see figure 3.4 and photo 3.5 on page 34f). Loss of 10 % for both the mirror and the objective and full use of the entrance aperture can be assumed. The fluence at the sample can be estimated from the average power P_{avg}, the repetition rate $f_{rep} = 80$ MHz, the focus area $A_{foc} = \pi w_0^2 = \lambda^2/(\pi \cdot NA)$ and a correction factor of $\eta \approx 0.9$ because of the losses:

$$\text{fluence} = \frac{\pi \cdot \eta \cdot P_{avg} \cdot NA}{f_{rep} \cdot \lambda^2} \approx 13000\,\mu\mathrm{J/cm}^2. \tag{4.1}$$

This value is high compared to the range of $0.1 \ldots 200\,\mu\mathrm{J/cm}^2$ in the cited papers [1, 39] in chapter 2.3.5. The upconversion luminescence confocal scanning image is presented in figure 4.3 as false color image. One can clearly identify the layered structure of thin and thick graphene flakes. Moreover, the monolayer graphene appears much brighter than the background. Beside background noise, speckles in the signal are caused by intensity fluctuations of the excitation laser. The resolution is limited by the diffraction limit and imperfections in the alignment. However, imaging of graphene on mica is successfully demonstrated.

Upconversion confocal scanning turns out to be a very efficient and high contrast imaging technique for graphene, from multilayer down to monolayer. The spectral very broad luminescence of graphene allows the efficient detection even for high scan speeds and low excitation power. However, neither in figure 4.3, nor in any other similar scan, spatial resonance features e.g. on edges appeared. They were expected by analogy to gold nanocrystals as described in chapter 2.3.4. To exclude misleading effects because of the spectral integration, the following chapter will present a spectrally filtered scan of the same region.

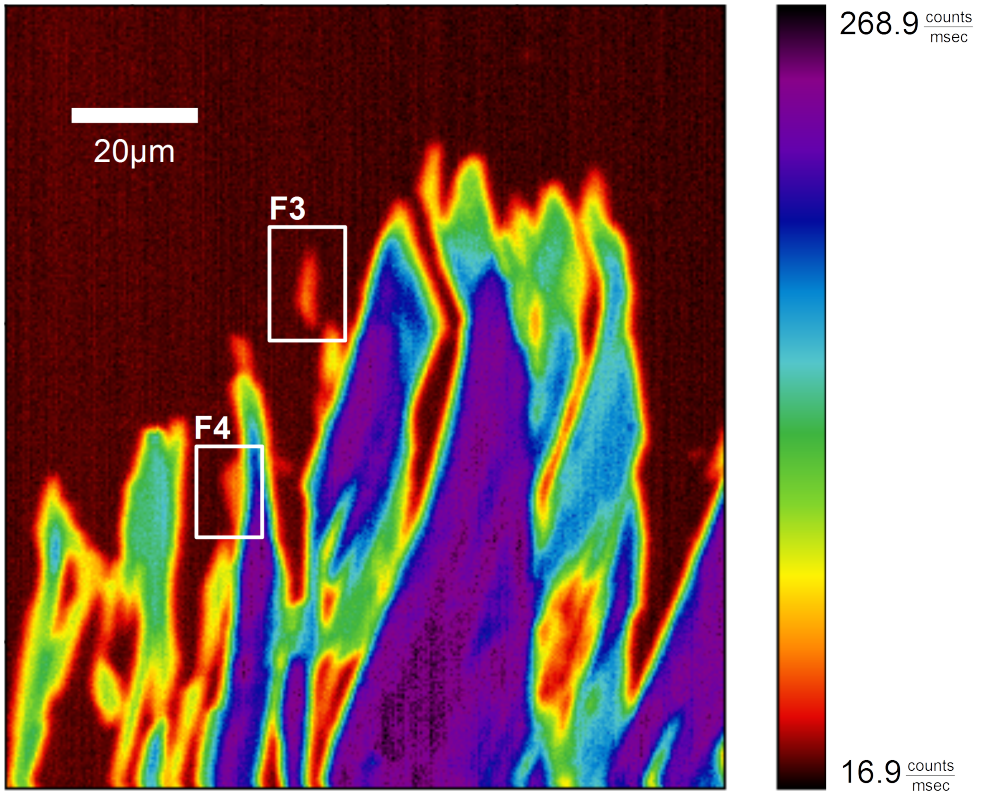

Figure 4.3: False color image of the upconversion luminescent graphene. The region belongs to the red rectangle in figure 4.1. The monolayer F3 and F4 which were characterized by Raman spectroscopy are marked with white rectangles. The layer contrast as well as the bright luminescence even of monolayer graphene is obvious.

4.1.2 Spectrally Filtered Confocal Scan

In the previous chapter, upconversion confocal scanning turns out to be a very efficient tool for imaging graphene. As will be shown later in chapter 4.3 one reason for the efficiency was the spectral broad luminescence of graphene which was easily detected without spectral selection. If resonances similar to those in gold nanocrystals (chapter 2.3.4) would exist, they would appear as specific spatial features in the radiation of light of specific wavelength. The integration over a broad spectral range would therefore overlap all these features. The result would be a more or less homogenous image of the luminescent graphene.

A bandpass was placed in front of the detector for spectral selection (compare figure 3.4 on page 34). The bandpass FB590/10 is transparent around (590 ± 2) nm. The FWHM of (10 ± 2) nm allows the detection of a small fraction of emitted

radiation. The suppression of a majority of the light required adjustment in the scanning parameters. The excitation power was set to 18.2 mW (more than three times higher than before) and the APD acquisition time and scan speed was set to 100 msec per point (10 times slower then before). The result is an image of satisfactory signal-to-noise ratio (figure 4.4). The image shows a subsection of the scan in the previous chapter rotated by 45°. The monolayer F3 is marked with a white rectangle.

Even for a spectral section of only 10 nm around 590 nm, no distinctive spatial features appear. The image is qualitative identical with the previous scan where no bandpass was used. To conclude, the observation of resonances similar to the measurements on the gold nanoprisms [36] failed. If these resonances are not present by principle, if the effects are too weak compared to the homogenous luminescence or if just the spatial resolution is to low will be discussed in chapter 5. Consequently, the following chapters will focus on the present luminescence to understand the physical process of upconversion.

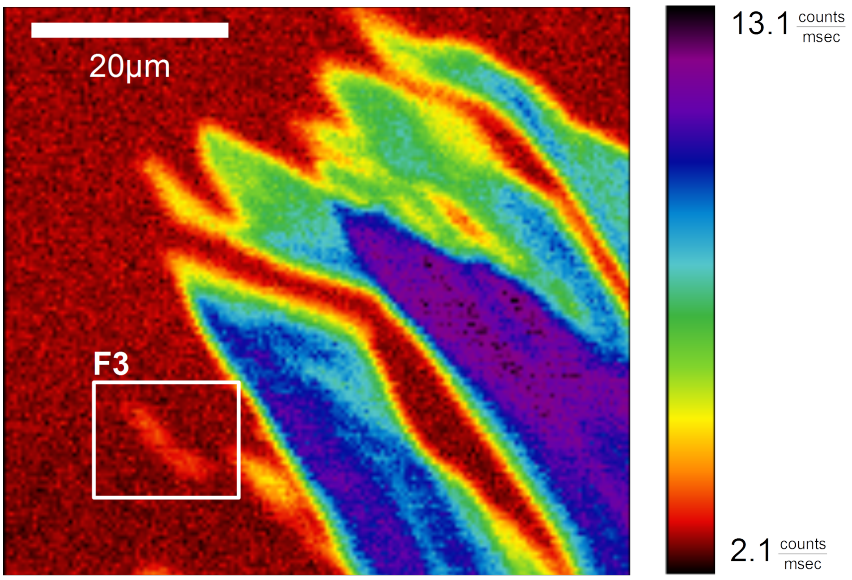

Figure 4.4: Spectral filtered upconversion confocal scan of a subsection of the previous region. The white rectangle marks the monolayer F3. The 10 nm wide bandpass around 590 nm required a 10 times lower scan speed and increased excitation by a factor of more than 3. No distinctive spatial features appear.

4.1.3 Intensity Dependence

It is inevitable for the understanding of the nonlinear optical response to study the excitation intensity dependence. As mentioned in chapter 11, two possible processes in graphene can lead to upconversion: one-photon absorption and efficient scattering in contrast to two-photon absorption. The following data present the range of the luminescence between what can be detected and below the destruction threshold for graphene. The excitation power is tuned between 0.66 and 18.2 mW. These values correspond to a fluence of 1500 μJ/cm^2 and 42000 μJ/cm^2, respectively. As shown in figure 4.5 the lower value corresponds to an excitation where only thick layered graphene is apparent. Above a power of about 18.2 mW destruction of graphene occurs. (see chapter 4.2). Therefore it was avoided.

While the thick graphene multilayer is visible from the first image on, the graphene monolayers F3 and F4 become apparent at excitation power ~ 2 mW (image 3 to 4). From this image on, the layered structure is clearly visible for every excitation power. Bleaching and saturation is not observed within the shown range. For low power, the background is dominated by the dark count rate of the detector. For higher power, a small signal from the mica arises.

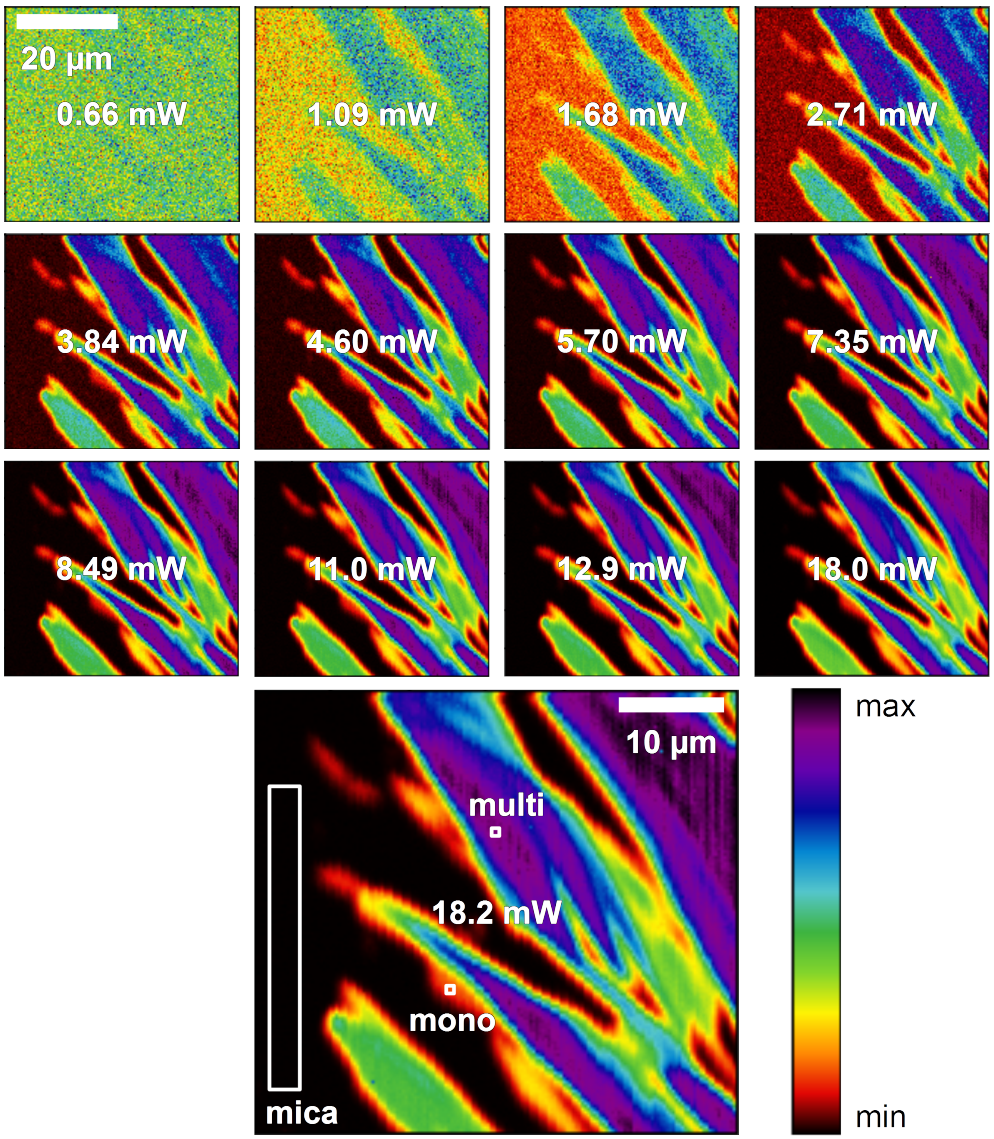

Figure 4.5: The excitation power dependence of upconversion confocal scans. The number in the center of each image gives the excitation power in mW. The white rectangles in the larger image show the region from which the data for a thick graphene multilayer, the monolayer F4 and the mica substrate is extracted and plotted in figure 4.6.

The APD count rate is extracted from the scans. The APD count rate for the mica background, the monolayer F4 and the multilayer is averaged over rectangular regions. They are exemplary shown in the image of 18.2 mW excitation power in figure 4.5. The unprocessed APD signal vs. excitation power is plotted in figure 4.6. The double logarithmic plot allows to determine the functional behavior at higher excitation power. For a second order optical process one expects the APD

count rate I_{APD} to scale quadratic with excitation power P_{exc}, i.e. $I_{APD} \propto {P_{exc}}^2$. The logarithm of the mica as well as the multilayer and monolayer signal were fitted to determine the slope using the model

$$\lg(I_{APD}) = a \cdot \lg(P_{exc}) + b. \tag{4.2}$$

The constant a determines the order of the optical process:

$$I_{APD} \propto {P_{exc}}^a \tag{4.3}$$

Both, multilayer and monolayer graphene, show the same functional behavior. Both signals have a slope of bit more than 2. This proofs an effect which is dominated by a second-order optical process in graphene and probably assisted by an higher order optical process. Due to the similar behavior, the physical reason is supposed to be the same. This is surprising with regard to explanations which focus on efficient scattering in the linear electronic bands of graphene [1, 39]. This is in contrast to the curved valence and conduction band in graphite where efficient scattering is not expected.

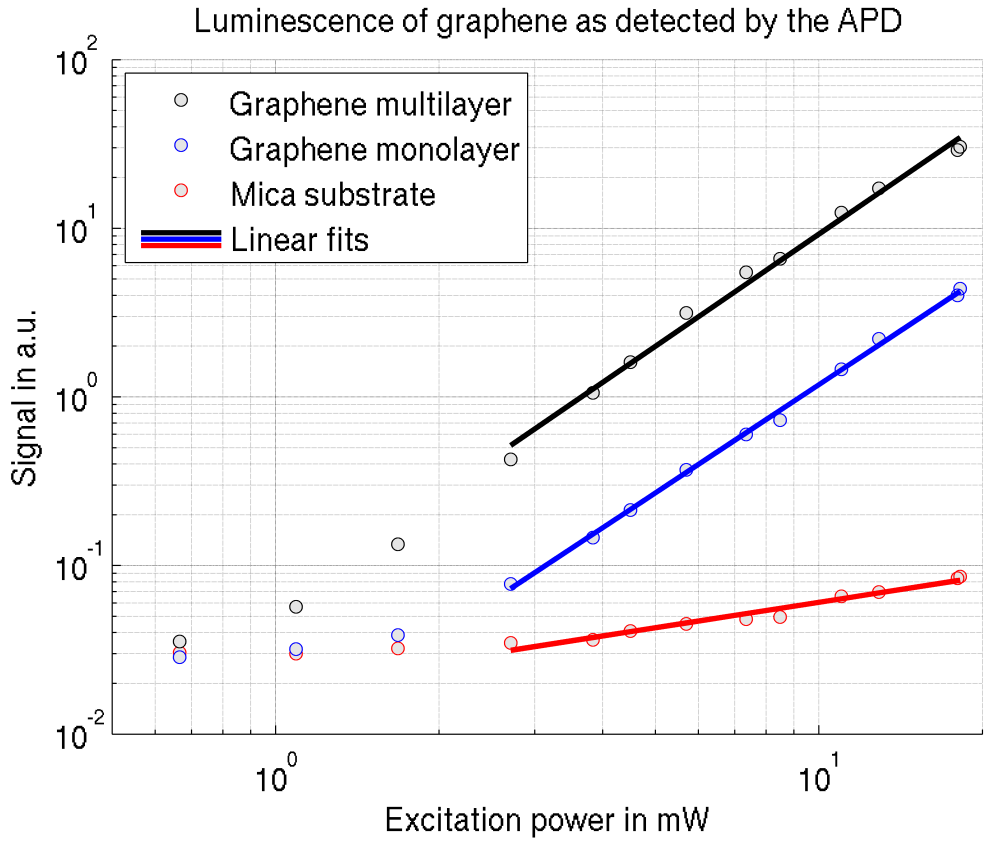

Figure 4.6: Excitation power dependence of the upconversion luminescence of graphene. The APD signal is extracted from confocal scans and plotted in a double logarithmic plot for a graphene multilayer, a monolayer and the mica substrate. The fits give a slope of about 2 which indicates a dominant second order nonlinear optical process for both multi- and monolayer graphene. For the fit parameters see table 4.1.

graphene multilayer	$a = 2.208 \pm 0.033$	$b = -1.244 \pm 0.031$
graphene monolayer	$a = 2.131 \pm 0.033$	$b = -2.060 \pm 0.031$
mica substrate	$a = 0.502 \pm 0.033$	$b = -1.720 \pm 0.031$

Table 4.1: Fit parameters obtained from linear fits in figure 4.6. The slope of about $a \approx 2$ indicates a dominant second order nonlinear optical process.

Finally these data emphasize that upconversion scanning is well suited for imaging graphene down to a monolayer. In chapter 3.1.2, a former high contrast method for imaging graphene was presented. Using this method, according to formula 3.5, a contrast of 11.08 % relying on interference is expected for a monolayer on mica when a light source of 550 nm wavelength is used. In contrast, the contrast calculated from the upconversion luminescence presented in figure 4.6 exceeds this value by magnitudes. The result is shown in figure 4.7. The contrast for the graphene monolayer is increasing with the excitation power. At 18.2 mW the monolayer appeared with a contrast of 5000 %.

The excitation power and therefore the contrast is only limited by the destruction threshold. This will be the topic of the next chapter.

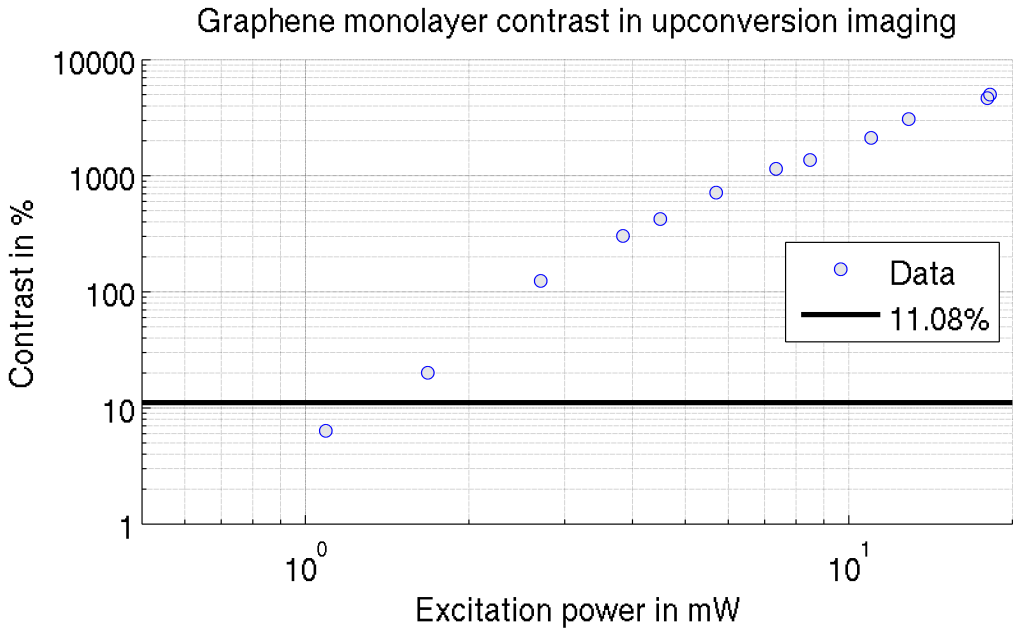

Figure 4.7: Intensity dependent graphene monolayer contrast. The contrast is calculated from the monolayer and mica data presented in figure 4.6 and emphasizes the ability to image graphene using upconversion. The black line corresponds to the value expected from high contrast imaging via interference for graphene on mica at 500 nm illumination wavelength.

4.2 Excitation close to the Destruction Threshold

4.2.1 Upconversion Bleaching and Bleaching Protection

As mentioned before, graphene can be easily damaged through intense laser irradiation. For the first time this happened accidentally when the laser stopped at a certain position between two confocal scans. It became obvious that this effect occurs when the pulse energy is dumped continuously into the graphene resulting in layer heating.

This is not an issue for scanning and imaging, but for spectroscopic purposes it is. The confocal scans are performed by using a sensitive APD and integrating over the whole spectral range. This allows a fast scanning speed. For spectroscopy, on has to encounter some technological obstacles. First, the detection is done by a cooled CCD camera. Indeed, the camera is very sensitive but not as powerful as the APD. Furthermore, the spectrally broad signal is splitted into several components, according to the wavelength. Every pixel of the CCD camera detects only a tiny fraction of the whole signal. This is in contrast to single emitter spectroscopy where the whole signal consists only of a few wavelength components. Conclusively, the spectrometer and the CCD camera is the combination of fragmentation of the signal and higher signal-to-noise levels for each fragment. The remedy is a long integration time on the order of $\sim$ 1min and high excitation power. Due to destruction issues, this is clearly not possible for a single spot. One solution lies in a periodic movement of the sample through the laser focus. The challenge is to both maintain spatial resolution and avoid destruction. The present chapter presents the acquired experience and shines some light on the physical effects which occur during the destruction. In the following the term "degeneration" will be used. This will become clear within the next chapter.

Figure 4.8 (a) shows the high contrast image of one of the first graphene samples investigated here. Several fewlayer graphene sheets are clearly visible, as extended sheets or as smaller structures like dots and lines. The encircled region shows a large homogeneous area of contrast of 9.5 %, i.e. a graphene monolayer. The large monolayer and the complex structure around were suitable for technical optimization and exploration of parameters for acquiring scans and spectra. Figure 4.8 (b) shows the central region using upconversion confocal scanning. The monolayer and smaller structures are clearly visible as homogenous bright areas.

Subsequently, the initial attempt was to collect the luminescence from a single spot to record a spatially resolved spectrum. Therefore the laser was focused constantly on a single spot of the monolayer. Without success with regard to a reliable spectrum, the monolayer was damaged. Changes in acquisition time and excitation power did not solve this problem. Figure 4.8 (c) shows a confocal upconversion scan where the bleached spots are clearly apparent (white arrows). The presence of these spots required further improvements.

The energy accumulated in a single spot of graphene is decreased when the sample is constantly moved through the laser focus. Hence, the scanning stage was set to move periodically over a rectangular area. At the same time a spectrum was acquired. The potential spectrum was supposed to be unchanged because no graphene edges or any other boundary were hit. Unfortunately, the graphene monolayer bleached again. The resulting confocal scan (figure 4.8 (d)) clearly shows the bleached area (white rectangle).

Besides that, images (b) to (d) demonstrate the evolution of the image quality.

Finally the signal-to-noise ratio was so low, that even small graphene islands and thin carbon stripes (upper left quarter of image (d)) could be detected. They were not apparent in the high contrast image. Although there are several interesting graphene structures, no undamaged monolayer is left in this area. Subsequently, another graphene flake was used to adjust scan area and speed as well as excitation power and acquisition time.

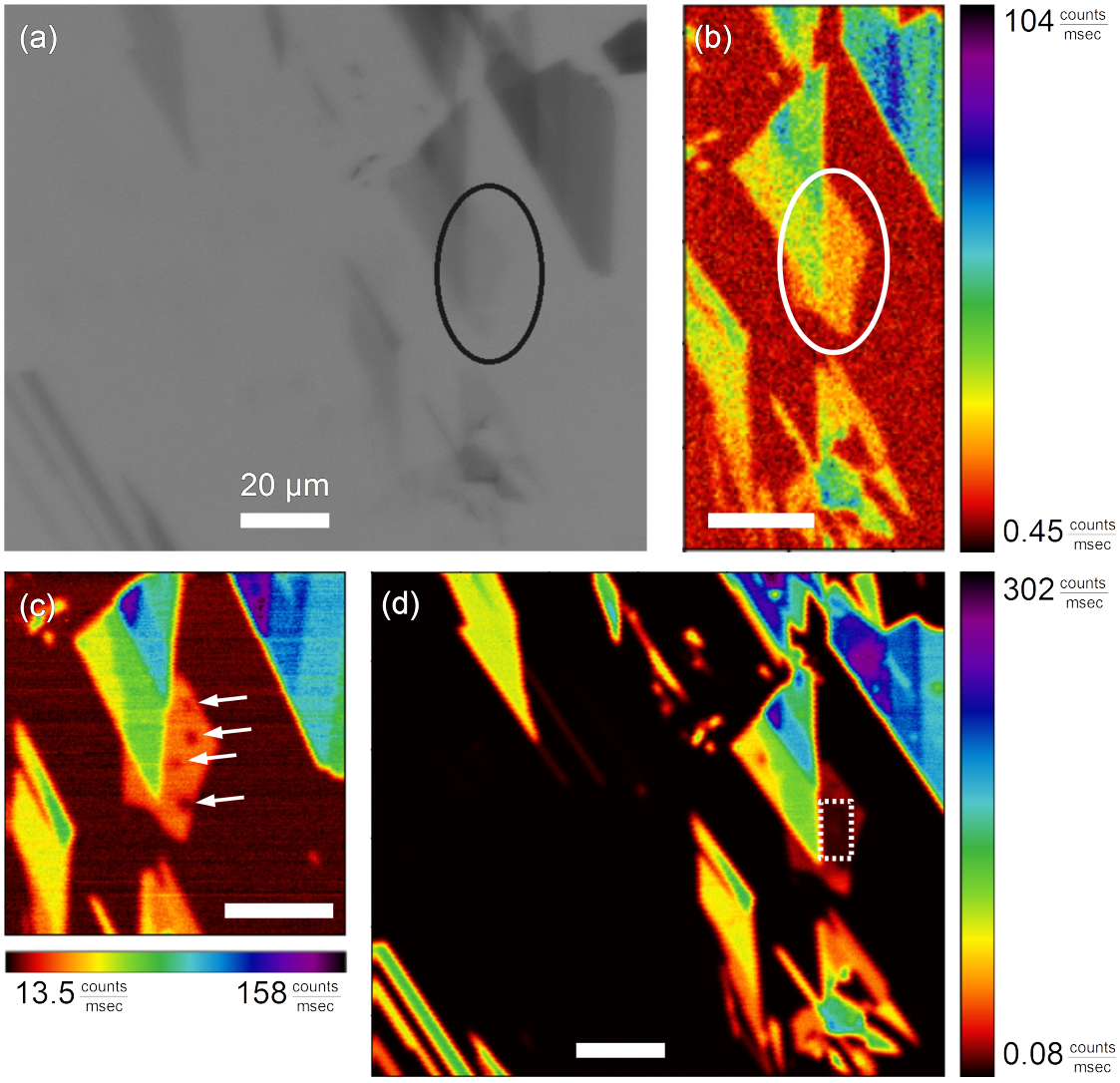

Figure 4.8: (a) High contrast image in white light microscopy. (b) - (d) upconversion confocal scans of graphene. The encircled region highlights the monolayer characterized by the contrast. The false color images represent the evolution of the scan quality. In attempt to record a spectrum, graphene was damaged on single spots marked by arrows (c) and over an extended area marked by the rectangle (d). All scale bars measure 20 μm.

Both the excitation power and the spectrometer acquisition time have to be set higher than a minimum value to reach a sufficient signal-to-noise ratio. Furthermore, the scan speed has to be faster than the threshold for damage graphene at the first pass-by. On the other hand, the cycle duration of the periodic scan has to be long enough so that the excited graphene can relax. In other words, the dumped

energy must not accumulate above the destruction threshold. All these parameters define a minimum size of the periodically scanned area.

The typical lateral size of single graphene flakes is in the range of a few micron. This is smaller than the minimum scan area. Thus, it became unavoidable to scan beyond the flake area. Consequently, the possibility of edge effects has to kept in mind. Figure 4.9 (a) presents a graphene flake and the scanning area. The size of the scanning area clearly exceed that of the graphene flake. Images (b) to (d) illustrate the same flake after a spectrum was taken, respectively. With a scan speed of 40 μm/sec and an excitation power of 18.6 mW, the first spectra could be recorded successfully. None of the images show any indication of degeneration. It turned out that the usable parameter range is very narrow. Before discussing the obtained spectra, the observations with regard to the degeneration will be presented.

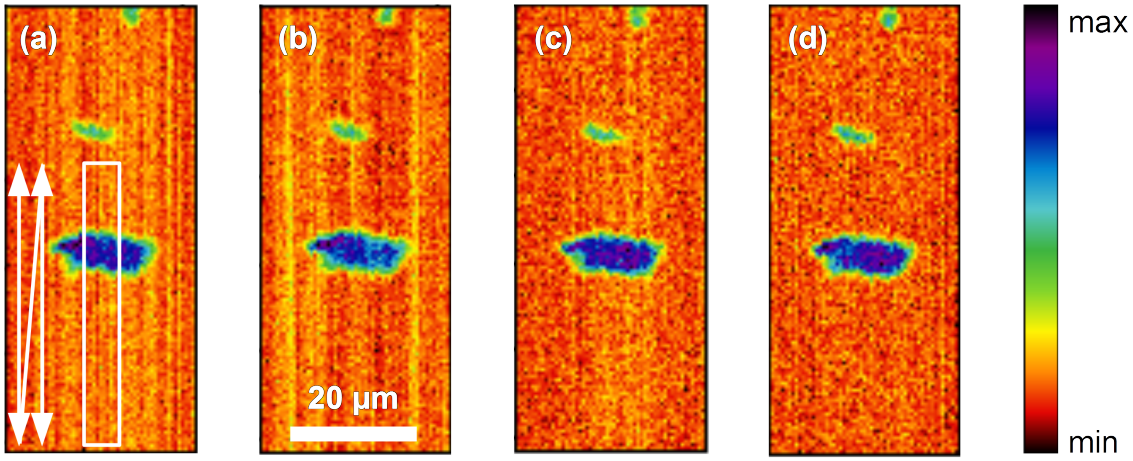

Figure 4.9: Acquiring spectra is performed during periodic movement of the sample through the laser focus. The scanned area is marked in (a) with a white rectangle. Between images (a) - (d) a spectrum was taken. No bleaching is observable. This documents the successfully achieved setting.

4.2.2 Degeneration of Graphene and Substrate

Even if the optical degeneration is not the main purpose of this thesis, it is worth to try to understand the underlying process. This subsection will present the results from fluorescence confocal and atomic force microscopy and will explain why "degeneration" of graphene is a more appropriate term than "destruction".

In the previous chapter, figure 4.8 has presented the bleaching of a graphene monolayer. In a first step holes were "burned" accidentally. In a second step, a larger area was degenerated. After the first step, the setup was changed to a fluorescence confocal scanning setup. The excitation was performed by a 532 nm cw laser and a longpass filter was used in the detection path. In this configuration the graphene is also expected to appear due to Raman scattering. The dominant G- and 2D-peak leads to scattered light with wavelengths at 581 nm and 621 nm, respectively.

The result is shown in figure 4.10 (a). As expected, the graphene appears because of Raman scattering. Furthermore, the former holes appear as fluorescent bright spots. The fluorescence of the spots exceeds the Raman signal of graphene even for thicker multilayer flakes. One has to conclude that a photochemical reaction

occurred during the upconversion bleaching process. The reaction product is a fluorescent structure embedded in the remaining graphene.

Figure 4.10 (b) is the confocal fluorescence scan right after the second bleaching step where an extended monolayer plane was degenerated. The degenerated area (compare figure 4.8 (d) on page 49) also occurs as a fluorescent plane. Similar to the spots in 4.10 (a) the fluorescence signal of the degenerated plane exceeds the Raman signal of the surrounding graphene. In contrast to most of the spots, the plane rapidly started bleaching under 532 nm illumination.

This leads to figure 4.10 (c). The fluorescence of the degenerated plane has been disappeared. Solely the fluorescence of some of the spots still exceeds the Raman signal from the surrounding graphene.

In short, all graphene sites which were bleached by infrared fs irradiation appeared fluorescent under cw excitation at 532 nm. After a certain time, the fluorescence also vanishes.

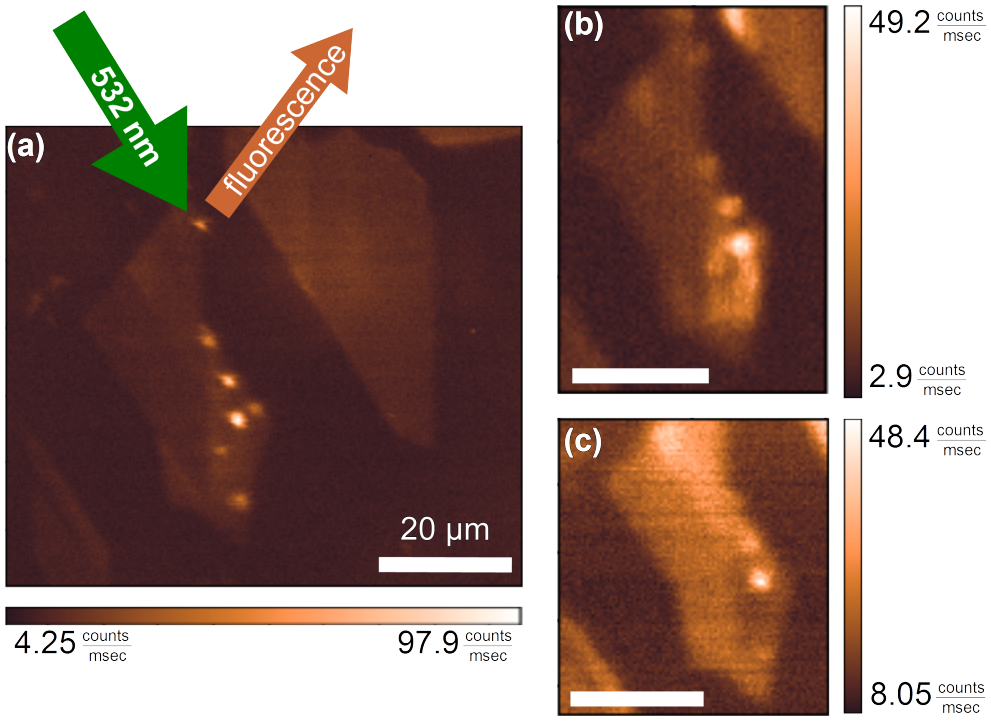

Figure 4.10: The graphene sample in a confocal fluorescence scanning setup. The sample is excitation by a cw laser at 532 nm. Graphene itself occurs because of Raman scattering. The fluorescence of the degenerated spots (a) as well as the degenerated plane area (b) are clearly brighter. The fluorescence of the degenerated graphene vanishes after some time of illumination (c).

Further insights were gained by atomic force microscopy of the bleached graphene. The AFM measurements were performed in the laboratories of the group of Prof. Rabe again. Mapping a graphene monolayer and even its substructure requires a very sensitive AFM. The result is presented in figure 4.11. Two images were merged so that the whole graphene flake including monolayer and fewlayer region is shown. All layers are well separated with respect to the topography. Additionally a fractal structure is present in the domain of each layer. According to chapter 3.1 and [43] this can be explained by a water submonolayer between graphene and

mica. Furthermore, relatively high structures at the edges of graphene were found which might stem from adsorbed particles. Since graphene is open for functional groups at the edges molecules can contaminate the sample. However no edge effects were observed during confocal scans. As mentioned before these structures could potentially play a role when spectra are recorded as one scans over the edges during signal acquisition.

Of special interest are the anomalies in the fractal structure. By comparing the AFM image with the former upconversion scans (figure 4.8 (c) and (d) on page 49) one notices the correlation with the bleached spots. The arrows in the figure help to assign the bleached spots. While at some spots just the fractal structure is interrupted, at other spots the topography is slightly elevated. In contrast to the spots, the large bleached plane has no equivalent in the AFM image. Since spotwise anomalies were also found on the pure mica surface (not shown), one has to conclude that also the substrate itself can be damaged by intense irradiation.

To conclude, the degeneration of graphene which occur as bleaching in upconversion experiments, is a photoinduced chemical reaction leading to fluorescent reaction products on the mica substrate embedded in the remaining graphene. The topology of graphene changes depending on the impact of the laser excitation. Even effects on the substrate can be observed.

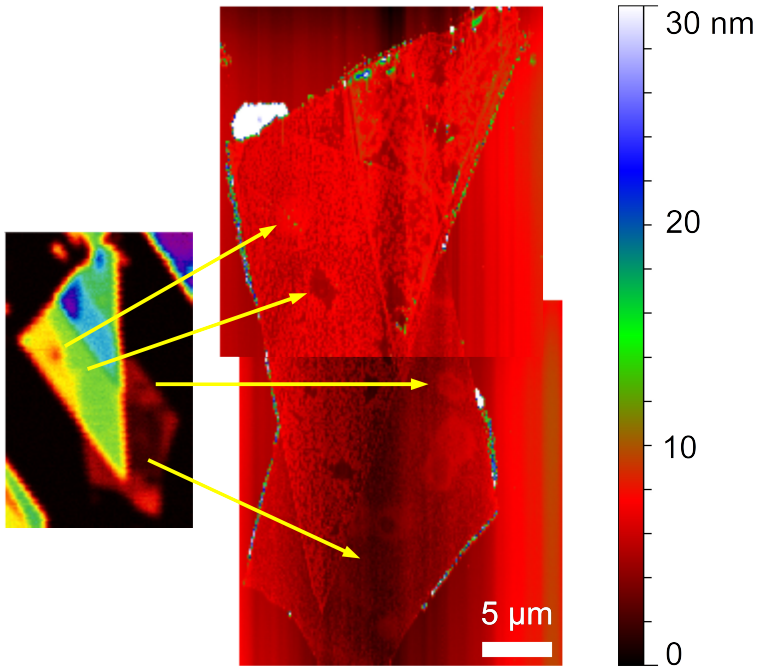

Figure 4.11: Atomic force microscopy image of the graphene flake. The bleached spots in the upconversion scan (left) appear in the AFM image as changes in surface structure and topography. This is not the case for the big bleached plane area. The fractal structure can be explained by water encapsulated between graphene and mica [43]. The accumulations on the edges did not cause distinct features in optical investigations.

4.3 The Spectrum of the Upconversion Luminescence after Femtosecond Excitation

In the previous chapters, the efficient imaging of graphene through upconversion confocal scanning after excitation with femtosecond laser pulses was presented. The difficulties of the degeneration by too intense excitation was discussed. The last section of this chapter presents and discusses the physical processes which become observable with or only by spectral analysis.

4.3.1 The Upconversion Spectrum from Graphene

Previously, the method of scanning to avoid degeneration of graphene enabled the acquisition of the following spectra possible. Figure 4.12 shows the upconversion luminescence spectrum obtained from graphene on mica, the contribution from pure mica and the difference. The difference between the mica and the graphene on mica signal is treated as the contribution from pure graphene. The spectra were acquired and processed as follows.

Before any spectrum can be taken, a confocal scan has to be performed. The confocal scans precisely determine the position of the former characterized graphene flake. The area for the periodic movement can be assigned as described above. After starting the periodic movement of the sample the spectrum is acquired. The mica contribution to the upconversion spectrum is encountered by choosing a scanning area next to the flake. All settings including lateral dimension of the area are kept constant. Repetition with blocked excitation laser path gives the background spectrum.

Typical results for the three spectra are shown as raw data in figure 4.12 (a). The excitation laser contribution appears as a broad peak around 960 nm and is not shown. The light green line corresponds to the background. Between 600 nm and 750 nm the background is dominated by stray light from the laboratory. At 532 nm the stray light peak from the pump laser is detected.

The pure contribution from the sample is obtained by subtracting the background. The background (light green) data is subtracted from the graphene (blue) as well as from the mica data (green). Every external light source which contributes to both the signal and the background is eliminated. Afterwards spectral correction of the data is necessary as described in chapter 3.2. Both the graphene and the mica data is corrected pointwise by the weighting function. The weighting function can be found in figure 3.8 in chapter 3.2. Especially in the long wavelength regime the spectrum rises up. Because the weighting function goes to zero at the lower and upper end the noise outside the measurement range is overrated by magnitudes. The resulting graphene and mica upconversion spectra are shown in figure 4.12 (b). One can clearly see how the spectrum becomes smooth by the background subtraction.

The pure graphene contribution is obtained by subtracting the mica data point by point from the graphene data. The underlying assumption is that both the pump beam and the mica luminescence are not depleted by passing the graphene layer. Finally, the graphene upconversion luminescence spectrum is plotted in figure 4.12 (c). After background subtraction, weighting and mica subtraction, the curve shows the typical smooth and monotonic behavior. The increasing noise in the upper wavelength range is caused by the weighting.

For comparison, the spectrum from another graphene flake is plotted as grey curve

in figure 4.13. The data was scaled to fit with the arbitrary units. Consequently the following discussion focus on the shape of the signal, not on the absolute value.

The main difference between both measurements is the change in pump power. The lower pump power of 5.6 mW leads to a shift of the spectrum towards higher wavelength. In contrast to the high power excitation at 18.6 mW no contribution below half the excitation wavelength of 480 nm can be detected.

The black curve in figure 4.13 shows the data for a graphene multilayer in the low excitation power regime. The shape is similar to that of low power excited graphene. This proofs that the change in shape belongs to the excitation power and not to the specific flake or the number of layers.

In summary, this chapter has presented the successful acquisition for different graphene samples and excitation power. The smooth monotonic spectra give rise to study the underlying physical process. In the next chapter, a graphene monolayer will be treated as source of blackbody radiation.

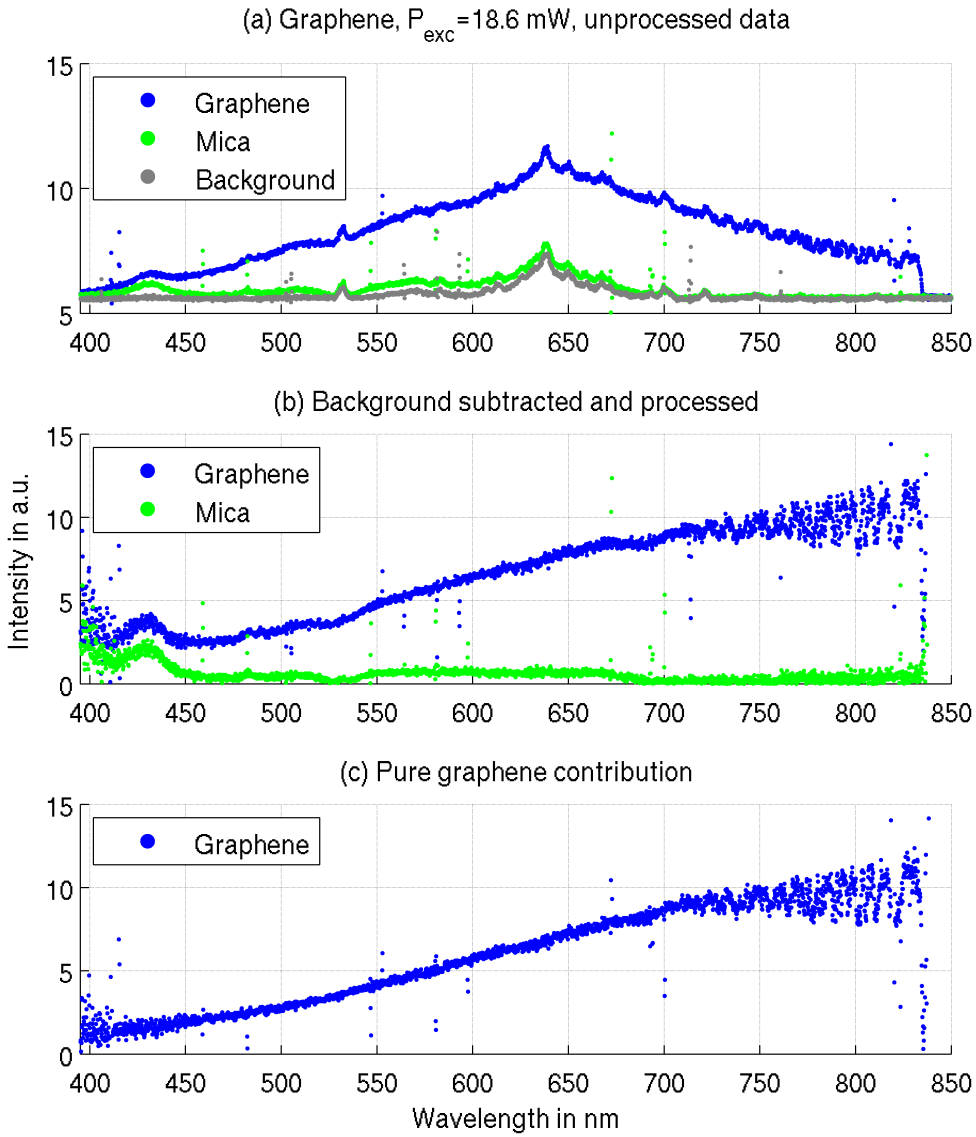

Figure 4.12: Upconversion luminescence spectrum of graphene after pulsed excitation at 960 nm. (a) The raw data is affected by the non-uniform setup weighting function, background and stray light. The graphene, the mica and the background contribution have to be taken into account. (b) Subtracting the background and weighting yields the luminescence spectrum for pure mica and graphene covered mica. (c) Subtracting the mica signal gives the final pure graphene contribution to the upconversion spectrum.

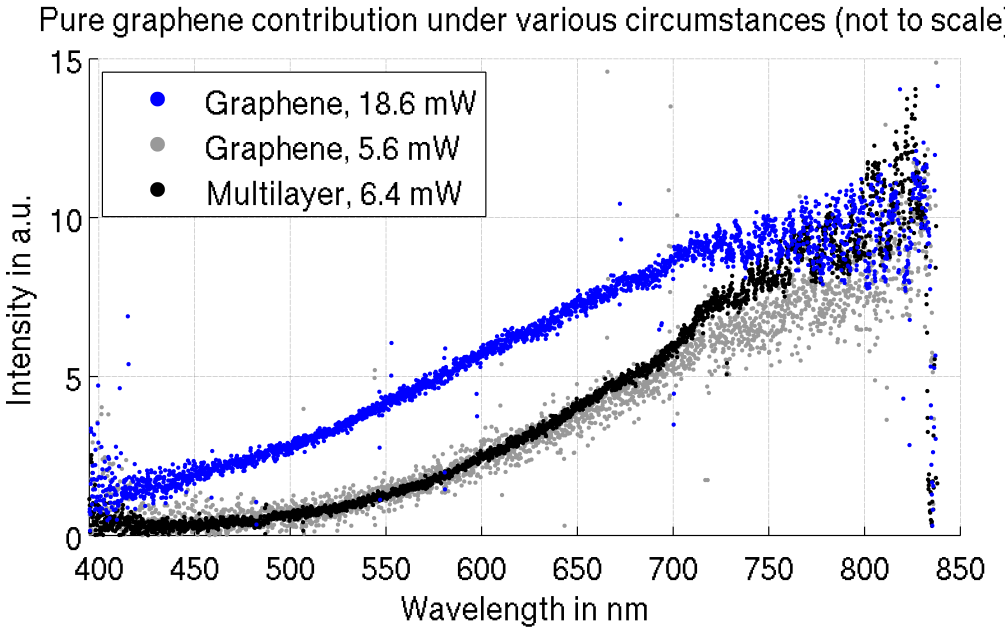

Figure 4.13: Comparing the pure graphene contribution in figure 4.12 to a low excitation power and a multilayer spectrum. The different graphs are not to scale. The plot shows that the shape of the signal depends on the excitation power.

4.3.2 Blackbody Radiation

In this chapter an interpretation of the derived spectrum will be given. As discussed in chapter 2.3.5, after optical excitation thermalization takes place [28]. The electronic excitations are largely thermalized among themselves, but are only partially equilibrated with strongly coupled optical phonons and essentially decoupled from other phonons [39]. The excitation of these optical phonons is the dominant relaxation channel. Besides that electron-hole recombination also takes place and leads to emitted radiation. In short, electrons and holes can be described as a gas of fermions with determined energy distribution which emits radiation as a blackbody.

Assume a spectral fraction of the emitted power at photon energy $\hbar\omega$. The corresponding intensity can be written as

$$I(\omega) = \frac{c}{4} w_E(\omega). \tag{4.4}$$

$w_E(\omega)$ is the spectral energy density of the electromagnetic field. Following Planck's law:

$$w_E(\omega) = \frac{\hbar}{\pi^2 c^3} \cdot \frac{\omega^3}{\exp\left(\frac{\hbar}{k_B T}\omega\right) - 1}. \tag{4.5}$$

An easy comparison with the experimental data requires Planck's law in terms of wavelength λ rather than in frequency ω. This leads to the wavelength dependent intensity

$$I(\lambda) = \frac{c}{4} \cdot w_E(\lambda) \tag{4.6}$$

$$= \frac{4\hbar\pi^2 c^2}{\lambda^5 \left(\exp\left(\frac{2\pi\hbar c}{k_B T} \cdot \lambda^{-1}\right) - 1\right)}. \tag{4.7}$$

However, graphene is not an ideal blackbody as only 2.3 % of the incident light is absorbed by each layer. Nevertheless, the absorption is almost constant in the entire visible and near infrared range [51]. Consequently, the emissivity which behaves like the absorption can easily be implemented by a prefactor.

Furthermore, only a fraction of the whole intensity is collected by the objective and the intensity is obtained in arbitrary units. This leads to another constant prefactor in the model. These considerations and the natural constants in equation 4.7 are expressed through the constant $C_1 \cdot 10^{20}$. Introducing a second constant $C_2\,(T) = (2\pi\hbar c)\,/\,(k_B T)$ leads to the following blackbody model for graphene:

$$I(\lambda) = \frac{C_1 \cdot 10^{20}}{\lambda^5 \left(\exp\left(C_2 \cdot \lambda^{-1}\right) - 1\right)}. \tag{4.8}$$

When C_2 is obtained from a nonlinear fit, one can calculate the temperature:

$$T = \frac{2\hbar\pi c}{k_B C_2}. \tag{4.9}$$

Figure 4.14 shows the emission spectrum of the graphene flake F3. The monolayer was presented in chapter 4.1.1, characterized by Raman spectroscopy and imaged by upconversion confocal scanning.

Two spectra were acquired while moving the monolayer periodically through the laser focus to avoid degeneration. The excitation was set to 5.2 mW ($\hat{=}$12000 μJ/cm^2) and 18.2 mW ($\hat{=}$42000 μJ/cm^2), respectively. The acquisition time was set as low as possible and was kept constant for consistence.

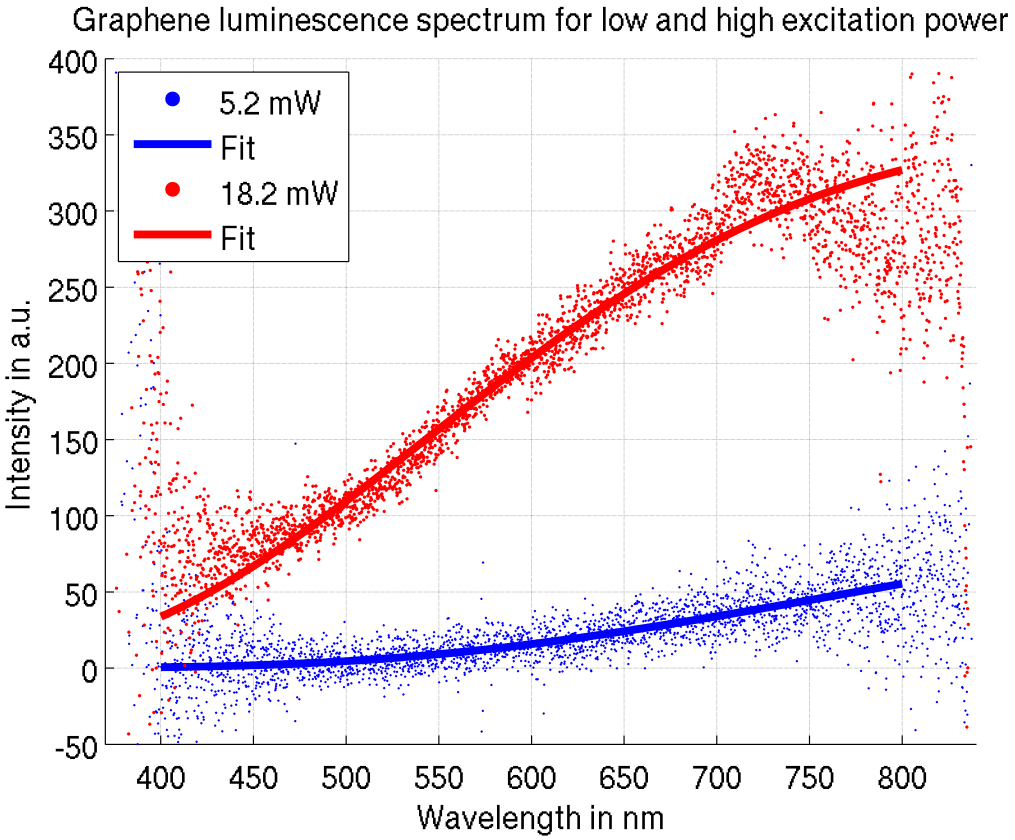

Figure 4.14: The upconversion spectrum of a graphene monolayer for two different excitation powers is acquired while the sample is constantly moved through the laser focus. Beside the power, all other parameters were kept constant. The blackbody model, equation 4.7, is fitted to the data yielding the temperatures $(2210 \pm 62)\,\mathrm{K}$ (blue) for the lower and $(3116 \pm 10)\,\mathrm{K}$ (red) for the higher excitation power.

exc. power	calculated fluence	C_1 in a.u.	C_2 in nm	Temperature
5.2 mW	$12000\,\mu\mathrm{J/cm^2}$	0.62 ± 0.16	6500 ± 180	$(2210 \pm 62)\,\mathrm{K}$
18.2 mW	$42000\,\mu\mathrm{J/cm^2}$	0.3463 ± 0.0085	4618 ± 15	$(3116 \pm 10)\,\mathrm{K}$

Table 4.2: Obtained parameters from fitting the blackbody model, equation 4.7, to the data in figure 4.14. The change of the absolute signal and the shape is explained by the temperatures extracted from the model.

The evolution of the spectrum is obvious. A higher excitation power leads to an increase of the luminescence at every wavelength. The obtained data is fitted with the blackbody model. The resulting constants demonstrate the non-uniform evolution. The temperatures extracted from C_2 are $(2210 \pm 62)\,\mathrm{K}$ and $(3116 \pm 10)\,\mathrm{K}$ for 5.2 mW and 18.2 mW, respectively. These values seem to be very high on the one hand, but demonstrate how the amount of dumped energy is converted into a high temperature on the other hand. Furthermore, these high values could lead to an explanation of the degeneration of graphene at higher excitation power. However, the luminescence arises from the electron gas and not from the crystal lattice [28]. The conversion from the inner energy of the electron gas to the inner energy of

the lattice would only lead to a small rise in the lattice temperature. In [52] the lattice temperature is estimated to increase by 60 K when a 10^4 K hot electron gas is relaxing. Conclusively, a phase transition like melting is not expected.

Not a phase transition, but a chemical reaction could be induced or catalyzed by the hot electron gas. It is known that hot electrons in their transient higher-energy state can excite electronic or vibrational transitions in molecules adsorbed on metal surfaces and thus catalyze chemical reactions [53]. In the case of graphene, the hot electron gas would induce a reaction of the graphene itself. A reaction e.g. with oxygen from the atmosphere or water from the surface could explain the bleaching in the upconversion confocal scanning. A fluorescence spectrum of the reaction product could shed some light on the underlying process.

4.3.3 Second Harmonic Generation

So far, nonlinear optical behavior of graphene was observed in the sense of a spectrally broad photoluminescence. The spectrum and its interpretation explains it as incoherent light emission. In contrast, as described in chapter 2.3.5 and 3.1, second harmonic generation from mica and from graphene was measured in [42] and [40], respectively, but no spectrum was presented. The results obtained during this thesis clearly show luminescence at twice the excitation energy without necessarily being explained as second harmonic generation. An accurate analysis should provide a spectrum where both the incoherent and the coherent contribution are clearly recognizable.

Second harmonic generation is theoretically described in chapter 2.3.1. From the condition for the wavevectors follows that SHG intensity is expected mostly in the direction of the incident light. The geometry of the setup used in this thesis is particular unsuited for this purpose since excitation and collection are done by the same objective. A first step towards an improved collection of SHG signal is an additional mirror on top, just lying on the top backside of the sample (figure 4.15 (a)). This simple solution is not optimal since the SHG light must be scattered back from the mirror and is thus only badly focused. However, the following spectra show that enough light reaches the spectrometer to detect second harmonic generation from the sample.

Figure 4.15 (a) illustrates the geometry of the objective, the upside-down mounted sample and the mirror on top. The confocal scan depicted in (b) remains almost unchanged. The white rectangle indicate the area used for periodic movement while the spectrum is acquired.

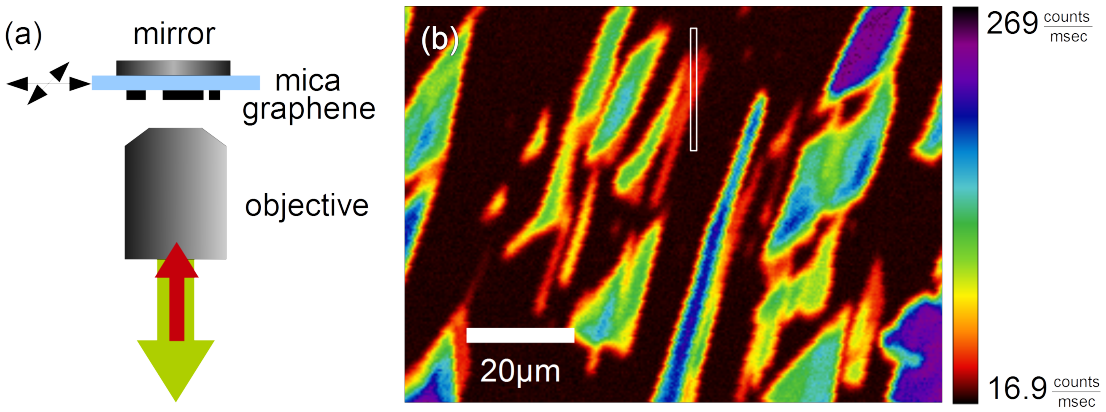

Figure 4.15: (a) A mirror was placed on top of the sample to collect forward emitted light. (b) The white rectangle in the upconversion confocal scan marks the region for spectral analysis.

The result is given in figure 4.16. The high excitation power of 18.6 mW leads to the typical broad spectrum exceeding twice the excitation energy. Additionally, a peak appeared between 470 and 490 nm in the spectrum of graphene on mica. To clarify the origin of the peak, the second spectrum is recorded for a region of pure mica next to the graphene flake. It shows the typical mica response as seen before but also with a little peak. Subtraction of the two plots give the contribution of pure graphene or graphene induced enhancement. Obviously, the additional peak is still present on top of the broad spectrum.

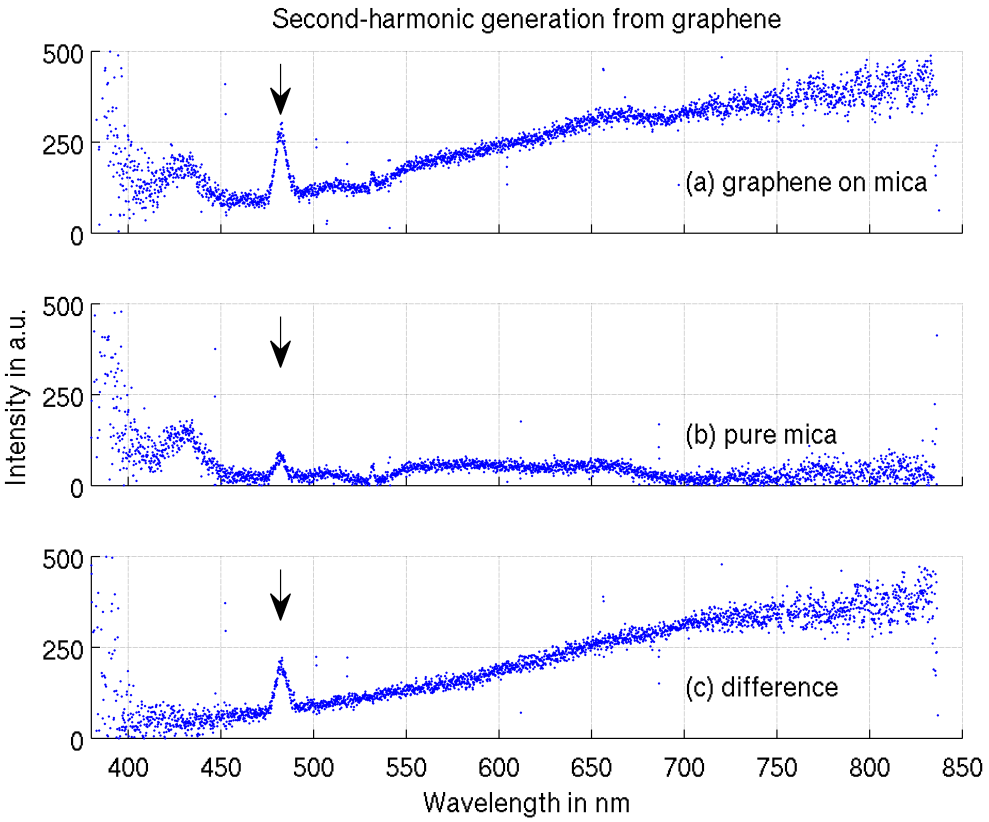

Figure 4.16: The upconversion luminescence spectrum when a mirror is placed on top of the sample for graphene on mica (a), the pure mica contribution (b) and the difference between both (c). The difference, attributed to pure graphene, clearly shows a second harmonic peak on top of the broad luminescence spectrum.

The verification that the process is indeed second harmonic generation can be performed by comparing SHG peak and laser spectrum. The laser spectrum is recorded simultaneously since a small amount is transmitted through the shortpass filter. It is plotted in figure 4.17. Equation 2.45 in chapter 2.3.1 allows to calculate the dominant contributions to the SHG peak. Each intensity value for a specific wavelength component will appear squared at the half wavelength. Due to the additional incoherent luminescence and the unpredictable conversion efficiency the offset and the amplitude of the SHG peak must be estimated. Hence, the expected shape of the SHG peak is derived from the laser spectrum. The amplitude and offset is fitted to the data. The result is plotted together with the spectrum of graphene on mica in figure 4.17. The calculated shape of the peak is in good agreement with the obtained data. The small horizontal shift can be explained with imperfections in the spectrometer calibration.

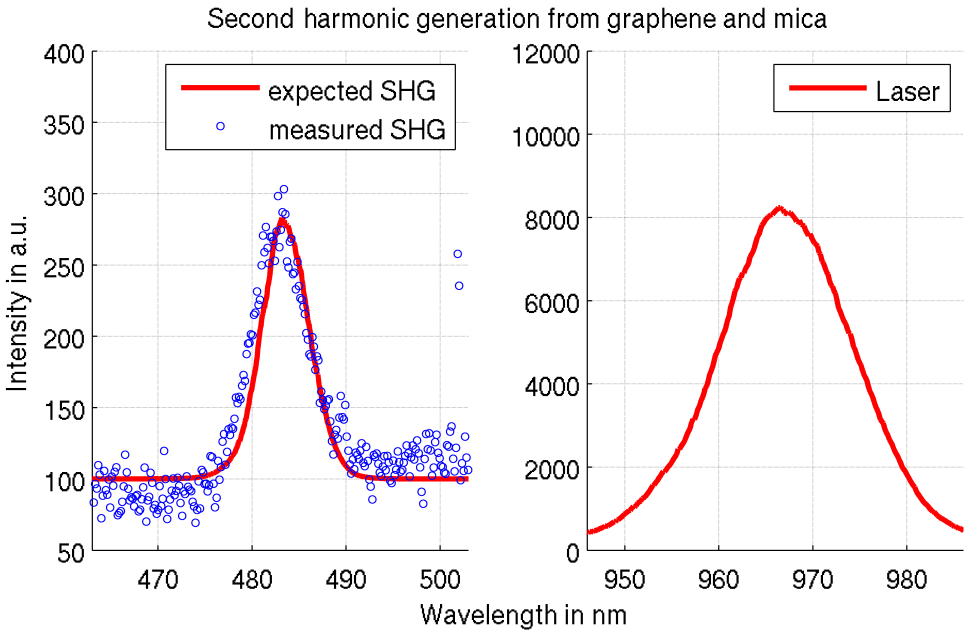

Figure 4.17: From the laser spectrum (right) calculated expected second harmonic peak shape (left, red line). The peak in the spectrum clearly behaves like a second harmonic peak. The amplitude and offset are fitted to the data.

In summary, a little change in the setup made the investigation of SHG possible. A peak at half of the laser wavelength appeared for pure mica and, significant higher, for graphene. The shape of the peak clearly shows the expected behavior of second harmonic generation.

Unfortunately, the peak varied in amplitude and vanishes from time to time and from sample to sample. A first approach has explained this by aging of the sample when stored and handled under ambient conditions. This explanation failed for the last sample which was freshly fabricated and well characterized by Raman spectroscopy. Therefore, the reproducibility for the existence of second harmonic generation from graphene is not proofed within this thesis. Possible reasons for variations of the SHG peak and non-reproducibility are summarized in the following table.

possible reason for non-reproducibility of SHG	test or suggestion for improvement	experiment performed?
wrong layer assumption	Raman spectra for verification of monolayer and fewlayer graphene	performed, inconclusive
humidity dependence	performing measurements for different humidities and under N_2 atmosphere, sample stored in N_2 for more than 12 hours	performed, inconclusive
excitation wavelength	laser tuned between 1000 nm to 950 nm	performed, inconclusive
position of the attached mirror	mirror moved	performed, inconclusive
laser pulse shape	spectral characteristics of cw- and pulsed mode recorded	performed, inconclusive
laser polarization vs. lattice orientation and mica birefringence	sample rotated by 45 and 90 degree	performed, inconclusive
setup alignment, laser focus	setup aligned, focus checked	performed, inconclusive
mirror on top leads to a pump-probe like geometry, strong dependence on time between both pulses	controlling mica thickness, use a transmission microscopy setup	no
SHG effected by edges, enhanced mode density	use larger graphene monolayer, explicit study on the edges	no
substrate dependence	use another substrate (preparation on glass failed)	no
ambient conditions, further uncontrolled parameters	improve experimental and storage conditions	no

Table 4.3: List of possible reasons for the non-reproducibility of second harmonic generation. The reason why the second harmonic peak does not appear on the last sample has not been found.

5 Summary and Discussion

The results accumulated during this thesis will be summarized in this chapter. It will be discussed how the results meet the theoretical expectations, how they compare with the literature and what insight could be gained by studying the upconversion luminescence of graphene. After explaining the advantages of upconversion confocal microscopy as imaging technique, the underlying physics of incoherent upconversion is presented. Furthermore, the inconclusive observation of second harmonic generation will be discussed. This discussion ends up at the initial motivation, i.e. the question of plasmonic modes in graphene in the visible spectral range.

5.1 Upconversion Confocal Microscopy as Imaging Technique

Within this thesis, an upconversion confocal microscope for the investigation of graphene was developed and further improved. This allows the scanning of graphene samples by excitation in the near infrared and detection in the entire visible spectral range. Graphene on mica was fabricated by mechanical exfoliation by members of the group of Prof. Rabe.

Afterwards the samples were characterized. High contrast imaging (chapter 3.1.2) was used to find fewlayer graphene flakes. It turned out that this method is not always reliable but it allows a fast examination of the whole sample. Raman spectroscopy (chapter 3.1.3) was used to explicitly identify monolayer flakes.

Chapter 4.1.1 presents the whole characterization procedure and the corresponding upconversion confocal scan. The monolayer flakes appear clearly. The signal of the multilayer structures correlate with the contrast in the high contrast image. A thicker multilayer emits more upconverted radiation than a thinner one. Furthermore, even tiny carbon structures appear. Small luminescent flakes and long stripes are e.g. shown in figure 4.8 in chapter 4.2.1. The direct comparison with the high contrast image proofs that upconversion scanning can depict carbon structures which were not apparent in the high contrast image. The contrast itself is dependent on the excitation power as described in chapter 4.1.3 and on the background. The background is found to be fluorescence from mica. When the laser is operated at an elevated wavelength, the fluorescent light can pass the shortpass. Tuning the laser to a smaller wavelength reduces this effect.

Furthermore, the resolution of the upconversion scan can be easily improved by using an objective with higher numerical aperture. A $NA = 0.6$ objective was used. Installing for example a $NA = 1.2$ oil immersion objective would double the resolution. This is not possible for high contrast imaging because a higher angular spread would decrease the layer contrast.

In chapter 4.2 the degeneration of graphene flakes after long and intense illumination is demonstrated. The optical absorption of graphene is of the same magnitude

in both the NIR and the visible spectral range. Accordingly this issue is expected whenever graphene is exposed to intense radiation. Within this thesis, upconversion scanning was used to image the degenerated sites. To establish this method in other research fields seems to be reasonable.

In summary, upconversion confocal scanning was shown to be a powerful tool for mapping graphene and other graphene like structures on the surface of mica. The contrast depends on the excitation power and the resolution is principally only diffraction-limited but could be also combined with SNOM techniques.

5.2 Incoherent Upconversion: The Underlying Physics

Besides the technical advantages of mapping, the upconversion luminescence can gain further insight into the charge carrier dynamics in graphene. The intensity dependence as well as spectroscopic investigations were performed during this thesis.

As mentioned in the former chapter, the emitted upconversion intensity and the graphene layer contrast vary with the excitation intensity. Chapter 4.1.3 gave a test series of several confocal scans obtained at different excitation powers. The series demonstrates the usable range. For the low excitation power the signal-to-noise ratio is not sufficient to detect monolayer graphene. Above $\sim 2\,\mathrm{mW}$ the monolayer flake is visible. The average count rate for the graphene monolayer, a multilayer and the mica substrate is extracted and plotted in a loglog plot to determine the order of the nonlinear optical process. Constant slopes slightly higher than 2 were measured for both monolayer and multilayer graphene. This indicates a process which is dominated by a second order optical process. It has been shown in chapter 4.3.2 that the broad spectrum shifts toward lower wavelength for higher excitation energy. However most of the signal appears at long wavelengths. The rise of the quantum efficiency toward 700 nm would therefore result in a slightly underestimated slope. This proofs that even higher order optical processes are involved. In [1] and [39] the upconversion luminescence is explained by excited charge carriers after one photon absorption followed by scattering along the Dirac cone. After thermalization the recombination reflects the population density of holes and electrons in valence and conduction band, respectively (see chapter 2.2.3). Efficient scattering is expected from graphene because of its linear band structure (chapter 2.3.1) but not from graphite. The bandstructures for graphite and graphene in figure 2.4 in chapter 2.2.2 show clearly a difference. The curved bands of graphite should result in a different signal.

An alternative explanation for the excitation intensity dependence would be a two photon absorption. This does not exclude scattering. Indeed, both processes together could explain both populations at high energy levels and a slope higher than two. However two photon luminescence is claimed to be ineffective for graphene by [38]. The statement is based on pump probe measurements indicating only a linear change in transmission of excited graphenes. This work is also cited to [1] in order to neglect TPL. Both publications have in common that the pump fluence is by magnitudes lower than those used in measurements presented in this thesis.

Further insight is gained by spectral analysis. Chapter 4.2 illustrates the way towards a suitable parameter range. Finally, in order to avoid degeneration of graphene spectra were acquired while moving the graphene flake periodically through

the laser focus. The pure mica contribution to the upconversion spectrum was subtracted to obtain the pure graphene contribution. In chapter 4.3.1 figure 4.12 present the pure contribution to the upconversion spectrum from graphene at high excitation power, at low excitation power and for a multilayer flake at low excitation power. These three curves indicate that the shape of the upconversion spectrum depend only on the excitation power. The spectrum of lowlayer and multilayer are similar for comparable excitation power. This observations fit to the explanation of the intensity dependence obtained from the confocal scans. Whatever is leading to the upconversion, must be the same for graphite and graphene.

Two spectra of a clearly identified monolayer flake is given in chapter 4.3.2. The spectra only differ in excitation power. Both, the spectral shift and the increase of the integrated signal are recognizable. The model of a blackbody radiator was fitted to the data. The fit converged towards the data and indicated radiation comparable to that from a blackbody at 2200 K and 3120 K for low and high excitation power, respectively. This reveals the luminescence to be thermal radiation from a thermalized hot electron gas. The obtained temperatures are in agreement with the literature [39] even though a lower fluence but shorter pump pulses were used.

The high temperature of the electron gas could explain the degeneration of graphene at higher excitation power. A fluorescence spectrum of the reaction product could shed some light on the underlying process. Nevertheless this does not explain the excitation process.

In short, thermal radiation was found to be the fingerprint of the upconversion process. From the data accumulated in this work the upconversion process appears to be independent from the number of layers. This is revealed by similar intensity dependence and similar spectral distribution for monolayer and multilayer graphene flakes.

5.3 Second harmonic generation

A small modification of the setup allowed to detect forward scattered frequency doubled light. A mirror on top of the backside of the sample reflects the emitted light back to the objective. The mirror image of the sample is slightly shifted from the focal plane of the objective. Nevertheless, an amount of SHG light is able to reach the detectors.

Comparing the mica spectra with and without mirror indicates that SHG is detected. Although mica is a centrosymmetric crystal SHG is expected from the bulk (chapter 3.1.1). Every sample showed the SHG peak from pure mica when the mirror is set on top. The sample can be moved piezo controlled over an area of $\sim 100\,\mu\text{m} \times 100\,\mu\text{m}$. Within this area no changes of the pure mica SHG were observed.

Under special circumstances, the SHG peak was enhanced at the graphene covered mica sites. In chapter 4.3.3 an exemplary spectrum is shown. The SHG peak appears on top of the broad incoherent upconversion spectrum. It is increased by a factor of ~ 3 compared to bare mica. Comparing the SHG peak shape with the laser peak shape confirms that the underlying process is indeed second harmonic generation. Subtracting the mica signal from the graphene on mica signal gives the pure graphene contribution. From the data it is not clear if the peak is an addition of SHG from mica and SHG from graphene or if the graphene induces an enhancement of the SHG from mica.

However, so far the data is not reproducible. First observations indicated a vanishing peak when the sample is used and stored for a couple of months. This hypothesis was falsified by the last sample. An enhanced SHG peak did not appear even though it was the best characterized sample.

A list of possible reasons is given in chapter 4.3.3. Several experiments were performed using the last sample in order to find an enhanced SHG peak again. These experiments excluded reasons like a misaligned setup, laser pulse shape, wavelength or polarization influences, atmospheric humidity dependence, a former wrong layer assumption and the on-top mirror position. It could not be excluded, that the pump-probe like geometry, effects on graphene's edges, unnoticed mica inhomogeneities or further uncontrolled parameters due to the ambient conditions influences the signal.

Apart from the non-reproducibility no spectrum of SHG from monolayer graphene is reported. In [40] upconverted light at half of the laser wavelength is claimed to be SHG because of its isotropic behavior. This is discussed in detail in chapter 2.3.5. The spectra presented in this thesis clearly show two contributions. At sufficient excitation power the signal consists of the spectrally broad incoherent isotropic thermal radiation and additionally the coherent spectrally narrow second harmonic generation. The presentation of a spectrum and the correlation with the laser pulse is therefore indispensable to proof second harmonic generation.

5.4 Plasmonic modes in Graphene

The initiating motivation for this project was to clarify on the question if there are plasmonic modes in graphene in the visible spectral range. Beside the insights into charge carrier dynamics and nonlinear graphene optics the observations should provide an answer.

Upconversion confocal scanning was performed, the results are shown and the physical reason for the spatial homogenous luminescence is discussed. This was mostly motivated by the investigation of the plasmons in gold nanoprisms [36] as discussed in chapter 2.3.4. The intensity of two-photon luminescence appeared to be modulated according to the surface plasmon local density of states. Mapping the TPL is equal to record the convolution of SP-LDOS and beam profile.

In this thesis, several upconversion scans were performed. To make sure that possible resonance features are not suppressed by spectral integration, a spectrally filtered scan was performed (chapter 4.1.2). Nevertheless neither in this nor in any other scan resonance features on graphene or on graphite appeared like those in [36].

The interpretation of this result is independent from the reason of the broad luminescence, i.e. efficient scattering or two-photon luminescence. Any plasmonic mode should increase the electromagnetic mode density which should lead to enhanced conversion in both cases. Consequently, two results are possible.

First, the modulation happens on a length scale below the diffraction limited or is to weak compared to the absolute luminescence. This would fit to the result in [2] where the plasmons in the visible spectral range are supposed to have a wavelength of 9nm and decay within a few wavelengths. This length scale is clearly below the diffraction limit. The second interpretation is a vanishing plasmonic density of states. This would refute the existence of plasmons. Conclusively, an answer cannot be found from this measurements.

The second probe for plasmonic modes presented within this thesis is second harmonic generation. As described in chapter 2.3.3 plasmons can induce a large nonlinear polarization which in turn causes a resonantly enhanced emission of the second harmonic light. Therefore investigation of the spectral, spatial and time dependence of SHG can gain insight into the plasmonic properties. In the case of graphene, the purpose can be to study SHG from graphene itself or from enhancement of mica's SHG in the vicinity of graphene. Unfortunately, the detected additional SHG contribution from graphene covered mica sights could not be reproduced. A list of possible reasons was given in chapter 4.3.3.

One of the unexamined possibilities is the interaction of graphene with both the incident pulse and the reflected pulse. The first pulse interact with graphene and the following reflected pulse could probe the excited graphene. Assuming a mica thickness of 200 μm, the time shift between both pulses is 2.1 ps. The charge carriers are not relaxed within this time as shown in chapter 2.2.3. F. Javier García de Abajo introduced the idea of a transient plasmon [52]. This idea follows his calculations for intraband processes and plasmons in the infrared in doped graphene. The plasmons are allowed by an energy gap where electron-hole excitation is forbidden due to Pauli blocking (see chapter 2.2.3 for details). The energy gap is determined by the Fermi energy. A heated Fermi gas has a shifted Fermi energy. According to [52] the shifted Fermi energy reads as

$$E_F(T, E_F^0) = E_F^0 + 2k_B T \ln\left(1 + \mathrm{e}^{-E_F^0/k_B T}\right) \tag{5.1}$$

with the temperature T and Boltzmann's constant k_B. The relation is plotted for different initial Fermi energies E_F^0 in figure 5.1. The results of chapter 4.2 have shown degeneration of the graphene samples at sufficient high excitation power. The associated temperature for strongly excited graphene was determined to be slightly above 3000 K (chapter 4.3.2). Conclusively, electron gas temperatures above 4000 K are unattainable. This is not high enough to access a sufficient doping level to attend the infrared plasmons to the visible spectral range. However, only intraband excitations were considered in this model. An interaction of excited graphene with the reflected pulse could be also driven by single and collective interband transitions. These interactions would be effective on time scales in the picosecond and subpicosecond range. A small change in the setup geometry like mirror-graphene distance or pulse shape could have an influence. This so far uncontrollable influence could effect the reproducibility of the second harmonic peak. Nevertheless, the possibility to use second harmonic generation to probe plasmonic excitations in excited graphene has potential but requires more control and probably a modification of the setup as described below.

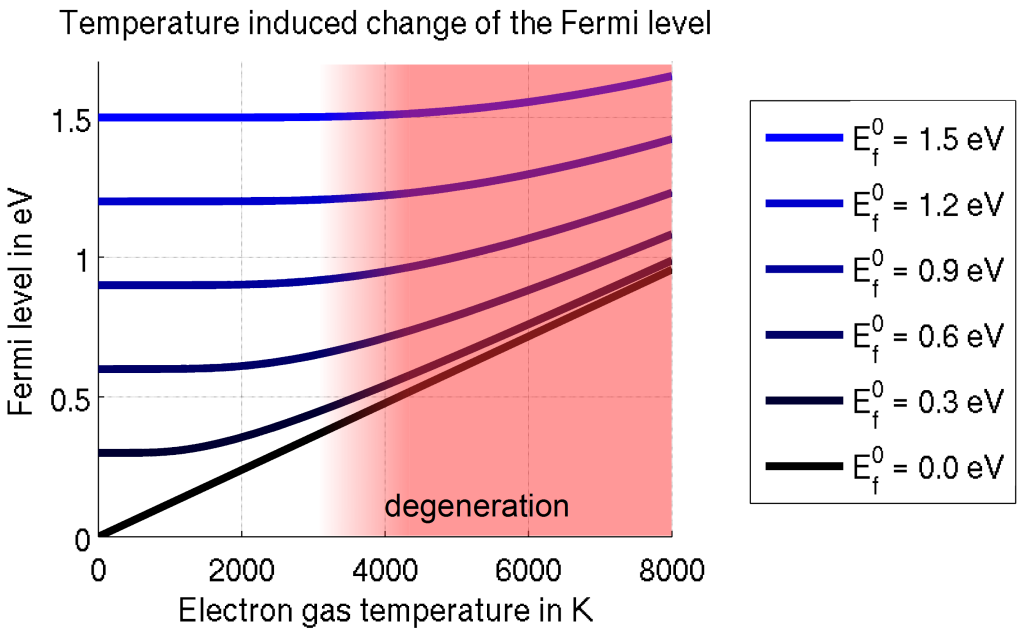

Figure 5.1: Shift of the Fermi level for a heated electron gas. The degeneration threshold limits the temperature. The effect becomes negligible at high initial doping levels E_f^0. Observable effects lie in the infrared spectral range only.

6 Conclusion and Outlook

In this thesis the luminescence of graphene in the visible spectral range was studied after excitation with fs laser pulses in the infrared. A setup was developed and characterized for upconversion confocal scanning and spectroscopy. The combination of sensitive photodetection by an APD and spectral analysis using an efficient spectrometer and a cooled camera provide a flexible and powerful tool for investigations. The study of graphene's optical response at energies in the range of visible light is of interest for the understanding of its charge carrier dynamics and can gain insight into fundamental electron relaxation and collective excitation processes.

Upconversion luminescence is a powerful tool for graphene imaging. Monolayer graphene flakes, characterized by white light microscopy and Raman spectroscopy, on mica were mapped. Their luminescence is controlled by the excitation power which allows to obtain high contrasts between graphene and mica. The signal increases for increasing layer thickness of few- and multilayer graphene. In order to obtain the underlying physical processes, spectrally filtered and excitation intensity dependent upconversion scans were performed. The upconversion is dominated by second-order nonlinear optical processes and is emitted homogeneously over the whole graphene plane. Furthermore it has been shown that also higher orders must contribute and that multilayer graphene behaves similar to monolayer graphene. While efficient scattering of excited charge carriers is expected from monolayer graphene only, also two-photon absorption must be considered.

It was shown that too intense optical excitation damages graphene. The degeneration is observed by bleached sites in upconversion scans. Degenerated spots and areas were studied by confocal fluorescence microscopy and atomic force microscopy. From the fluorescent leftover one has to conclude that graphene is not simply ablated. Instead, an optical induced chemical reaction induced or catalyzed by the hot electron gas must have happened. The topography of the damaged sites reveals changes of the water layer between graphene and mica and changes of the mica surface itself. The obtained experiences were used to develop a high excitation spectroscopy method for graphene.

By moving the sample periodically through the laser focus, spectroscopic measurements were performed without damaging graphene. Processing of the data allowed to extract the pure graphene contribution from the joint graphene on mica response. Further it has been shown that the upconversion luminescence depends on the excitation power and not on the layer thickness. A blackbody model was fitted to the spectrally broad emission which exceeds even twice the excitation photon energy. The temperature of the highest excited electron gas in monolayer graphene was found to be 3120 K. A small modification of the setup allowed the spectral observation of second harmonic generation. Second harmonic generation is detected from the mica substrate. In contrast to mica enhanced SHG from graphene was detected to be strongly variable. Depending on the sample and its age the SHG signal vanished completely. The reasons for the variation is not found.

The initial motivation of this thesis was to use optical upconversion to inves-

tigate plasmonic modes in the visible spectral range. This was motivated by reported strongly plasmon influenced two-photon luminescence in gold nanoprisms and enhanced second harmonic generation in thin silver films. So far, neither spatial modulations nor reliable enhanced second harmonic generation has been found from graphene. The reason could lie in the specific properties of the plasmonic modes or in their absence.

The key could be based on the spectroscopic observation of second harmonic generation. No spectrum is published for the second harmonic generation from graphene. Based on the result that various processes can lead to emission at half of the excitation wavelength, a spectrum as shown in this thesis is absolutely necessary. Perhaps the variation of the SHG peak is an effect of different circumstances leading to different plasmonic density of states. Consequently future measurements should focus on the spectral observation of second harmonic generation and on the reproduction of successful observations.

The setup could be optimized for this purpose in contrast to its actual state which allows spectroscopically broad detection. This includes a selection of optical components which fit perfectly to half of the excitation wavelength. Furthermore the detection beam path could be redesigned to avoid losses in particular unnecessary components.

A significant change would be the rearrangement of the spectrometer and the APD. Using the spectrometer as a monochromator and detect the spectrally filtered emission with the APD would increase the detection efficiency for a specific wavelength. Furthermore, tunable spectrally filtered confocal scans would be possible. The possibility to detect spatial dependent second harmonic generation could improve the search for its reasons and consequently for plasmonic activity.

A second significant development would be the installation of a transmission setup. So far excitation and emission pass the same objective. Due to the large spectral separation focus imperfections are unavoidable. Above the scanning stage the AFM sits on a tripod. Rebuilding the tripod, installing a microscope objective instead of the AFM and establish optical access would give the possibility to excite from the top. The excitation would be done as usual by the lower microscope objective. This geometry would replace the mirror in SHG measurements. The uncertainty regarding the second pass of the pulse would be eliminated automatically.

Beside the plasmonic properties graphenes unique band structure inspires the research on several fields. The detected upconversion luminescence represents the charge carrier distribution in optically excited graphene. Very recent, in August 2015, R. Jago, T. Winzer et al. published their theoretical suggestions to use graphene as a gain medium for broadband lasers [54]. Based on the same theoretical calculation as used in chapter 2.2.3 the population inversion is caused by a highly excited thermalized electron gas. This is the same inversion which leads to the upconversion luminescence reported in this thesis.

Furthermore the bandstructure and the 2D confinement allows tuning of graphene and coupling to numerous quantum emitters. Resonant energy transfer processes could be used to control luminescence and excitation on the photonic scale. When the charge carrier dynamics in graphene are understood graphene has a high potential as building block for future miniaturized devices in electronics and optoelectronics. To fully explore its potential a full understanding also for the single and collective excitation processes is important.

Consequently, the beginning of the "Carbon Age" [26] as it is predicted and desired

by science, industry and society must be accompanied by research on graphenes unique electronic properties.

Acknowledgment

First of all, I thank my supervisor Prof. Dr. Benson for the possibility to become a member of the "Nanooptics" group. During the last years, it was a pleasure to work and to research in his group. The support and the discussions were always very fruitful and the amount of gained experience is impressive.

I also wish to thank Prof. Dr. Rabe for being the second supervisor. The good cooperation with the group "Physics of Macromolecules" was essential for this thesis. I am also grateful for the support and the possibility to perform experiments in their laboratories.

Special thanks go to Günter Kewes for his effort during the last years. He has constantly provided motivation, new ideas and technical support. He inspired a lot of the investigations performed within this thesis and beyond. Furthermore he spent an impressive amount of time for instruction and improvement.

I am very grateful for the help, the support and the discussions with members of both groups. Especially I would like to thank Nikolai Severin for the constant supply with high quality graphene samples and the time he took for productive discussions.

A lot of ideas were gained during brainstorming in various ways. This comprise further members of the "Macromolecules" group, especially Philipp Lange, Bita Rezzania and Fardin Gholami, members of the "Nanooptics" group like Chris Müller and Alexander Kuhlicke as well as fellow students and office mates, namely Christian Marciniak, Oliver Weisse, Simon Christ, Bruno Schulz and Christoph Roll to whom I am very grateful.

Finally, I am also very grateful to my family, my friends and my girlfriend Elisa for support during this thesis and my life in general.

Bibliography

[1] Wei-Tao Liu, S. W. Wu, P. J. Schuck, M. Salmeron, Y. R. Shen, and F. Wang: Nonlinear broadband photoluminescence of graphene induced by femtosecond laser irradiation, Phys. Rev. B 82, 081408 (2010)

[2] P. Lange, G. Kewes, N. Severin, O. Benson, J. P. Rabe: Evidence for graphene plasmons in the visible spectral range probed by molecules, arXiv:1404.6518 (2014)

[3] K. Kneipp, Y. Wang, H. Kneipp, L. T. Perelman, I. Itzkan, R. R. Dasari, and M. S. Feld: Single Molecule Detection Using Surface-Enhanced Raman Scattering (SERS), Phys. Rev. Lett. 78, 1667 (1997)

[4] R. R. Nair, P. Blake, A. N. Grigorenko, K. S. Novoselov, T. J. Booth, T. Stauber, N. M. R. Peres, A. K. Geim: Fine Structure Constant Defines Visual Transparency of Graphene, Science 320, 1308 (2008)

[5] K. S. Novoselov, V. I. Fal´ko, L. Colombo, P. R. Gellert, M. G. Schwab & K. Kim: A roadmap for graphene, Nature 490, 192-200 (2012)

[6] T. Eberlein, U. Bangert, R. R. Nair, R. Jones, M. Gass, A. L. Bleloch, K. S. Novoselov, A. Geim, and P. R. Briddon: Plasmon spectroscopy of free-standing graphene films, Phys. Rev. B 77, 233406 (2008)

[7] J. Chen, M. Badioli, P.Alonso-González, S. Thongrattanasiri, F. Huth, J. Osmond, M. Spasenović, A. Centeno, A. Pesquera, P. Godignon, A. Z. Elorza, N. Camara, F. Javier García de Abajo, R. Hillenbrand & F. H. L. Koppens: Optical nano-imaging of gate-tunable graphene plasmons, Nature 487, 77–81 (2012)

[8] Z. Fei, A. S. Rodin, G. O. Andreev, W. Bao, A. S. McLeod, M. Wagner, L. M. Zhang, Z. Zhao, M. Thiemens, G. Dominguez, M. M. Fogler, A. H. Castro Neto, C. N. Lau, F. Keilmann & D. N. Basov: Gate-tuning of graphene plasmons revealed by infrared nano-imaging, Nature 487, 82–85 (2012)

[9] Yu Liu, R. F. Willis, K. V. Emtsev, Th. Seyller: Plasmon dispersion and damping in electrically isolated two-dimensional charge sheets, Phys. Rev. B 78, 201403 (2008)

[10] J. W. Weber, V. E. Calado and M. C. M. van de Sanden: Optical constants of graphene measured by spectroscopic ellipsometry, Appl. Phys. Lett. 97, 091904 (2010)

[11] M. Klintenberg, S. Lebegue, C. Ortiz, B. Sanyal, J. Fransson, O. Eriksson: Evolving properties of two-dimensional materials: from graphene to graphite, Journal of Physics: Condensed Matter 21, 33 (2009)

[12] S. A. Maier: Plasmonics: Fundamentals and Applications, Springer (2007)

[13] W. L. Barnes, A. Dereux, T. W. Ebbesen: Surface plasmon sub-wavelength optics, Nature 424, 824-830 (2003)

[14] B. Prade, J. Y. Vinet, A. Mysyrowicz: Guided optical waves in planar heterostructures with negative dielectric constant, Phys. Rev. B 44, 13556 (1991)

[15] H. W. Kroto, J. R. Heath, S. C. O'Brien, R. F. Curl & R. E. Smalley: C60: Buckminsterfullerene, Nature 318, 162-163 (1985)

[16] S. Iijima, T. Ichihashi: Single-shell carbon nanotubes of 1-nm diameter, Nature 363, 603-605 (1993)

[17] K. S. Novoselov, A. K. Geim, S. V. Morozov, D. Jiang, Y. Zhang, S. V. Dubonos, I. V. Grigorieva, A. A. Firsov: Electric Field Effect in Atomically Thin Carbon Films, Science 306, 666-669 (2004)

[18] E. Fradkin: Critical behavior of disordered degenerate semiconductors. II. Spectrum and transport properties in mean-field theory, Phys. Rev. B 33, 3263 (1986)

[19] A. S. Mayorov, R. V. Gorbachev, S. V. Morozov, L. Britnell, R. Jalil, L. A. Ponomarenko, P. Blake, K. S. Novoselov, K. Watanabe, T. Taniguchi, A. K. Geim: Micrometer-Scale Ballistic Transport in Encapsulated Graphene at Room Temperature, Nano. Lett. 11, 2396-2399 (2011)

[20] C. Lee, X. Wei, J. W. Kysar, J. Hone: Measurement of the Elastic Properties and Intrinsic Strength of Monolayer Graphene, Science 321, 385-388 (2008)

[21] A. A. Balandin: Thermal properties of graphene and nanostructured carbon materials, Nature Materials 10, 569-581 (2011)

[22] J. S. Bunch, S. S. Verbridge, J. S. Alden, A. M. van der Zande, J. M. Parpia, H. G. Craighead and P. L. McEuen: Impermeable Atomic Membranes from Graphene Sheets, Nano Lett. 8, 2458-2462 (2008)

[23] A. H. Castro Neto, F. Guinea, N. M. R. Peres, K. S. Novoselov, and A. K. Geim: The electronic properties of graphene, Rev. Mod. Phys. 81, 109-162 (2009)

[24] O. Klein: Die Reflexion von Elektronen an einem Potentialsprung nach der relativistischen Dynamik von Dirac, Zeitschrift für Physik 53, 157-165 (1929)

[25] P. R. Wallace: The Band Theory of Graphite, Phys. Rev. 71, 622 (1947)

[26] E. Malic, A. Knorr: Graphene and Carbon Nanotubes, Wiley-VCH (2013)

[27] A. G. Marinopoulos, Lucia Reining, Angel Rubio, and Valerio Olevano: Ab initio study of the optical absorption and wave-vector-dependent dielectric response of graphite, Physical Review B 69, 245419 (2004)

[28] E. Malic, T. Winzer, E. Bobkin, and A. Knorr: Microscopic theory of absorption and ultrafast many-particle kinetics in graphene, Phys. Rev. B 84, 205406 (2011)

[29] P. Wachsmuth, R. Hambach, M. K. Kinyanjui, M. Guzzo, G. Benner, and U. Kaiser: High-energy collective electronic excitations in free-standing single-layer graphene, Phys. Rev. B 88, 075433 (2013)

[30] F. J. Nelson, J.-C. Idrobo, J. D. Fite, Z. L. Mišković, S. J. Pennycook, S. T. Pantelides, Ji Ung Lee, A. C. Diebold: Electronic Excitations in Graphene in the 1–50 eV Range: The π and $\pi + \sigma$ Peaks Are Not Plasmons, Nano Lett. 14, 3827–3831 (2014)

[31] F. H. L. Koppens, D. E. Chang, F. Javier García de Abajo: Graphene Plasmonics: A Platform for Strong Light–Matter Interactions, Nano Lett. 11(8), 3370–3377 (2011)

[32] Martin Rothe: Fluoreszenzuntersuchung einzelner Quantenemitter auf Graphen, Bachelorarbeit, Humboldt-Universität zu Berlin (2012)

[33] Dong-Hun Chae, T. Utikal, S. Weisenburger, H. Giessen, K. v. Klitzing, M. Lippitz, J. Smet: Excitonic Fano Resonance in Free-Standing Graphene, Nano Lett. 11(3), 1379–1382 (2011)

[34] R. W. Boyd: Nonlinear Optics, 3rd Edition, Elsevier Inc. (2008)

[35] H. J. Simon, D. E. Mitchell, J. G. Watson: Optical Second-Harmonic Generation with Surface Plasmons in Silver Films, Physical Review Letters 33, 1531-1534 (1974)

[36] S. Viarbitskaya, A. Teulle, R. Marty, J. Sharma, C. Girard, A. ud Arbouet, E. Dujardin: Tailoring and imaging the plasmonic local density of states in crystalline nanoprisms, Nature Materials 12, 426–432 (2013)

[37] E. Hendry, P. J. Hale, J. Moger, A. K. Savchenko, and S. A. Mikhailov: Coherent Nonlinear Optical Response of Graphene, Phys. Rev. Lett. 105, 097401 (2010)

[38] J. M. Dawlaty, S. Shivaraman, M. Chandrashekhar, F. Rana, M. G. Spencer: Measurement of ultrafast carrier dynamics in epitaxial graphene, Appl. Phys. Lett. 92, 042116 (2008)

[39] Chun Hung Lui, Kin Fai Mak, Jie Shan, T. F. Heinz: Ultrafast Photoluminescence from Graphene, Phys. Rev. Lett. 105, 127404 (2010)

[40] J. J. Dean, H. M. van Driel: Second harmonic generation from graphene and graphitic films, Appl. Phys. Lett. 95, 261910 (2009)

[41] J. J. Dean, H. M. van Driel: Graphene and few-layer graphite probed by second-harmonic generation: Theory and experiment, Phys. Rev. B 82, 125411 (2010)

[42] A. Savoia, M. Siano, D. Paparo, L. Marrucci: Nonlocal optical second harmonic generation from centrosymmetric birefringent crystals: the case of muscovite mica, J. Opt. Soc. Am. B 28, 679-688 (2011)

[43] B. Rezania, M. Dorn, N. Severin, J.P. Rabe: Influence of graphene exfoliation on the properties of water-containing adlayers visualized by graphenes and scanning force microscopy, Journal of Colloid and Interface Science 407, 500-504 (2013)

[44] Muscovite: Muscovite mineral information and data, retrieved from http://www.mindat.org/min-2815.html, 19th August 2015

[45] M. Dorn, P. Lange, A. Chekushin, N. Severin, and J. P. Rabe: High contrast optical detection of single graphenes on optically transparent substrates, J. Appl. Phys. 108, 106101 (2010)

[46] Encyclopedia Britannica: mica | mineral, retrieved from http://media-1.web.britannica.com/eb-media/66/2666-004-3AD7A666.jpg, 2nd September 2015

[47] E. D. Palik: Handbook of Optical Constants of Solids Academic, Academic Press, New York (1991)

[48] A. C. Ferrari: Raman spectroscopy of graphene and graphite: Disorder, electron–phonon coupling, doping and nonadiabatic effects, Solid State Communications 143, 47–57 (2007)

[49] Lukas Novotny, Bert Hecht: Principles of Nano-Optics, Cambridge University Press (2006)

[50] PerkinElmer Inc.: Avalanche photodiode, A User Guide (2010)

[51] R. R. Nair, P. Blake, A. N. Grigorenko, K. S. Novoselov, T. J. Booth, T. Stauber, N. M. R. Peres, A. K. Geim: Fine Structure Constant Defines Visual Transparency of Graphene, Science 320, 5881 (2008)

[52] F. Javier García de Abajo: Graphene Plasmonics: Challenge and Opportunities, ACS Photonics 1, 135-152 (2014)

[53] M. L. Brongersma, N. J. Halas and P. Nordlander: Plasmon-induced hot carrier science and technology, Nature Nanotechnology 10, 25–34 (2015)

[54] R. Jago, T. Winzer, A. Knorr, and E. Malic: Graphene as gain medium for broadband lasers, Phys. Rev. B 92, 085407 (2015)

Publication Comprising Parts of this Work

M. Rothe, G. Kewes, N. Severin, J. P. Rabe, O. Benson: Luminescence of graphene in the visible spectral range after short-pulse excitation in the near infrared, DPG Frühjahrstagung, Berlin, 15.-20.3.2015

Honesty Declaration

I hereby declare that the work submitted is my own and that all passages and ideas that are not mine have been fully and properly acknowledged.

Berlin, September 22, 2015

_____